Order Number 9017186

A simulation study of magnetic reconnection processes at the dayside magnetopause

Shi, Yong, Ph.D.

University of Alaska Fairbanks, 1989

U·M·I

300 N. Zeeb Rd.
Ann Arbor, MI 48106

A SIMULATION STUDY OF MAGNETIC RECONNECTION
PROCESSES AT THE DAYSIDE MAGNETOPAUSE

by
Yong Shi

RECOMMENDED:

D. W. Swift

J. Gosink

R. Gatterdam

S-I. Akasofu

L. C. Lee, Chairman, Advisory Committee

J. L. Morack, Head, Physics Department

APPROVED:

K. Jayaweera, Dean, College of Natural Sciences

L. Proenza, Dean of the Graduate School

10/10/89
Date

A SIMULATION STUDY OF MAGNETIC RECONNECTION PROCESSES AT THE DAYSIDE MAGNETOPAUSE

A
THESIS

Presented to the Faculty of the University of Alaska
in Partial Fulfillment of the Requirements
for the Degree of

DOCTOR OF PHILOSOPHY

By
Yong Shi, B. S.

Fairbanks, Alaska
December, 1989

Abstract

In this thesis, the dayside reconnection processes are studied by using computer simulations.

First, the global magnetic reconnection patterns at the dayside magnetopause are studied based on a two-dimensional incompressible magnetohydrodynamic (MHD) code. It is found that multiple X line reconnection may prevail at the dayside magnetopause when the magnetic Reynolds number is large (> 200). The formation and subsequent poleward convection of magnetic islands are observed in the simulation. The Alfvén Mach number of the solar wind, M_{Asw}, can also change the reconnection patterns. For a large M_{Asw}, reconnection tends to occur at the higher latitude region.

Secondly, the structure of the dayside reconnection layer is studied by a two-dimensional compressible MHD simulation. In a highly asymmetric configuration typical of the dayside magnetopause, the pair of slow shocks bounding the reconnection layer in Petschek's symmetric model is found to be replaced by an intermediate shock on the magnetosheath side and a weak slow shock on the magnetospheric side.

In addition, a mechanism for the enhancement of B_y, which is observed in the magnetopause current layer and magnetic flux tubes, is proposed.

Table of Contents

List of Figures

List of Tables

Acknowledgements

I am greatly indebted to the many people who have contributed to the completion of this thesis. It would be impossible to name all those who have helped directly or indirectly in its preparation, but I must acknowledge several people in particular.

I owe a special debt to Dr. L. C. Lee, my adviser, for introducing me into this field of space physics and guiding me through four memorable years of graduate study at Geophysical Institute, University of Alaska Fairbanks. His constant support and inspiration encouraged the completion of this thesis.

In 1986, Dr. L. C. Lee suggested that I worked on the numerical simulation of the dayside reconnection as the subject of my thesis. He arranged for my visit to UCLA to work under the guidance of Dr. C. C. Wu, an expert in MHD simulation, to whom I must extend my sincere thanks. It was during my stay in UCLA that I sharpened my skill in computer simulation and had, for the first time, a hands-on experience on the supercomputer Cray X-MP, which proved to be a powerful tool in the following years of my research. Dr. Z. F. Fu and Dr. D. Swift are two other persons who have taught me the numerical simulation. To them go my thanks too.

In the preparation of this thesis, my committee members (Drs. L. C. Lee, D. Swift, S-I. Akasofu, J. Gosink, and R. Gatterdam) patiently reviewed each draft and gave valuable suggestions for improving the thesis. Their support meant a lot. I wish to express my thanks to them for their support.

Many of my fellow students at Geophysical Institute also provided generous help. My thanks go to all, with special mention of A. L. La Belle-Hamer. The staff of the publication office of Geophysical Institute carefully read my thesis and provided suggestions for improving my English. I am grateful to their help.

I gratefully acknowledge the financial support from the National Science Foundation grant and Department of Energy grant to the University of Alaska. The computing support from the San Diego Supercomputing Center and the computing center of Geophysical Institute was particularly appreciated.

I wish to extend my thanks to Dr. S. Wang, my adviser for one year at University of Science and Technology of China, P. R. China. I would never have become involved in space physics had it not for him.

Finally, I am indebted to my wife, Ya-tao, for those many nights she stayed up with me to help assemble the thesis.

Chapter 1. Introduction

A fundamental feature of magnetized plasmas is the exchange of energy forms between the energy of magnetic fields and the energy of particles. Historically, the concept that we now call magnetic reconnection originated from an attempt by *Ronald G. Giovanelli* [1946, 1948] to explain solar flares in terms of such energy exchange. *Giovanelli* [1946] proposed that the optical emission associated with solar flare is from atoms that are excited by electrons accelerated in induced electric fields near neutral points (the point where the magnetic field is zero) during the evolution of magnetic fields near sunspots. *Hoyle* [1949] and *Dungey* [1961] applied the concept of magnetic reconnection to the earth's magnetosphere. On the other hand, Giovanelli's original idea was further developed and elaborated by a number of authors [*Sweet*, 1958; *Parker*, 1957; *Petschek*, 1964; *Sonnerup*, 1970; *Yeh and Axford*, 1970]. Their work provides the basis of the present theories of magnetic reconnection.

The earlier models of magnetic reconnection were all based on a magnetohydrodynamic (MHD) description of magnetized plasma. In order to understand the phenomenon of magnetic reconnection, it is useful to start with the magnetic induction equation in MHD theory. In a simple electrically conducting fluid, Ohm's law has the form

$$\mathbf{j} = \sigma(\mathbf{E} + \mathbf{v} \times \mathbf{B}), \tag{1.1}$$

where $\mathbf{j}$ is the electrical current density, σ is the electrical conductivity, $\mathbf{v}$ is the fluid velocity, $\mathbf{E}$ is the electric field, and $\mathbf{B}$ is the magnetic field. Using Faraday's and

Ampere's laws:

$$\frac{\partial \mathbf{B}}{\partial t} = -\nabla \times \mathbf{E}, \tag{1.2}$$

$$\mu_0 \mathbf{j} = \nabla \times \mathbf{B}, \tag{1.3}$$

where μ_0 is the magnetic permeability in free space, the curl of (1.1) can be written as

$$\frac{\partial \mathbf{B}}{\partial t} = \nabla \times (\mathbf{v} \times \mathbf{B}) + \eta \nabla^2 \mathbf{B}, \tag{1.4}$$

where $\eta = 1/\mu_0 \sigma$ is the magnetic diffusivity. Equation (1.4) is the magnetic induction equation in MHD theory. Equation (1.4) indicates that changes in the magnetic induction vector $\mathbf{B}$ are caused by the convection of the magnetic field with the plasma fluid (first term on the right-hand side of (1.4)) and the diffusion of the magnetic field (second term on the right-hand side of (1.4)). If $\eta = 0$ in (1.4), the "frozen-in" theorem of MHD theory states that the flux of the magnetic field through a loop moving with the fluid is conserved or the magnetic field lines are frozen to the fluid and move with the fluid. In such a case, reconnections between different magnetic field lines cannot happen as the occurrence of reconnection would break the frozen-in condition. Usually, if the characteristic speed V and length scale L of the configuration of the fluid and magnetic field are such that the magnetic Reynolds number VL/η is much greater than one, the magnetic field lines will diffuse slowly relative to the fluid and hence the frozen-in condition is approximately satisfied. In most regions of space plasma, the magnetic Reynolds number is very large and therefore the "frozen-in" theorem generally holds. However, local regions exist in the space plasma where the magnetic field has a large gradient. In these regions, the diffusion of the magnetic field will become significant (or the second term on the right-hand side of (1.4) becomes larger or comparable to the first term) and the frozen-in condition breaks down to allow magnetic reconnection to occur.

One particular configuration in which magnetic reconnection may occur is the current sheet (the interface of two magnetized plasma regions with an antiparallel component of magnetic field). In the earth's magnetosphere, current sheets exist at the dayside magnetopause, which is formed as the solar wind presses the interplanetary magnetic field against the geomagnetic field, and in the magnetotail, resulting from the tangential stresses exerted by the solar wind on the magnetic field in the two tail lobes. Current sheets may also be found in the solar atmosphere, for example, between approaching magnetic dipoles in the photosphere [*Priest and Raduu*, 1975] and as a result of the stretching of magnetic loops on the sun during rapid plasma ejection [*Carmichael*, 1964]. Figure 1.1 illustrates the magnetic reconnection process in a current sheet. The solid lines are magnetic field lines and the hollow large arrows represent the plasma flow. Figure 1.1*a* shows a current sheet configuration before magnetic reconnection at time $t = 0$, where the four magnetic field lines nearest to the current sheet are labelled as field lines aa', bb', cc', and dd', respectively, for purpose of illustration. Figure 1.1*b* shows the magnetic field configuration and plasma flow having resulting from the reconnection. Field lines aa' and cc' are cut in the diffusion region around reconnection point and reconnected to form two new field lines ac and $a'c'$. In the reconnection configuration, there are basically four regions which consist of topologically different magnetic fields. Region 1 and Region 2 (up and down in Figure 1.1*b*) consist of unreconnected field lines and are referred to as the upstream regions or inflow regions. Region 3 and Region 4 (left and right in Figure 1.1*b*) consist of reconnected field lines and are referred to as the downstream regions or the outflow regions. The upstream regions and downstream regions are separated by the so-called separatrix (lines db' and bd' in Figure 1.1*b*). Usually, the magnetic field strength downstream of the separatrix is weaker than in the upstream region, while the plasma flow speed is higher in the downstream region than in the upstream region. Hence, in the process of magnetic

reconnection, part of the energy stored in the upstream magnetic field is converted to the downstream plasma kinetic energy. Therefore, the significance of the reconnection process is twofold: (1) to convert magnetic energy to plasma kinetic energy and (2) to provide coupling between the magnetic fields and plasmas on the two sides of the current sheet.

Most reconnection models in the past are limited to a two-dimensional configuration and a steady state. The earliest one proposed by *Sweet* [1958] and developed further by *Parker* [1957, 1963] neglected entirely the weak magnetic field on the downstream side of the separatrix. Thus, in the Sweet-Parker model, the outflow of plasma is essentially field-free and is accelerated by the pressure gradient in the outflow region. The process can be better described as magnetic field annihilation rather than reconnection, since the Sweet-Parker model describes basically a magnetic diffusion process (this is why the Sweet-Parker model is sometimes referred to as a diffusion model). In a steady state (a balance between diffusion and convection), the magnetic reconnection rate defined as the upstream Alfvén Mach number, $M_{A1} = v_1/V_{A1}$, where v_1 is the upstream inflow speed and V_{A1} is the upstream Alfvén speed, can be shown to be

$$M_{A1} = R_m^{-1/2}, \tag{1.5}$$

The magnetic Reynolds number R_m in (1.5) is defined as

$$R_m = \frac{V_{A1} L}{\eta}, \tag{1.6}$$

where L is the scale length of the reconnection configuration. Note that, since in most astronomical applications the magnetic Reynolds number is very large, the above relation leads to a very slow rate at which field lines approach each other and are annihilated. The Sweet-Parker model was originally suggested to explain solar flares. However, in the Sweet-Parker model, the rate at which the magnetically stored energy

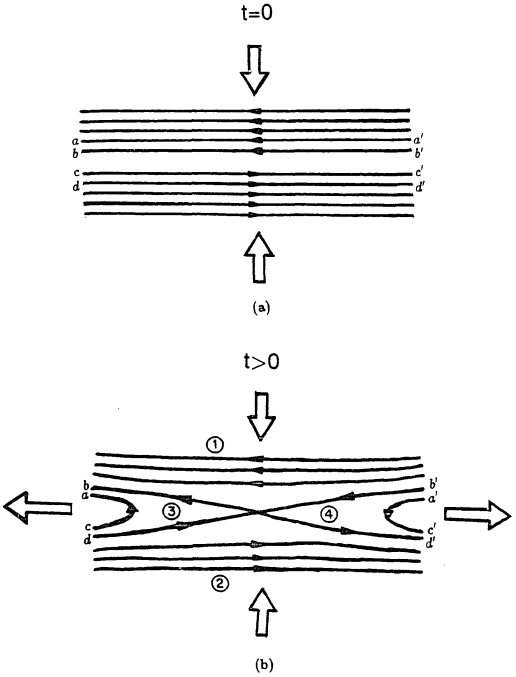

Figure 1.1 Illustration of magnetic reconnection process in a current sheet.

can be converted into plasma kinetic energy is too slow to account for the rapid energy release in a solar flare. Based on the Sweet-Parker model, the estimated time for the release of the same amount of energy observed in a solar flare is a factor of 100 to 1000 too large for the observed solar flare time scale.

To achieve a higher reconnection rate, *Petschek* [1964] suggested a new magnetic reconnection model. Note that the configuration of magnetic reconnection contains a magnetic field reversal region (the downstream region as shown in Figure 1.1). In the field reversal region, the magnitude of the magnetic field decreases and the plasma kinetic or thermal energy increases. Hence, as mentioned before, the energy of the magnetic field is converted into plasma thermal or flow energy. In the Sweet-Parker model, the reduction of magnetic field in the field reversal region is purely due to the diffusion of the magnetic field into plasma in the presence of finite resistivity. The conversion of energy in the Sweet-Parker model is hence a result of Ohmic heating. However, *Petschek* [1964] realized that the MHD slow shocks can also convert the magnetic energy to the plasma energy.

Shown in Figure 1.2 is a schematic sketch of Petschek's reconnection model. The magnetic field lines in Figure 1.2 are represented by light lines. In Petschek's model, the Sweet-Park type diffusion region (the shaded area) is very small, and the energy conversion process takes place mainly along two pairs of slow shocks (heavy lines in Figure 1.2). In Figure 1.2, the inflow regions are to the left and right and the outflow regions (boundary layer in Petschek's original terminology) are above and below the diffusion region. The standing slow shocks contain concentrated electric currents. Hence, the slows shocks serve, first, to reduce the magnetic field in the downstream region and, second, to accelerate plasma across the shocks in approximately the tangential direction of the shock by the $\mathbf{j} \times \mathbf{B}$ force associated with them. In the figure, the plasma flowing toward the outflow region from the upstream regions (left and right sides in the figure)

is turned and accelerated by the slow shocks to flow out in the positive and negative y directions, respectively. In Petschek's model, since the conversion of magnetic energy into plasma kinetic and thermal energy is mainly through the acceleration and heating of plasma by these slow shocks, the reconnection rate has a weak dependence on the resistivity or magnetic Reynolds number. The contribution from Sweet-Parker Ohmic heating in the diffusion region is negligible in the energy conversion process of Petschek's model. Based on his model, *Petschek* [1964] demonstrated that the energy required for a flare can be released in 10^2 sec. The time is short enough to account for the observed solar flare times.

Sonnerup [1970] and *Yeh and Axford* [1970] adopted Petschek's idea to develop a different reconnection model. *Vasyliunas* [1975] pointed out that the major difference between the Petschek model and the Sonnerup-Yeh-Axford model is in the inflow region: The flow pattern corresponds to a fast mode expansion in Petschek's model and a slow mode expansion in Sonnerup-Yeh-Axford's model. Based on analytical solutions, *Priest and Forbes* [1986] obtained a family of steady-state reconnection types including the Sweet-Parker model, Petschek model, and Sonnerup-Yeh-Axford model. They found that the boundary conditions are important for the appearance of different types of reconnection. *Lee and Fu* [1986*a*] demonstrated in their local numerical simulations that the plasma inflow speed, the scale size of the simulation box, and the magnetic Reynolds number are the three most important parameters controlling the reconnection types. They found that different combination of these three parameters can give rise to reconnections fitting the Sweet-Parker model, the Petschek model, or the Sonnerup-Yeh-Axford model. Note that all these three types of reconnection are steady-state models and are characterized by magnetic reconnection along a single line (the X line). Furthermore, *Lee and Fu* [1986*a*] made the important suggestion that another basic type of magnetic reconnection exists: The time-dependent multiple X line reconnection

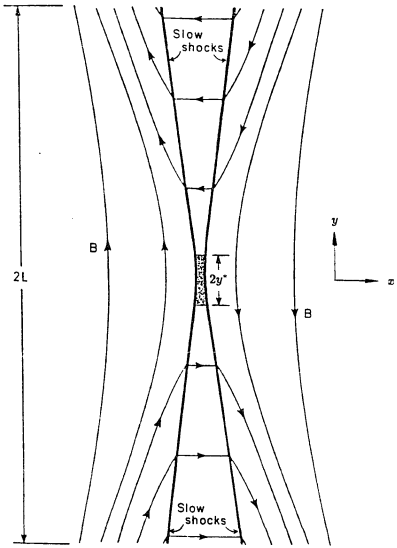

Figure 1.2 Configuration of slow MHD shocks and magnetic field lines in Petschek's magnetic reconnection model (*Petschek*, 1964).

characterized by the formation and convection of magnetic islands. *Lee and Fu*'s [1986*a*] simulation shows that when the magnetic Reynolds number is large, or the inflow speed of the plasma is large, or the initial current sheet is long, multiple X-line reconnection tends to occur.

Along with the development of the fundamental theories of magnetic reconnection, the understanding of magnetic reconnection in the earth's magnetosphere has also seen progress. The concept of magnetic reconnection was introduced to the Earth's magnetosphere in 1961 by *Dungey* [1961]. Figure 1.3 shows the configuration of magnetic reconnection in *Dungey*'s [1961] open magnetosphere model. The solid lines in Figure 1.3 are magnetic field lines (geomagnetic field lines and interplanetary field lines). In Dungey's model, magnetic reconnection can occur at the dayside magnetopause as well as in the magnetotail. In particular, at the dayside magnetopause, Dungey's model predicts that the reconnection will occur at the subsolar point (the subsolar point can be roughly defined as the point on the dayside magnetopause which is closest to the sun) along a single X line (reconnection line perpendicular to the two-dimensional plane of the figure). The reconnected geomagnetic field lines become open field lines and,after the reconnection, the magnetopause is no longer a closed one, i.e., not a tangential discontinuity separating the geomagnetic field from the solar-wind plasma and interplanetary field (IMF). The dayside reconnection in Dungey's model is characterized by its large scale and quasi-steady state. Note that Dungey's model is only a qualitative one. Since Dungey's first open magnetosphere model, dayside reconnection has been considered as playing an important role in the transfer of energy, momentum, and particles between the solar wind and the earth's magnetosphere.

A more sophisticated dayside reconnection model was proposed by *Levy et al.* [1964]. They suggested that in the process of dayside reconnection, the dayside magnetopause remains a well-defined current layer. However, this current layer now corre-

sponds to a rotational discontinuity (RD) with a nonvanishing normal magnetic field component B_n instead of a tangential discontinuity (TD). The dayside reconnection site in *Levy et al.*'s [1964] model is also assumed to be at the subsolar point as in Dungey's model. The plasma passing through this current layer (RD) is accelerated away from the subsolar point by the Lorentz or $\mathbf{I} \times \mathbf{B}_n$ force, where $\mathbf{I}$ is the magnetopause current. The accelerated plasma forms a boundary layer of jetting plasma immediately inside the magnetopause. Tailward of the cusp regions, the magnetopause current $\mathbf{I}$ is reversed and plasma is then decelerated. In this way, the mechanical energy is extracted from the solar wind and stored as magnetic energy in the geomagnetotail [e.g., *Swift*, 1980].

The two basic properties of *Levy et al.*'s [1964] model are the existence of the normal magnetic field B_n and a high-speed plasma jet near the dayside magnetopause. A magnetic field component B_n normal to the magnetopause has been observed [*Sonnerup*, 1976] when the magnetosheath field opposes geomagnetic field, although not as a permanent feature. However, the predicted high speed plasma jet [*Levy et al.*, 1964] was absent in most of the satellite observations such as HEOS 2 [e.g., *Haerendel*, 1977; *Haerendel et al.*, 1978] even when the satellites have had the right position and latitude to observe them. On the other hand, *Paschmann et al.* [1979] and *Sonnerup et al.* [1981] have identified a few exceptional crossings in the subsolar region which show enhanced flow speeds in the magnetospheric boundary layer. These cases represent the most promising examples to date for the relatively direct observation of the expected signatures of steady-state reconnection. However, the fact that the high-speed plasma jets are rare suggests that magnetopause reconnection may be more sporadic and localized than originally expected. This is also supported by the observation of a plasma boundary layer inside the dayside magnetopause [*Eastman et al.*, 1976; *Crooker*, 1977]. The possibility of magnetic reconnection near the cusp and elsewhere on the magnetopause

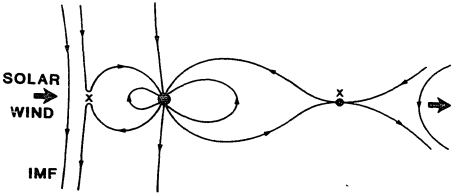

Figure 1.3 Configuration of magnetic field lines in Dungey's single X line open magnetosphere.

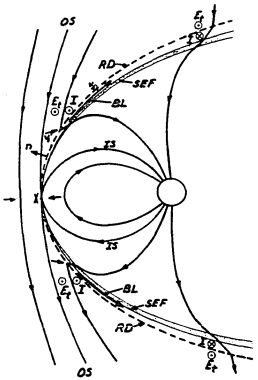

Figure 1.4 Magnetopause reconnection proposed by Levy et al. [1964]. The principal geometrical features of this model are: the separator (X); the magnetopause current layer in the form of a rotational discontinuity (RD); a thin high-velocity plasma boundary layer (BL) immediately inside the magnetopause and, at its innermost edge, a slow mode expansion fan (SEF, shown shaded). The inner and outer separatrix surfaces are marked by (IS) and (OS), the reconnection electric field by E_t, and the magnetopause current by I.

surface have also been suggested [*Haerendel*, 1977]. In a laboratory experiment, *Podgorny et al.* [1978] claimed to have observed Dungey-type subsolar point reconnection for a small solar-wind Alfvén Mach number and high- latitude cusp region reconnection for a large solar-wind Alfvén Mach number (~ 10). *Heikkila* [1975] even argued that dayside reconnection may not exist at all, because of the failure to observe a steady-high speed plasma jet".

The discovery of flux transfer events (FTEs) [*Russell and Elphic*, 1978] by ISEE satellites at the dayside magnetopause stimulated some researchers to propose new dayside reconnection models. FTEs are characterized by bipolar pulses of magnetic components normal to the dayside magnetopause surface. The duration of each event is typically 1–2 minutes and the interval between successive events is usually 2-10 minutes. When the interplanetary magnetic field (IMF) has a southward component, FTEs are almost always observed. This correlation between the occurrence of FTEs and IMF orientation provides strong evidence that FTEs are closely associated with dayside reconnection. Therefore, nearly all the FTE models invoke magnetic reconnection. On the other hand, FTEs can also be used to test different dayside reconnection models.

Based on the properties of the observed FTEs, *Russell and Elphic* [1978] proposed a patchy reconnection model for the dayside magnetopause. They suggested that since the magnetosphere is undergoing patchy reconnection, we are seeing FTEs. As a result of the patchy reconnection, a pair of elbow-shaped magnetic flux tubes connecting the IMF and the geomagnetic field are formed. The flux tube, along with ambient plasma, is then convected poleward. The cross-section of the flux tubes is about 1 R_E^2, R_E being the earth radius. The patchy reconnection process is depicted schematically in Figure 1.5. *Sonnerup* [1987] pointed out the possibility of magnetic flux being wrapped

around the flux tube as it moves so as to generate core current. *Kan* [1988] suggested that the 3-D tearing may be the cause of the intermittent and patchy reconnections.

Another dayside reconnection model was proposed by *Lee and Fu* [1985]. In Lee-Fu model, dayside reconnections occur presumably along several reconnection lines (X lines). For this reason, they have named their model the multiple X line reconnection. Figure 1.6 shows the dayside magnetic reconnection configuration envisioned in the Lee-Fu model. Figure 1.6*a* is the 3-D perspective view and Figure 1.6*b* is the corresponding 2-D projection. Three X lines are plotted in Figure 1.6 for purpose of illustration. The multiple X line reconnection results in the formation of magnetic islands at the dayside magnetopause (Figure 1.6*b*). In the presence of a finite IMF B_y component, these magnetic islands correspond to magnetic flux tubes (Figure 1.6*a*). The magnetic islands formed or magnetic flux tubes are later convected poleward away from the subsolar magnetopause region and new ones will then be formed. The cross section of the magnetic flux tubes is on the order of 1 R_E^2. The formation and convection of the magnetic flux tubes will then generate the observed signatures of FTEs [*Fu and Lee*, 1985; *Lee*, 1986, *Ding et al.*, 1986; *Shi et al.*, 1989]. The type of dayside reconnection described in the Lee-Fu model is an impulsive and not a small- scale process characterized by repeated formation and convection of magnetic islands as long as the magnetosheath field has a southward component. The primary cause of the multiple-X line reconnection was thought to be the onset of a tearing mode instability in the magnetopause current layer [*Lee and Fu*, 1986*a*].

More recently, a bursty single X-line reconnection model was put forth by *Southwood et al.* [1988] and *Scholer* [1988*a*] as shown in Figure 1.7 (Figure 1.7 shows only the 2-D view). They argued that a sudden increase in the reconnection rate on the magnetopause gives rise to bulge-shaped regions of plasma containing a bended magnetic

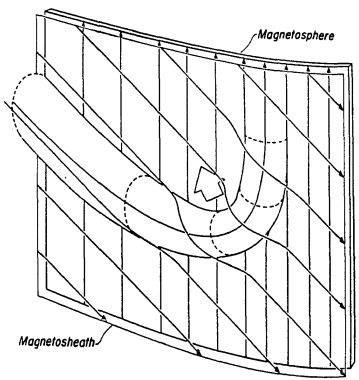

Figure 1.5 Russell and Elphic's patchy reconnection model. Magnetosheath field lines, slanted arrows, have connected with magnetospheric field lines, vertical arrows, possibly off the lower edge of the figure. The connected flux tube moves in the direction of the large arrow (*Russell and Elphic*, 1978).

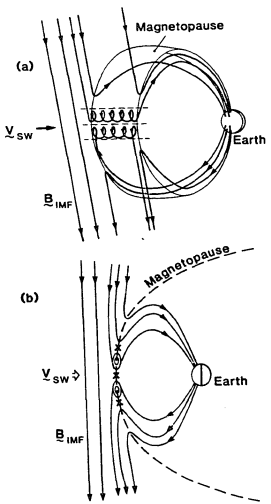

Figure 1.6 Lee-Fu's dayside multiple X-line reconnection process (a) a perspective view of the open magnetic flux tubes and the regular open field lines as a result of multiple X-line reconnection at the dayside magnetopause, and (b) the projection of flux tubes in the noon-midnight meridian plane (*Lee and Fu*, 1985).

field. In the bulge-shaped region, plasma is accelerated to high speed. When reconnection has ceased, the bulge-shaped region threaded by the magnetic field and created by the earlier reconnection continues to move away from the reconnection site. This model, though also characterized by reconnection along a single X line as in Dungey's early model, describes a time-dependent process in which reconnection is assumed to be suddenly switched on and off. This reconnection model can also explain some of the observed features of FTEs.

In the above-mentioned efforts, many aspects of the dayside reconnection remain unclear. The objective of this thesis is to gain a better understanding of the dayside reconnection and related phenomena through numerical simulations.

In Chapter 2, the global pattern of the dayside reconnection as studied by a two-dimensional global simulation using magnetohydrodynamic (MHD) code is discussed. The dependences of the reconnection pattern on the magnetic Reynolds number, the solar-wind Alfvén Mach number, and the current-dependent resistivity, were investigated. The simulation results will be compared with observations and some theoretical dayside reconnection models. The magnetic and plasma signatures generated in one particular case (Lee-Fu type reconnection) will be used to interpret FTEs. In particular, Lee-Fu type multiple X-line reconnections will be discussed in detail in relation to the simulation results.

The internal structure of the dayside reconnection layer is the subject of Chapter 3, which presents reconnection layer structure under different symmetry conditions as simulated by two-dimensional compressible MHD simulations. First, reconnection in a symmetric configuration was simulated to confirm the classical Petschek model. Second, several cases with asymmetric configurations typical of the dayside magnetopause were simulated to determine the reconnection layer structure at the dayside magneto-

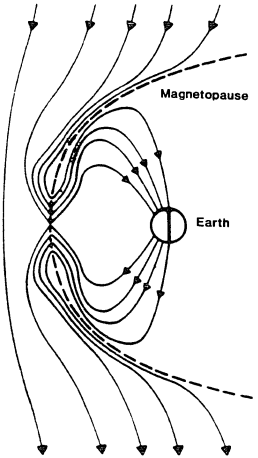

Figure 1.7 Magnetic field configuration in dayside single X-line bursty reconnection (*Scholer*, 1988*a*).

pause. The effect of asymmetry in magnetic field and plasma on the reconnection layer structure was examined. In addition, the effect of plasma β on the strength of the MHD shocks associated with the reconnection layer was studied, where β is the ratio of plasma to magnetic pressures.

Chapter 4 proposes a mechanism to explain the observed core magnetic field enhancement associated with magnetic flux tubes in flux transfer events. Again, a two-dimensional compressible MHD simulation was carried out to support the proposed mechanism. The results were also applied to the magnetotail to explain similar observations.

Chapter 5 contains the summary of the thesis.

Chapter 2. Global MHD Simulations of Magnetic Reconnections at the Dayside Magnetopause

2.1 Introduction

As mentioned in Chapter 1, with the discovery of FTEs, the emphasis of theoretical dayside reconnection models has shifted from large-scale steady-state ones to small-scale sporadic or impulsive ones. The same trend is seen in computer simulations. In a series of computer simulations [*Fu and Lee*, 1985; *Lee and Fu*, 1986*a*] of driven reconnection based on a slab model, impulsive reconnection processes resulted from multiple X-line reconnection and the transition criteria from steady-state to impulsive reconnections were investigated. *Scholer* [1988*a*] simulated the bursty reconnection processes based on single X-line reconnection. Formations of magnetic islands in other local simulations are also sometimes observed. [*Birn and Hones*, 1981; *Biskamp*, 1982; *Leboeuf et al.*, 1982; *Forbes and Priest*, 1983; *Matthaeus and Lamkin*, 1985; and *Scholer and Roth*, 1987].

Spacecraft have a limited capability of obtaining a global-scale picture of the dayside reconnection. Global MHD simulations have become, therefore, increasingly important. Global MHD simulations of solar wind-magnetosphere interaction have been done by a number of workers [e.g., *Lyon et al.*, 1981; *Wu et al.*, 1981; *Ogino et al.*, 1986]. However, the low resolution at the dayside magnetopause in these simulations has made it difficult to study processes of a characteristic scale $\sim 1\ R_E$, such as FTEs

or other small-scale reconnection processes. In a recent semi-global MHD simulation, *Sato* [1986] reported one simulation case in which field-twisted flux tubes were observed at the dayside magnetopause. In *Ogino et al.*'s [1989] global simulation, twisted magnetic flux tubes are also observed at the dayside magnetopause. The observed flux tubes in these global simulations may represent only one particular class of the dayside reconnection because of the limited number of simulation cases. In view of this, a systematic and high-resolution global MHD simulation is needed to solve the mystery of the dayside reconnection.

This chapter presents a global two-dimensional incompressible MHD simulation which aims: (1) to demonstrate various possible dayside reconnection patterns, e.g., steady-state single X-line reconnection, multiple X-line reconnection, and single X-line bursty reconnection; (2) to establish quantitative correlations between reconnection patterns and the physical parameters such as the local dayside magnetopause resistivity and the solar wind Alfvén Mach number; (3) to study the plasma flow patterns at the dayside magnetopause associated with the dayside reconnections; and (4) to interpret some of the observed features of flux transfer events (FTEs) in terms of the simulation results.

The chapter is organized in the following way. Section 2 presents the simulation model and numerical procedures. Different dayside reconnection patterns observed in the present simulations are shown and discussed in section 3. Section 4 compares the observed flux transfer event with two particular types of dayside reconnections reproduced in the simulation: Lee-Fu's multiple X-line reconnection model and the bursty single X-line reconnection model. In section 5, Lee-Fu's multiple X-line reconnection model is further discussed. Section 6 concludes this chapter by summarizing the major results of the work presented here and discussing the limitations and applicability of the simulation results.

2.2 Simulation Model and Numerical Scheme

2.2.1 Simulation model and governing equations

The global simulation presented in this chapter is two-dimensional in the x-z plane of the Geocentric Solar Magnetosphere (GSM) coordinate system. Figure 2.1 illustrates the simulation model. A two-dimensional magnetic dipole is used to represent the geomagnetic dipole field. Initially, the dipole field is confined by the solar wind coming from the sun and entering continuously from the left boundary of the simulation box. The rectangular box is the simulation domain. At the start of the simulation, a southward interplanetary magnetic field (IMF) is introduced from the left boundary and is carried by solar wind towards the geomagnetic dipole. After reaching the dayside magnetopause, the IMF will reconnect with the geomagnetic field. The simulation uses a magnetohydrodynamic (MHD) approach. The plasma fluid is further assumed to be incompressible for simplicity. It needs to be pointed out that the present study is attempted as a first step towards the ultimate solution of the solar wind-magnetosphere interaction problem. A discussion of the applicability and validity of the present study can be found in section 2.6.

Under the incompressibility assumption, the MHD equations governing the behavior of magnetic fields and plasmas can be reduced to a compact form [e.g., *Lee and Fu*, 1986*a*]:

$$\frac{\partial A}{\partial t} = -\mathbf{v}\cdot\nabla A + \eta\nabla^2 A \tag{2.1}$$

$$\frac{\partial \Omega}{\partial t} = -\mathbf{v}\cdot\nabla\Omega + \mathbf{B}\cdot\nabla J \tag{2.2}$$

where A is the y component of the magnetic vector potential defined as $\mathbf{B} = \nabla\times(A\hat{y}) + B_y\hat{y}$, Ω is the vorticity related to the plasma velocity by $\Omega\hat{y} = \nabla\times\mathbf{v} = \nabla^2\phi\hat{y}$, ϕ is

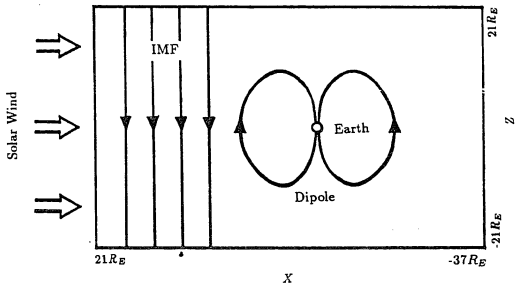

Figure 2.1. A schematic sketch of the simulation model. The rectangular box is the simulation domain, where R_E is the earth radius. The x-axis is pointing to the sun and z-axis is in the northward direction. The southward interplanetary magnetic field (IMF) is carried by solar wind entering from the left boundary of the simulation box towards the geomagnetic dipole and reconnects with the geomagnetic dipole field upon its arrival at the dayside magnetopause.

the stream function, $J = -\nabla^2 A$ is the current density and η is the resistivity. For simplicity, we let $B_y = 0$ in this simulation.

In (2.1), (2.2), and the simulation results presented hereinafter, the normalization units for each physical quantity are displayed in Table 2.1.

TABLE 2.1 Normalization Units of the Simulation

physical quantity	normalization unit
magnetic field	B_0
velocity	$V_{A0} = B_0/\sqrt{\mu_0 \rho}$
length	R_E
current density	$J_0 = B_0/\mu_0 R_E$
resistivity	$\eta_0 = \mu_0 R_E V_{A0}$
time	$t_A = R_E/V_{A0}$
electric field	$E_0 = V_{A0} B_0$

In Table 2.1, B_0 is the initial magnetic field strength at the subsolar point, R_E is the earth radius, ρ is the plasma density assumed to be a constant everywhere, μ_0 is the magnetic permeability in free space. V_{A0} is the corresponding Alfvén speed at the subsolar point and t_A is usually referred to as Alfvén transit time (based on R_E and V_{A0}). Based on observations, values of some normalization units are given as follows: $B_0 \sim 30$ nT, $V_{A0} \sim 200$ km/s, and $t_A \sim 30$ sec.

2.2.2 Simulation domain and boundary conditions

The global simulation distinguishes itself from the local simulation in that the nonphysical effects of numerical boundaries are minimized, provided that the global simulation domain is large enough compared to the spatial extent of regions under study. In the

present study, the simulation domain was chosen as a rectangular box in the x-z plane (see Figure 2.1) extending from -21 to 21 R_E in the z direction (north direction) and from -37 R_E to 21 R_E in the x direction (sunward direction). The later simulation results show that the size of the chosen simulation domain is appropriate for the dayside reconnection. Since only cases with purely southward solar wind interplanetary magnetic fields were studied, the simulation was conducted only in the upper half plane ($z > 0$) because of the symmetry (or anti-symmetry) of the model with respect to the x-axis.

While a larger simulation domain is desirable, it is equally important to maintain a reasonable spatial resolution or to construct the grid mesh as fine as possible. An efficient mean to meet both requirements is by the use of nonuniform grid mesh. In this simulation, we wished to study such small scale events as flux transfer events (FTEs) with characteristic scale of about 1 R_E. For this reason, a nonuniform grid mesh was used which provided a resolution of 0.075 R_E near the dayside magnetopause in a region from $5R_E$ to $12R_E$ in the x direction and from 0 to $12R_E$ in the z direction. For the whole upper half simulation domain, 200 $\times$ 200 grid points were employed. Figure 2.2 shows the grid mesh used in the simulation. Note since the magnetotail is not to be studied in this simulation, the grid size in the x direction (Δx) increases in the tailward direction in the region $x < 5R_E$. It will be seen later in the simulation results that the poor resolution in the $x < 0$ region results in spurious magnetic field patterns. However, these pseudo patterns do not affect the reconnection process at the dayside magnetopause.

The simulation boundaries were specified as follows.

(1) Left boundary ($x = 21$ R_E): the solar wind inflow speed is maintained at v_{sw}, or equivalently, the stream function $\phi(x = 21R_E, z) = -v_{sw}z$. A southward IMF is introduced at time $t \geq 0$ by imposing on the left boundary a magnetic vector potential

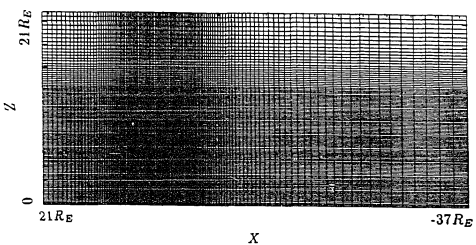

Figure 2.2 The nonuniform grid mesh used in the simulation for the upper half ($z > 0$) of the simulation domain. 200×200 grid points are employed. The smallest grid sizes Δx and Δz are 0.075R_E and are used in the region from 5R_E to 12R_E in the x direction and 0 to 12R_E in the z direction.

$A(x = 21R_E, z, t) = -v_{sw}B_{sw}t$, where B_{sw} is the IMF magnitude. Note that this boundary condition on A ensures that the leading field line (the first field line) of IMF has $A = 0$. Reconnection between IMF and geomagnetic field lines can occur, since the outermost geomagnetic field line has initially $A = 0$ (at $r = 10R_E$ or see (2.3') in subsection 2.2.3). Vorticity Ω at $x = 21R_E$ is kept at its initial value, which is zero.

(2) At the central boundary ($z = 0$), either a symmetric or an anti-symmetric condition is used: $A(x, z) = A(x, -z)$, $\phi(x, z) = -\phi(x, -z)$.

(3) At right ($x = -37\ R_E$) and upper ($z = 21\ R_E$) boundaries, second derivatives of each physical quantity with respect to normal direction are set to zero such that plasmas, along with the magnetic field, can flow out freely. In an effort to minimize the spurious boundary effects, the right boundary is placed farther away from the magnetic dipole than the upper boundary is.

(4) To bypass the difficulty of coupling between ionosphere and magnetosphere, each physical quantity is fixed to its initial value within a region of radius of 2.5 R_E around the earth (at $x = z = 0$). The physical quantities surrounding this region are smoothed such that they match the values in the exterior region smoothly.

2.2.3 Initial configuration

In setting up the initial configuration, an analytical equilibrium configuration of a two-dimensional magnetic dipole embedded in an incompressible flow field [*Kulikovskiy and Lyubimov*, 1965] was used. In this equilibrium, the geomagnetic field, produced by a magnetic dipole placed at $x = 0$ and $z = 0$ pointing in the negative z direction (southward), is confined by the solar wind flow (the incompressible flow) within a cylinder of

radius 10 R_E. The magnetic field $\mathbf{B}$ and flow velocity $\mathbf{v}$ can be expressed as

$$\begin{cases} \mathbf{B} = 0.5B_0 \nabla\left\{ z\left(1+\frac{a^2}{r^3}\right)\right\}, & r \le a; \\ \mathbf{B} = 0, & r > a. \end{cases} \tag{2.3}$$

$$\begin{cases} \mathbf{v} = -v_{sw} \nabla\left\{ x\left(1+\frac{a^2}{r^3}\right)\right\}, & r \ge a; \\ \mathbf{v} = 0, & r < a. \end{cases} \tag{2.4}$$

where $r^2 = x^2 + z^2$, $a = 10\ R_E$, B_0 is the magnitude of the magnetic field at the subsolar point ($x = a$ and $z = 0$), and v_{sw} is the flow speed at infinity. Furthermore, equilibrium requires that $B_0^2 = 4\mu_0 \rho v_{sw}^2$. The corresponding initial configurations expressed in magnetic vector potential and stream function are

$$\begin{cases} A(x,z) = 0.5B_0 x\left(1-\frac{a^2}{r^3}\right), & r \le a; \\ A(x,z) = 0, & r > a. \end{cases} \tag{2.3'}$$

$$\begin{cases} \phi(x,z) = -v_{sw} z\left(1-\frac{a^2}{r^3}\right), & r \ge a; \\ \phi(x,z) = 0, & r < a. \end{cases} \tag{2.4'}$$

Figure 2.3 shows the initial configurations of magnetic field (geomagnetic dipole field) and solar wind stream lines (without IMF) as given by (2.3')-(2.4') in the simulation box.

The model magnetosphere constructed above is, of course, not an exact representation of the real magnetosphere of the earth. However, since the primary interests of the present study are the magnetic reconnection processes occurring at the dayside magnetopause only, the model can be considered as a reasonable initial configuration.

2.2.4 Resistivity Model

The configuration of magnetic reconnection consists of two regions: the diffusion region and the external convection region. In the presence of a finite resistivity, the reconnection of magnetic field lines can occur in the diffusion region. In the earth's

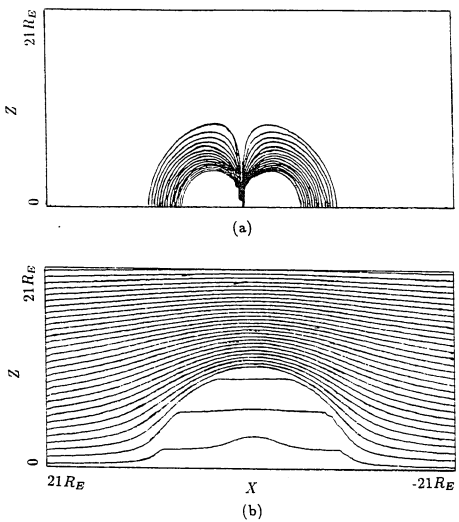

Figure 2.3 Initial configurations of the magnetic field and solar wind flow. (a) Contour of magnetic vector A representing magnetic field lines, (b) Solar wind stream lines.

magnetosphere and in interplanetary space, the collisional resistive effects in the diffusion region are negligible. Strictly speaking, the reconnection processes in the earth's magnetosphere should be treated by a kinetic theory or by particle simulations. In order to apply the simulation result based on MHD equations to the earth's magnetosphere, the so-called "anomalous" resistivity in the diffusion region of the reconnection configuration must be properly determined. An anomalous resistivity may arise either from the particle inertia [*Speiser*, 1970; *Vasyliunas*, 1975; *Sonnerup*, 1979] or from wave-particle interactions in the presence of plasma turbulence [*Coroniti and Eviatar*, 1977; *Huba et al.*, 1978; *Lee*, 1982]. The presence of plasma turbulence in the diffusion region may be caused by plasma instabilities that occur in the magnetic neutral sheet.

To account for the anomalous resistivity, we assume a resistivity of the form

$$\eta(J) = \begin{cases} \alpha(J - J_c)^2 + \eta_b, & \text{if } J > J_c, \\ \eta_b, & \text{otherwise,} \end{cases} \tag{2.5}$$

where α is a constant, J is the total current density, J_c is the critical current density for the enhancement of the local anomalous resistivity, and η_b is a constant background resistivity. Note that the term $\alpha(J - J_c)^2$ represents the current-dependent anomalous resistivity, resulting, for example, from the current-driven instabilities or particle inertia. In the present simulation, the current-dependent anomalous resistivity will be significant only at the magnetopause current sheet. Similar forms of the current-dependent anomalous resistivity have been adopted by other authors in simulating magnetic reconnections using MHD code [*Sato and Hayashi*, 1979; *Ugai*, 1984]. These authors found that the most critical parameter in the current-dependent anomalous resistivity is the threshold current density J_c while the functional form (with the function variable $(J - J_c)$) is not so important.

Corresponding to the constant backgroumd resistivity η_b, the magnetic Reynolds number is defined as $R_m = \mu_0 R_E V_{A0}/\eta_b$, which is based on a scale length of $1R_E$. The

scale length chosen in R_m is of the order of magnitude of the possible reconnection layer thickness in the magnetopause normal direction. One may also choose the scale length to be equal to the scale length of the magnetopause, which is about 10 R_E. Also note that this R_m is based on η_b instead of the total resistivity $\eta(J)$. A magnetic Reynolds number based on the total resistivity $\eta(J)$ will vary with both time and location due to the current-dependent anomalous resistivity term and is not an appropriate parameter to use in the simulation.

2.2.5 Differencing scheme and numerical procedure

The finite differencing approximations of the governing MHD equations inevitably introduce numerical truncation errors. In the simulating magnetic reconnection processes in space plasma, the effects of the numerical truncation errors should be properly treated since the actual resistivity in space plasmas is remarkably small. In magnetic induction equation (2.1), the second term on the right-hand side represents the magnetic field diffusion, which is a critical process in magnetic reconnection. For a very small resistivity η, this term will be small. It is essential that the truncation errors resulting from differencing approximations of other terms in (2.1) and (2.2) be smaller than the magnitude of this term, since one of the major purposes of this simulation study is to investigate the effect of resistivity or magnetic Reynolds number on the dayside reconnection. To reduce the numerical truncation errors, a high-order finite differencing scheme is desirable for the present study.

Bearing this in mind, we developed the following differencing scheme for (2.1) and (2.2):

(a) A two-step method is used to time-center the time derivatives. This gives a second-order accuracy in time step Δt (i.e., the truncation errors $\sim O(\Delta t^2)$).

(b) For the advective terms $\mathbf{v}\cdot\nabla A$ and $\mathbf{v}\cdot\nabla\Omega$, a differencing scheme accurate to the third order in spatial grid size Δx or Δz is used. For purposes of illustration, we write down below the differencing scheme for advective terms in the one-dimensional case

$$(v\frac{\partial f}{\partial x})_i = \begin{cases} v_i\left[\lambda(\frac{\partial f}{\partial x})_i^{center} + (1-\lambda)(\frac{\partial f}{\partial x})_{i-}^{one-sided}\right], & \text{if } v_i \geq 0; \\ v_i\left[\lambda(\frac{\partial f}{\partial x})_i^{center} + (1-\lambda)(\frac{\partial f}{\partial x})_{i+}^{one-sided}\right], & \text{if } v_i < 0. \end{cases} \tag{2.6}$$

where v is the convection speed, $\lambda = 2/3$, and

$$(\frac{\partial f}{\partial x})_i^{center} = [(f_{i+1}-f_i)\frac{x_{i-1}-x_i}{x_{i+1}-x_i} - (f_{i-1}-f_i)\frac{x_{i+1}-x_i}{x_{i-1}-x_i}]/(x_{i-1}-x_{i+1}),$$

$$(\frac{\partial f}{\partial x})_{i-}^{one-sided} = [(f_{i-1}-f_i)\frac{x_{i-2}-x_i}{x_{i-1}-x_i} - (f_{i-2}-f_i)\frac{x_{i-1}-x_i}{x_{i-2}-x_i}]/(x_{i-2}-x_{i-1}),$$

$$(\frac{\partial f}{\partial x})_{i+}^{one-sided} = [(f_{i+1}-f_i)\frac{x_{i+2}-x_i}{x_{i+1}-x_i} - (f_{i+2}-f_i)\frac{x_{i+1}-x_i}{x_{i+2}-x_i}]/(x_{i+2}-x_{i+1}).$$

In the case of uniform grid mesh, (2.6) will be reduced to

$$(v\frac{\partial f}{\partial x})_i = \begin{cases} v_i\left(\lambda\frac{f_{i+1}-f_{i-1}}{2\Delta x} + (1-\lambda)\frac{f_{i-2}+3f_i-4f_{i-1}}{2\Delta x}\right), & \text{if } v_i \geq 0; \\ v_i\left(\lambda\frac{f_{i+1}-f_{i-1}}{2\Delta x} + (1-\lambda)\frac{-f_{i+2}-3f_i+4f_{i+1}}{2\Delta x}\right), & \text{if } v_i < 0. \end{cases} \tag{2.6'}$$

For (2.6'), it can be readily shown that when $\lambda = 2/3$, the truncation error of the differencing scheme in (2.6') for advective terms is of the order of Δx^3.

(c) For the last terms on the right side of (2.1) and (2.2), the usual second-order center-differencing is used.

The subsequent simulation shows that the scheme is stable without the need to use any artificial diffusion terms. In addition, the third-order accuracy differencing scheme for the advective terms makes it possible to simulate reconnection processes with very small resistivity. As a matter of fact, several test cases show that the effect of numerical truncation errors is significant only when the magnetic Reynolds number R_m is larger than ~ 4000.

While the accuracy of the differencing scheme is vital in this study, the efficiency of the simulation code is also important. In particular, for the incompressible MHD simulation, a fast Poisson equation solver can save a large amount of computing time. For each time step in the simulation, the Poisson equation

$$\nabla^2 \phi = \Omega \tag{2.7}$$

needs to be solved to obtain the stream function ϕ from vorticity Ω. In this simulation, due to the nonuniformity of the grid mesh and the unusual boundary conditions of ϕ (zero second-order derivative) on two of the four boundaries, it is complicated to implement a 2-D Poisson solver using direct methods. The usual boundary conditions in direct methods are either Dirichlet conditions ($\phi = 0$) or Neumann conditions ($\partial\phi/\partial n = 0$). Instead, we use the cyclic reduction method (a direct method) in the z direction and an iterative method in the x direction to solve (2.7) first in the z direction and then in the x direction. This Poisson solver proves to be at least twice as fast as the one using an iterative method in both directions.

2.3. Patterns of the Dayside Magnetic Reconnection

Since the first open magnetosphere model [*Dungey*, 1961] was presented, the occurrence of magnetic reconnection at the dayside magnetopause is now widely accepted. However, the patterns, or topologies, of the dayside reconnections remain to be resolved. Experimentally, the satellite observations are sometimes consistent with the large-scale classical steady (or quasi-steady) single X-line reconnection and at other times imply the existence of localized sporadic reconnection. Theoretically, many reconnection models have been proposed, emphasizing different aspects or possibilities of the dayside reconnection: (1) high-latitude (cusp region) reconnection versus low-latitude (subsolar

region) reconnection; (2) large-scale single X-line reconnection (SXR) versus small scale multiple X-line reconnection (MXR); (3) steady-state (most likely quasi-steady state) reconnection versus sporadic and impulsive reconnection. The dayside reconnection patterns depend on: (a) macroscopically, the solar wind conditions and (b) microscopically, the various plasma instabilities in the magnetopause current sheet. One objective of this study is to gain insight into such dependence.

This section presents a parameter study conducted of the dayside reconnection patterns. The parameters used were chosen to be the magnetic Reynolds number R_m, the critical current J_c, and solar wind Alfvén Mach number $M_{Asw} = v_{sw}/V_{Asw}$, where $V_{Asw} = B_{sw}/\sqrt{\mu_0 \rho}$ is the solar wind Alfvén speed. It was found that the dayside reconnections exhibit various patterns depending on the three parameters R_m, M_{Asw} and J_c. For the cases presented below, the common parameters used are: $\alpha = 0.025$ and $v_{sw} = 0.5V_{A0}$

Seven simulation cases are presented in this section. Table 2.2 lists the parameters used for each case and the reconnection type obtained (note that in Table 2.1, MXR denotes multiple X-line reconnection and SXR single X-line reconnection).

TABLE 2.2 Simulation Cases and Parameters Used

cases	B_{sw}	M_{Asw}	R_m	J_c
Case 1 (SXR)	0.25	2	40	∞
Case 2 (MXR)	0.25	2	400	∞
Case 3 (MXR)	0.25	2	4000	∞
Case 4 (MXR)[1]	0.25	2	800	10
Case 5 (MXR)	0.125	4	800	10
Case 6 (MXR)[2]	0.0625	6	800	10
Case 7 (SXR)[3]	0.25	2	4000	*

* see section 2.4

[1] Lee-Fu type MXR.

[2] High latitude MXR.

[3] Bursty SXR.

2.3.1 Effect of magnetic Reynolds number R_m

To investigate the effect of magnetic Reynolds number R_m, three cases (Case 1 to Case 3) were simulated with different R_m (see Table 2.2). For this purpose, the current-dependent anomalous resistivity term in (2.5) is switched off by setting $J_c = \infty$, since a resistivity that varies with both time and location will complicate the study. Therefore, Cases 1 to 3 are for the dayside reconnection with a constant resistivity. In Cases 1 to 3, the ratio of the IMF field strength B_{sw} to the initial geomagnetic field strength B_0 at the subsolar point is 1:4 or $B_{sw} = 0.25B_0$. The corresponding solar wind Alfvén Mach number is then $M_{Asw} = 2$. Therefore, Cases 1 to 3 are cases with a small solar wind Alfvén Mach number.

Case 1: $R_m = 40$

In Case 1, a large constant resistivity $\eta_b = 0.025$, or equivalently a small $R_m = 40$, is used. At $t \geq 0$, the southward IMF with a strength $B_{sw} = 0.25B_0$ is introduced at the left boundary of the simulation box ($x = 21\ R_E$) and is carried by the inflow solar wind plasma towards the dayside magnetopause, which is located at $x = 10\ R_E$ (the speed of the solar wind at the incoming boundary at $x = 21\ R_E$ is $v_{sw} = 0.5V_{A0}$).

Approximately $5t_A$ after the first field line of the IMF reaches the subsolar point ($x = 10\ R_E$ and $z = 0$), magnetic reconnection is observed to occur at the subsolar point. Figure 2.4 shows the contours of constant magnetic vector potential A (magnetic field lines) at $t = 35t_A$ and $t = 46t_A$ in the whole simulation box. Figures 2.5*a* and *b* show the corresponding enlarged snapshots of magnetic field lines and velocity fields near the dayside magnetopause. To maintain a good graphical resolution at the dayside magnetopause, hereinafter we plot only field lines with $-10 < A < 10$ unless otherwise noted (note that both the first field line of the IMF and the outermost field line of the initial geomagnetic field have $A = 0$). In Figure 2.5*b* and hereinafter, the direction of the arrow is that of the plasma velocity and the length of the arrow is proportional to the magnitude of the plasma velocity.

It is seen in Figure 2.4 that by $t = 35t_A$ several of the geomagnetic field lines have been reconnected with IMF lines, forming some open geomagnetic field lines. One end of these newly formed open field lines is rooted in the earth and the other end, which extends deep into the solar wind, is carried by the solar wind flow tailward. This tailward movement of the open field lines drags the whole field line tailward, transferring magnetic flux from the dayside magnetosphere ($x > 0$) to the nightside magnetosphere ($x < 0$). By $t = 46t_A$, an appreciable amount of open magnetic flux has been transferred to the nightside magnetosphere, with open magnetic field lines being

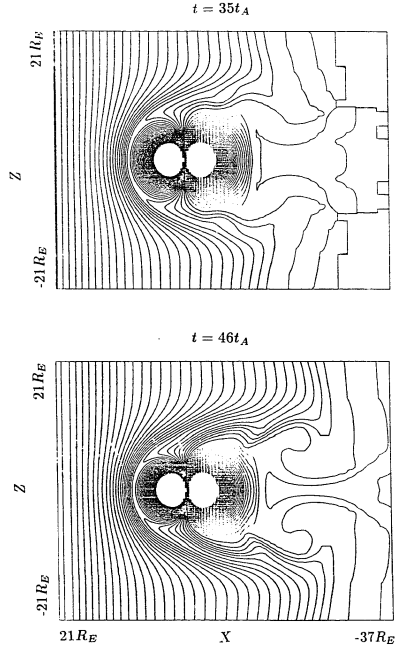

Figure 2.4 Contours of constant magnetic vector potential A (magnetic field lines) of Case 1 at $t = 35t_A$ (upper panel) and $t = 46t_A$ (lower panel). A single X-line at the subsolar point is observed.

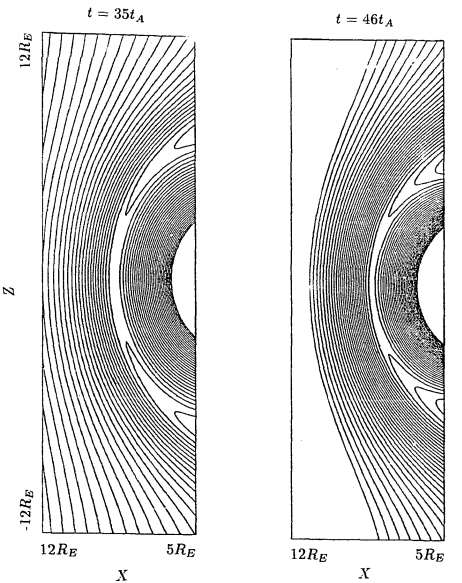

Figure 2.5 (a) Enlarged snapshots of magnetic field configuration near the magnetopause for Case 1 at $t = 35t_A$ and $t = 46t_A$

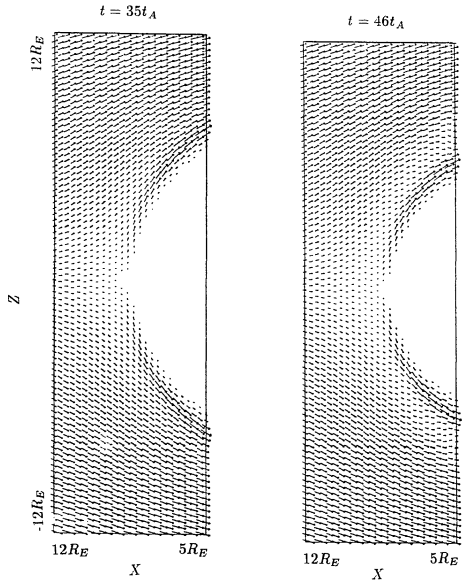

Figure 2.5 (b) Enlarged snapshots of flow patterns for Case 1 at $t = 35t_A$ and $t = 46t_A$. The direction of the arrow is the direction of the velocity vector and the length of the arrow is proportional to the magnitude of the plasma velocity.

draped over the nightside geomagnetic field lines. As a result, the dayside magnetopause is eroded inward by the subsolar-point reconnection. A comparison of magnetic field configurations at $t = 35t_A$ and $t = 46t_A$ in Figure 2.4 shows that the size of the dayside half of the geomagnetic cavity is considerably smaller at $t = 46t_A$ than at $t = 35t_A$. Correspondingly, the subsolar point is measured to move from $x \simeq 8.5\ R_E$ at $t = 35t_A$ to $x \simeq 8\ R_E$ at $t = 46t_A$. The average speed of the earthward movement of the magnetopause due to reconnection is therefore $\sim 0.05R_E/t_A \sim 0.1R_E/min$. The erosion of the magnetopause has been observed [e.g., *Maezawa*, 1974].

Also, as predicted for the dayside single X-line reconnection process by *Levy et al.* [1964], two high-speed plasma jets in the reconnection layers are observed in Case 1. The plasma jets can be easily identified in Figure 2.5*b*. The plasma speed in the plasma jet increases with latitude. At high latitude $\theta > 45°$, the jet plasma speed becomes comparable to the local Alfvén velocity.

To study the magnetic reconnection rate at the subsolar point, we show in Figure 2.6 E_{sp} versus time t, where E_{sp} is the y component of electric field at the subsolar point at time t in the frame of the moving subsolar point. In the simulation, E_{sp} is calculated by

$$E_{sp}(t) = -dA_{sp}(t)/dt, \tag{2.8}$$

where $A_{sp}(t)$ is the value of magnetic vector potential A at the subsolar point at time t. Therefore, $E_{sp}(t)$ represents the time derivative of the magnetic vector potential A at the subsolar point, or the rate of magnetic reconnection at subsolar point. Although the position of the subsolar point is changing with time (moving earthward), $A_{sp}(t)$ can be readily determined by noting that the A value at the subsolar point is always the maximum for the $x > 0$ region due to the specific initial magnetic field configuration (see (2.3′)) used and the boundary condition on A at $x = 21\ R_E$. In the simulation,

the maximum value of $A(x > 0, z = 0, t)$ (i.e., along the central symmetric line $z = 0$ for the dayside part $x > 0$) is recorded as a function of time t and then used as the magnetic vector potential value $A_{sp}(t)$ at the subsolar point.

In Figure 2.6, it is seen that E_{sp} increases monotonically with time from zero at $t = 0$ to ~ 0.08 at $t = 40t_A$ and maintains approximately the same value from $t = 40t_A$ to $t = 46t_A$. Hence, the reconnection during the time interval $t = 0$–$40t_A$ is a transient process. After $t = 40t_A$, the reconnection process may be considered as being in a local quasi-steady state near the reconnection site. Theoretically, a 2-D steady-state reconnection process can be defined by a constant electric field perpendicular to the 2-D plane everywhere [e.g., *Vasyliunas*, 1975]. Hence, one convenient way to determine whether a 2-D reconnection process is in a steady state is to check the electric field distribution. Figure 2.7*a* shows the contours of the electric field y component E_y near the magnetopause at $t = 35t_A$ and $t = 46t_A$ and Figure 2.7*b* is the corresponding 3-D plot of E_y distribution. E_y is calculated by Ohm's Law

$$E_y = -(\mathbf{v} \times \mathbf{B})_y + \eta J_y, \tag{2.9}$$

where J_y is the y component of the current density. It is seen in Figure 2.7 that E_y is almost constant outside and inside the magnetopause reconnection layer in Case 1. Throughout the region outside the magnetopause reconnection layer $E_y \sim 0.125$, which is the value of electric field imposed at the incoming boundary of the IMF where $E_y = B_{sw} v_{sw} = 0.125$. In the region outside the magnetopause reconnection layer, since the current density is negligible (see Figure 2.9 below), a nearly constant E_y distribution suggests that the IMF flux transport towards the magnetopause in Case 1 has reached a quasi-steady state by $t = 35t_A$. Across the magnetopause reconnection layer, E_y drops considerably, implying that the penetration of E_y from the solar wind into the magnetosphere is very small.

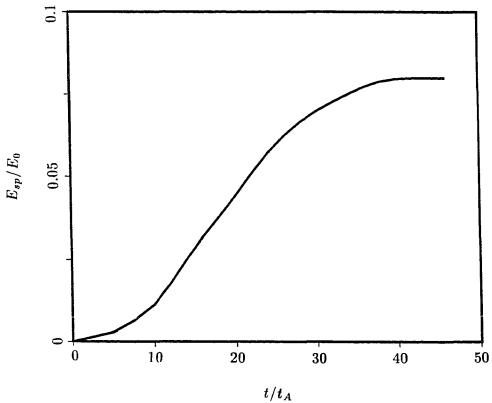

Figure 2.6 Magnetic reconnection rate at the subsolar point as a function of time for Case 1 ($R_m = 40$). E_{sp} is the y-component of the electric field at the subsolar point and E_0 is the normalization unit of the electric field. E_{sp} here is defined as the magnetic reconnection rate at the subsolar point.

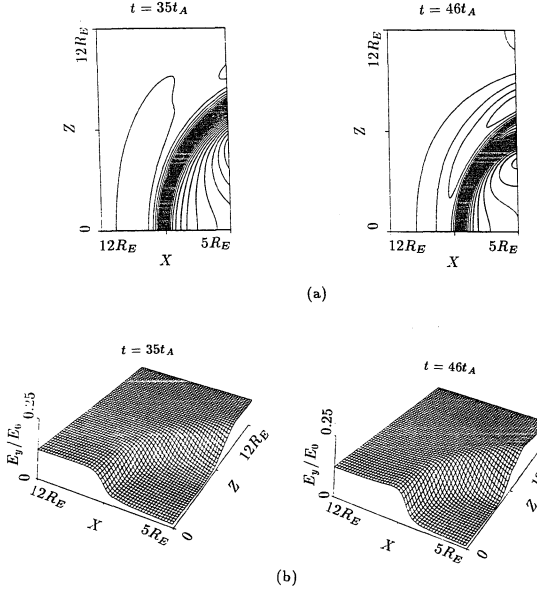

Figure 2.7 Electric field E_y (y-component) distributions at $t = 35t_A$ and $t = 46t_A$ near the dayside magnetopause in Case 1 (only the northern hemisphere half is plotted). (a) Contour lines of E_y; (b) 3-D profile of E_y.

Therefore, in the 2-D case, a steady state of the single X-line reconnection at the dayside magnetopause cannot be reached in the usual sense over a global scale (for example, 10 R_E), since a large drop in E_y value is expected across the magnetopause. However, in case of a constant reconnection rate, a local steady-state subsolar reconnection should exist in the frame of the moving magnetopause. In Case 1, the reconnection rate at the subsolar point is approximately a constant for $t > 40t_A$ as shown in Figure 2.6. By using the above estimated earthward moving speed of the subsolar magnetopause, we transform E_y to E'_y in the frame of the moving magnetopause at the subsolar point

$$E'_y = -[(\mathbf{v} - \mathbf{v}_m) \times \mathbf{B}]_y + \eta J_y, \tag{2.10}$$

where $\mathbf{v}_m$ is defined as the moving speed of the magnetopause at the subsolar point. Figure 2.8 shows the electric fields E_y and E'_y across the magnetopause along the $z = 0$ line for $t = 46t_A$. In calculating E'_y by (2.10), we use $\mathbf{v}_m = -0.05\hat{\mathbf{x}}$ estimated (see above) as the average moving speed of the subsolar magnetopause for $t > 35t_A$. Figure 2.8 shows that, in the rest frame, E_y drops sharply across the magnetopause at $x \sim 8.5$ R_E from $E_y \sim 0.125$ at $x = 12$ R_E down to $E_y \sim 0.02$ at $x = 5$ R_E. However, in the frame moving at $\mathbf{v}_m$, the variation of E'_y is much reduced ($E'_y \sim 0.1$ at $x = 12$ R_E and $E'_y \sim 0.13$ at $x = 5$ R_E). In particular, near the magnetopause at $x \sim 8.5$ R_E, the sharp jump of E_y is now replaced by a smooth transition of E'_y. Hence the reconnection around $t = 46t_A$ can be considered as a quasi-steady process in the region near the subsolar point. Likewise, in other situations where the reconnection sites are moving, a steady state of the reconnection process can only be defined in the moving frame.

Figure 2.9*a* shows contours of the current density J_y (y-component) at $t = 35t_A$ and $46t_A$ around the magnetopause and Figure 2.9*b* shows the corresponding 3-D plots

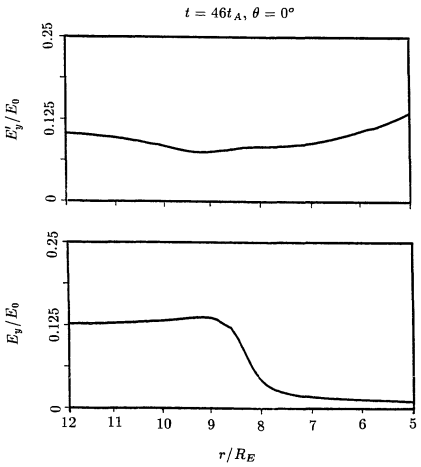

Figure 2.8 Profile of electric field E_y and E'_y across the magnetopause at latitude $\theta = 0^o$ and $t = 46t_A$ for Case 1. E'_y is the electric field in the rest frame and E'_y is the electric field in the frame moving with the magnetopause at the subsolar point.

of the J_y distribution. It is seen that the current density peaks at the subsolar point and gradually decreases with increasing latitude. At $t = 46t_A$, the current sheet begins to bifurcate at high latitude, while at $t = 35t_A$ the bifurcation of the current sheet is still small. In the traditional single X- line reconnection model [e.g., *Petschek*, 1964], a pair of slow mode shocks is supposed to be present, bounding the reconnection layer or magnetic field reversal region. Corresponding to this pair of slow shocks, a pair of current sheets is formed, across which plasmas are accelerated by the resultant Lorentz force. For $t = 46t_A$ in Case 1, the region where the current sheet bifurcates may be considered as corresponding to the pair of slow shocks in the compressible MHD situation. Note that the current density of the two branches of the bifurcated current sheets at $t = 46t_A$ is weak compared to that at the subsolar point. The low current density indicates that the corresponding discontinuities (slow shocks in the compressible case), if they exist, are weak. This may be due to the large magnetic diffusion caused by the small magnetic Reynolds number $R_m = 40$. Another single X-line reconnection model proposed particularly for the dayside reconnection is that by *Levy et al.* [1964]. Levy et al.'s model is an asymmetric one in which only one MHD discontinuity, a rotational discontinuity, is needed to accomplish the magnetic field reversal. However, our simulation data (not presented here) at the dayside magnetopause do not fit the Walén relation [*Walén*, 1944], which *Papamastorakis et al.* [1989] used as a test of dayside rotational discontinuity. This indicates that the reconnection layer in Case 1 is unlikely to consist of the type of rotational discontinuity proposed in Levy et al.'s model. This contradiction may be due to the incompressible simplification in the present simulation. A more realistic dayside magnetopause reconnection simulation should include the density asymmetry; in the present incompressible simulation, the density has been assumed constant everywhere.

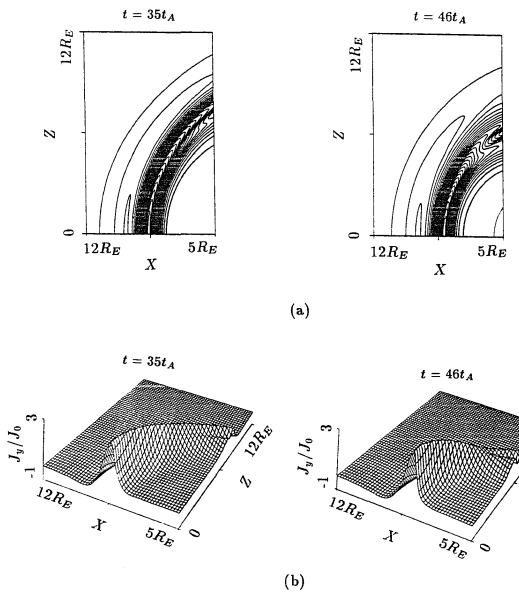

Figure 2.9 Distribution of the current near the dayside magnetopause at $t = 35t_A$ and $t = 46t_A$ in Case 1 (northern hemisphere half). (a) Contour of current density J_y; (b) 3-D profile of J_y.

Case 2 and Case 3: $R_m = 400$ *and* 4000

In Case 2, the magnetic Reynolds number is increased to $R_m = 400$, an order of magnitude larger than in Case 1. All other parameters are the same as in Case 1. Instead of the subsolar reconnection as in Case 1, a long magnetopause current sheet is formed in Case 2. Magnetic reconnections are later observed to occur at two sites located to the north and south of the subsolar point. As a result, a magnetic island is formed centered at the subsolar point.

Figure 2.10*a* shows the magnetic field configuration of Case 2 at $t = 24t_A$, in which a long current sheet is found to exist. Figure 2.10*b* is the corresponding enlarged snapshot near the dayside magnetopause. Note that in Figures 2.10 to 2.12, only the upper part of the simulation region is plotted and the lower part is a symmetric (or antisymmetric) reflection of the upper part. The long current sheet in Figure 2.10 is measured to have a thickness of $\sim 0.6\ R_E$ at the subsolar point. By $t = 36t_A$, as shown in Figure 2.11*a*, reconnection occurs in the northern hemisphere part of the magnetopause at a latitude of $\sim 30°$. By symmetry, reconnection also occurs in the southern hemisphere magnetopause current layer at the same latitude. As a result, a magnetic island is formed around the subsolar point. Above and below the reconnection sites in the northern and southern hemisphere, respectively, the reconnected geomagnetic field lines become open field lines and are pulled tailward. Figures 2.11*b* and c are the enlarged snapshot of magnetic field and velocity field near the magnetopause. In Figure 2.11c, a high-velocity jet of plasma can be seen to be associated with the reconnection layer to the north of the reconnection site in the northern hemisphere. In this layer, the plasmas are accelerated by the northward tension force of the open geomagnetic field lines. Therefore, as in Dungey's subsolar point single X-line reconnection model, multiple

X-line reconnections of the type in Case 2 can also produce a high-velocity plasma jet, except that the jet is likely to be found only in the high-latitude region.

In Case 3, we further increase the magnetic Reynolds number to $R_m = 4000$. Again magnetic reconnections are observed to occur above and below the subsolar point. A magnetic island is formed around the subsolar point. Figure 2.12*a* shows the magnetic field configuration at $t = 36t_A$ for Case 3. Figure 2.12*b* shows the enlarged snapshot near the magnetopause. The magnetic field configuration near the magnetopause in Case 3 is similar to that in Case 2, except that the magnetic island in Case 3 is larger than in Case 2 at the same simulation time ($t = 36t_A$).

The larger size of the magnetic island in Case 3 is probably caused by the smaller magnetic diffusion in the presence of a smaller resistivity ($\eta_b = 0.0025$). Although there is no magnetic field line reconnection at the center of magnetic island, annihilation of magnetic field lines can take place through the magnetic diffusion process. To determine quantitatively the effect of the diffusion process at the center of the magnetic islands formed in Case 2 and Case 3, we inspected the variation of the magnetic vector potential A at the center of these magnetic islands. Let us define $A_c(t)$ and $E_c(t) = -\partial A_c(t)/\partial t$ as the magnetic vector potential and the y component of electric field at the center of magnetic islands, respectively. Then, as in Case 1, $A_c(t)$ will be equal to the maximum of $A(x > 0, z = 0, t)$. From the simulation data, the average value of $E_c(t)$, $\bar{E}_c$, is calculated (the average is made during the period of the time after the formation of the magnetic island). It is found that $\bar{E}_c(t) \sim 0.02$ in Case 2 and $\bar{E}_c(t) \sim 0.003$ in Case 3. For comparison, at the boundary $x = 21\ R_E$, the IMF flux input rate $|\partial A/\partial t| = v_{sw}B_{sw} = 0.125$. Hence, the field annihilation rate in the magnetic island is about 16% of the IMF flux input rate in Case 2, while this percentage is only about 2.4% in Case 3. It is, therefore, suggested tentatively that the larger size of the magnetic

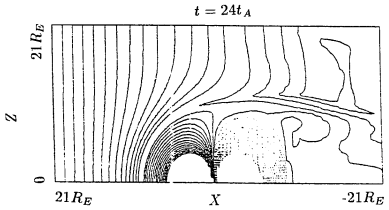

Figure 2.10 Magnetic field configuration (northern hemisphere half) at $t = 24t_A$ in Case 2 ($R_m = 400$). (a) Global picture; (b) Enlarged snapshot near the magnetopause.

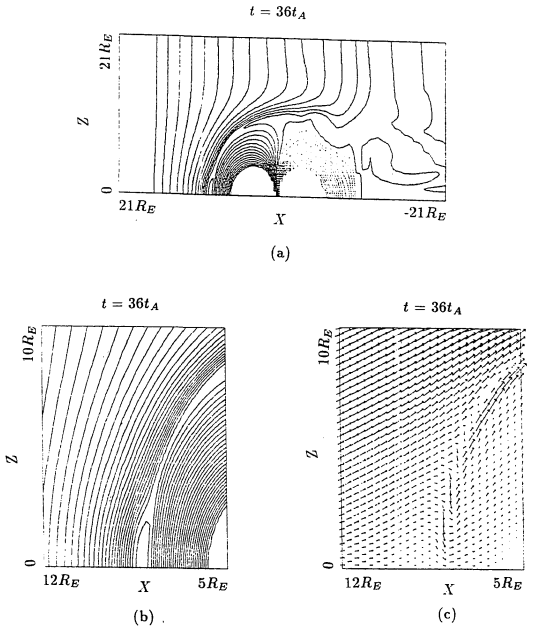

Figure 2.11 Magnetic field configuration and plasma flow pattern (northern hemisphere) at $t = 36t_A$ in Case 2. (a) The global magnetic field configuration; (b) Enlarged snapshot of magnetic field configuration near the magnetopause; (c) Plasma flow patterns near the magnetopause.

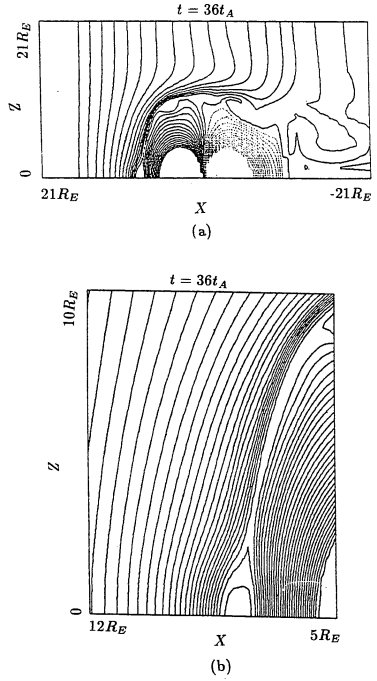

Figure 2.12 Magnetic field configurations (northern hemisphere) at $t = 36t_A$ in Case 3 ($R_m = 4000$). (a) Global picture; (b) Enlarged snapshot near the dayside magnetopause.

island in Case 3 is due to the smaller magnetic diffusion in the magnetic island of Case 3.

In the present north-south symmetric situation, the magnetic islands in Case 2 and Case 3 will split later at the subsolar point, resulting in two small islands which then move away from the subsolar point region in the northward and southward directions, respectively. This island splitting process at the stagnation flow point is common in local simulations of multiple X-line reconnections [e.g, *Lee and Fu*, 1986*a*]. Later in this chapter, the island splitting process will be shown in Case 7.

The role of magnetic Reynolds number and the formation of magnetic islands

Cases 1 to 3 indicate that the magnetic Reynolds number R_m is a physical parameter which may be able to control the general patterns of the dayside magnetic reconnections, namely, whether the traditional single X-line reconnection or the multiple X-line reconnections [e.g., *Lee and Fu*, 1986*a*]. Here the multiple X-line reconnections (MXR) is used as a general term to refer to any reconnection processes with more than one reconnection site. From the simulation cases, it could be concluded, at least in the 2-D geometry, that the larger the magnetic Reynolds number is at the dayside magnetopause, the more likely the dayside magnetic reconnection will occur at several sites, forming magnetic islands along the magnetopause. This is qualitatively consistent with the simulation results of *Lee and Fu* [1986*a*]. Using MHD simulations, *Lee and Fu* [1986*a*] have studied criteria for the transition of reconnection patterns from the single X-line to the multiple X-line reconnection in a 2-D slab model of a current sheet with imposed inflow boundary conditions. Empirically, Lee and Fu discovered that multiple

X-line reconnections tend to occur in a current sheet which satisfies

$$l/\delta > 10, \tag{2.11}$$

where l and and δ are the half-length and half-thickness of the current sheet, respectively. They found that, in addition to the boundary inflow speed and simulation box size, the magnetic Reynolds number is an important physical parameter which is responsible for the scale of the current sheet. Specifically, they obtain the following empirical relationship (under a constant inflow speed and fixed simulation box size)

$$l/\delta \propto R_m^{1/4}. \tag{2.12}$$

Equations (2.11) and (2.12) together suggest that as the magnetic Reynolds number R_m in a current sheet increases, the reconnection pattern is likely to make a transition from the single X-line type to the multiple X-line type.

In Case 1 the magnetic reconnection occurs immediately after the leading IMF field lines reach the subsolar point. No current sheet is seen to be formed at the beginning of the reconnection, although later (see Figures 2.4 and 2.5) the initial reconnection site (X point) is stretched into a short current sheet, the l/δ ratio of which is much less than 10 ($l/\delta \sim 4$ at $t = 35t_A$ and $l/\delta \sim 2.5$ at $t = 46t_A$). Consistent with criterion (2.11), the current sheet resulting from the single X-line reconnection in Case 1 is stable throughout the simulation. In fact, as noted above, the reconnection reaches a quasi-steady state after $t \sim 40t_A$. However, in Cases 2 and 3 with a larger magnetic Reynolds number R_m, long current sheets are formed before the onset of reconnections. In Case 2 at $t = 24t_A$ (Figure 9), the ratio $l/\delta \sim 20$ while in Case 3 this ratio (before reconnections) is even larger (not shown). As predicted by criterion (2.11), magnetic islands are later observed to be formed in Cases 2 and 3.

The formation of magnetic islands in a current sheet is sometimes referred to as chaotic behavior [e.g., *Forbes and Priest*, 1987] of magnetic reconnections in contrast to the steady state single X-line reconnections. The occurrence of this chaotic behavior in a current sheet is also observed in local simulations by others [*Biskamp*, 1982; *Forbes and Priest*, 1983; *Mathaeus and Lamkin*, 1985; *Scholer and Roth*, 1987]. It is generally held that such chaotic behavior is due to tearing-like instabilities in the current sheet. However, in most reconnection situations, there are plasma flows in the current sheet or diffusion region. Therefore, in addition to the ordinary tearing-mode instability criterion [*Furth et al.*, 1963], it has been suggested [e.g., *Sonnerup and Sakai*, 1981; *Sakai*, 1983] that the onset of the tearing-like instability also requires that the e-folding time for the tearing instability must be shorter than the convection time during which plasmas are convected out of the diffusion region. Based on these two conditions for the formation of magnetic islands in a current with plasma flow, *Lee and Fu* [1986*a*] derived a criterion for the tearing-like instability. The criterion they obtained was found to be in good agreement with the empirical one (i.e., (2.11)). This suggests that a tearing-like instability in a current sheet is a possible mechanism for the impulsive reconnections that can lead to the formation of magnetic islands. Simulation results in this chapter seem to support this school of argument. In Cases 2 and 3, a large magnetic Reynolds number ($R_m > 400$) leads to the formation of long current sheets. By criterion (2.11), this long current sheet is susceptible to tearing-like instability. The onset of tearing-like instability in turn will trigger the impulsive reconnections, resulting in the formation of magnetic islands. On the other hand, if the formation of the magnetic islands in Cases 2 and 3 was due to the tearing instability, the island scales in the north-south direction would be close to the wavelength of the unstable tearing mode. According to the linear theory of tearing instability, the wavelength λ of the unstable mode is given by $2\pi\delta/\lambda \sim 0.5$ [e.g., *Furth et al.*, 1963]. In Cases 2 and 3, the half-thickness of the

magnetopause current sheet before reconnections is $\delta \sim 0.3R_E$ (see Figure 2.10 for Case 2; the current sheet of Case 3 is not shown). Hence, in Cases 2 and 3, the wavelength of the unstable tearing mode is given as $\lambda \sim 5R_E$. From Figures 2.11 and 2.12, it is seen that the obtained wavelength λ is approximately the length of the magnetic islands in the north-south direction.

While a tearing-like instability seems to be a plausible candidate responsible for the magnetic island formation, other possibilities should not be overlooked. For example, given the presence of a long dayside magnetopause current sheet, the non-uniformity of the solar wind pressure and the stresses of the IMF exerted on the magnetopause surface may cause local fluctuations in the current sheets and, consequently, reconnections may also be triggered at several points without the need to invoke the tearing-like instability. In Cases 2 and 3, the pre-reconnection conditions of the magnetopause current sheet have been examined carefully. It was found that immediately before the reconnection, the current sheets in both cases are pinched heavily at two mid-latitude symmetric points in the northern and southern hemispheres, respectively, which later become the reconnection sites. Figure 2.13 shows the time variation of the magnetopause current sheet in Case 3 before the occurrence of magnetic reconnections. In Figure 2.13, J_{mp} is the current density of the magnetopause current layer and is plotted as a function of the latitude θ. Only the northern part of the magnetopause current sheet is plotted. It is seen in Figure 2.13 that at $t = 19t_A$, the maximum of J_{mp} occurs at the subsolar point ($\theta = 0^o$). At $t = 25t_A$, the J_{mp} distribution profile changes little except for an overall increase in the magnitude of J_{mp} along the current sheet. However, by $t = 31t_A$, the J_{mp} distribution profile is drastically changed with the maximum of J_{mp} shifted to $\theta \sim 30^o$. The large peak of J_{mp} at $t = 31t_A$ shows the location where the pinch of the magnetopause current sheet by the solar wind and IMF is the largest. Later, magnetic reconnection is found to occur in the northern hemisphere at approximately the same

location corresponding to the maximum J_{mp} at $t = 31t_A$. By symmetry, the southern hemisphere current sheet evolves in the same way. In Case 2, the time variation of the magnetopause current sheet is similar. Two other cases were run with the same parameters as that in Case 3 except the IMF magnitude was reduced by a factor of 1/2 and 1/4, respectively. In these two cases, the similar local current sheet pinch at higher latitude is found. These cases show that the subsequent reconnection sites are near the points in the magnetopause current sheet where the pinch is the largest. However, it is still unclear whether this pinch is related to the unstable tearing mode or is caused by the solar wind pressure and IMF stresses.

Whether the multiple X-line reconnections or the formation of magnetic islands at the dayside magnetopause are caused by the tearing-like instability or other effects, the formation of magnetic islands in our simulation (Cases 2 and 3) is directly related to the formation of a long current sheet, which is related to the large magnetic Reynolds number R_m. Observationally, the dayside magnetopause is very long. This is also very likely a consequence of the small resistivity in space plasma. Therefore, as is suggested by our simulation and the above-cited works, the dayside magnetopause reconnections may favor the impulsive reconnection processes such as multiple X-line reconnections. On the other hand, though steady-state single X-line reconnection is unlikely, at the dayside magnetopause which has a long current sheet, impulsive single X-line reconnections [*Southwood et al.*, 1988; *Scholer*, 1988*a*] may also be possible. In section 4, a simulation case of the impulsive single X-line reconnections will be shown.

2.3.2 Effect of current-dependent resistivity: Case 4

As discussed in subsection 2.2.4, at the dayside magnetopause, the classical resistivity derived from plasma collisional effects is negligible. Therefore, the assumption of the

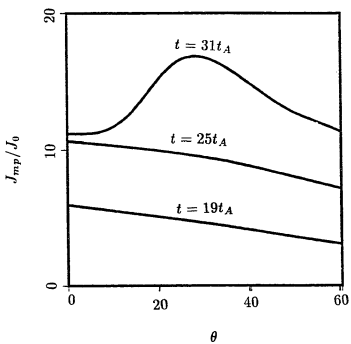

Figure 2.13 Profile of the current density in the dayside magnetopause current layer in Case 3 at three different times $t = 19t_A$, $25t_A$, and $31t_A$. J_{mp} is the current density in the magnetopause and θ is the latitude.

existence of an anomalous resistivity is essential in studying the dayside magnetic reconnections by MHD theory. Since it is still impossible to obtain a general expression for anomalous resistivity in the diffusion region, many MHD simulations of magnetic reconnections simply assume a constant resistivity (independent of time and space). A more sophisticated resistivity model used widely in MHD simulations is a current-dependent resistivity which, in most cases, is a function of both time and space. In subsection 2.3.1, the dayside reconnection processes with a constant resistivity have been studied by setting $J_c = \infty$ in equation (2.5). There are basically only two types of dayside reconnection patterns observed in the simulations with a constant resistivity (Cases 1 to 3): (1) the subsolar point single X-line reconnection for a small magnetic Reynolds number ($R_m = 40$), and (2) the two X-line reconnection which forms one magnetic island centered at the subsolar point when the magnetic Reynolds number is large ($R_m \geq 400$). In reality, the anomalous resistivity, if any, in the long and thin dayside magnetopause may vary with both time and space. In the presence of such an anomalous resistivity, magnetic reconnections may exhibit diverse patterns at the dayside magnetopause because of its sensitivity to resistivity, as presented below.

This subsection will study the effect of time-and-space dependent resistivity on the dayside reconnection patterns by introducing the current-dependent resistivity term in (2.5). The constant background resistivity η_b in this subsection is set small, $\eta_b \leq 0.00125$ or $R_m \geq 800$. The critical current density in (2.5) is set to $J_c = 10J_0$. This value of J_c is so chosen that a long and relatively uniform magnetopause current sheet can be formed before the onset of magnetic reconnections at any point. As the dayside magnetopause is usually observed to be long and thin, it is expected that magnetic reconnections occurring in a pre-existing long magnetopause current sheet would constitute the majority of dayside reconnections. With $J_c = 10$ and $\eta_b = 0.00125$, Case 4 will show how a magnetopause, which is a tangential discontinuity, can be disrupted by magnetic

reconnections triggered by current-dependent resistivity. All parameters, except η_b and J_c, in Case 4 are the same as in Cases 1 to 3.

Figure 2.14 shows the global picture of magnetic fields at different simulation times. At $t = 26t_A$, a long current sheet is formed along the magnetopause as in Cases 2 and 3 due to the small η_b. Meanwhile, the interplanetary magnetic fields are piled up in front of the magnetopause. Since no reconnections occur at this time, the magnetic fields on both sides of the magnetopause have a tangential component only. As will be shown in Figure 2.16, plasmas flows at the magnetopause also have only a tangential component. Hence, the magnetopause is considered to be a tangential discontinuity. However, since the average current density along the magnetopause at $t = 26t_A$ is approximately the value of J_c $(= 10J_0)$, the magnetopause boundary is now at the critical point of being disrupted by the onset of magnetic reconnections. As time goes on, more interplanetary magnetic fields carried by the solar wind pile up in front of the magnetopause. The pile-up further enhances the magnetopause current density. At $t = 29t_A$, magnetic reconnections are observed to occur along three X lines, one of which is exactly at the subsolar point with the other two located at latitude $\theta \sim \pm 10^o$. Correspondingly, two small magnetic bubble-shaped structures appear on each side of the subsolar point. The high-latitude portions of the magnetopause boundary above and below $\theta \sim \pm 10^o$ remain approximately tangential discontinuities but the magnetopause is no longer a closed one. By $t = 31t_A$, the original pair of magnetic bubbles have grown into a pair of large-sized magnetic islands, while another pair of magnetic islands have formed above and below the old pair. In the process of formation and growth of magnetic islands, the center of the magnetic islands keeps moving poleward. By $t = 36t_A$, the two pairs of magnetic islands have been convected a distance away from the subsolar point region. The reconnection site at the subsolar point is now stretched and starts to form a new current sheet. In the whole process, while the subsolar point reconnection site is fixed,

the other reconnection sites are moving poleward along with the magnetic islands. A comparison with the previous cases having constant small background resistivity (Cases 2 and 3) indicates that the time-and-space dependent anomalous resistivity can change dayside reconnection patterns significantly.

Figure 2.15 shows the corresponding enlarged snapshots of the magnetic configuration near the magnetopause. A close look at the magnetic island configurations shows that each magnetic island is wrapped by open field lines (geomagnetic field lines connected to the interplanetary magnetic field lines). This is especially clear at $t = 31t_A$ and $t = 36t_A$. The poleward tension force produced by these open field lines may contribute to the total poleward forces exerted on the magnetic islands and may be responsible for the poleward motion of magnetic islands. Also note that the magnetic islands compress the part of closed geomagnetic field lines close to the magnetopause, generating magnetic ripples on the closed geomagnetic field lines. Along with the poleward-moving magnetic islands, these magnetic ripples also propagate poleward. Hence, *Lee et al.* [1988] have proposed that dayside magnetic reconnections may be one of the energy sources of ultra-low frequency waves observed in the high-latitude cusp region (for more discussion, see section 2.5). Figure 2.16 shows the flow patterns of Case 4 near the dayside magnetopause. One interesting feature of the flow patterns is the enhanced plasma flow speed associated with each moving magnetic island: the magnetic islands are moving poleward at a faster speed than the ambient plasmas. This property of plasma flows resulting from the dayside reconnection will be further discussed later in relation to flux transfer events (FTEs).

Figure 2.17 shows the distribution of the current density J_y near the magnetopause at different times (only the northern hemisphere part is plotted), while Figure 2.18 shows the corresponding 3-D plots of the current density. At $t = 26t_A$, the current sheet is long and the current density is approximately constant along the whole current

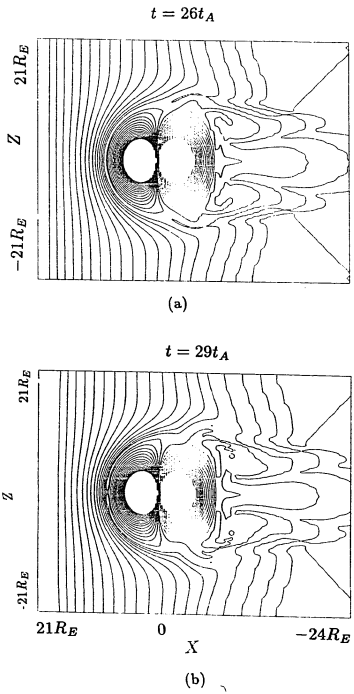

Figure 2.14 Global evolution of the magnetic configuration in Case 4 (a) at $t = 26t_A$, (b) at $t = 29t_A$.

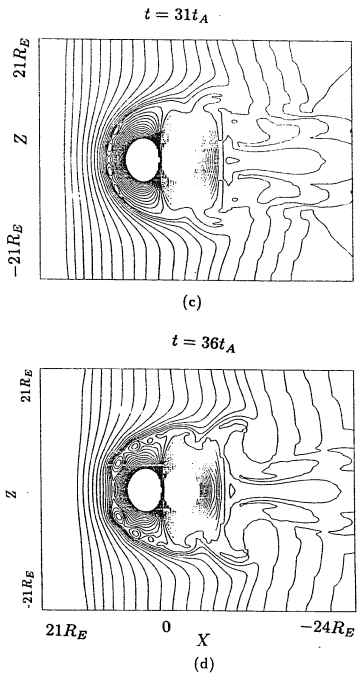

Figure 2.14 Global evolution of the magnetic configuration in Case 4 (c) at $t = 31t_A$, (d) at $t = 36t_A$.

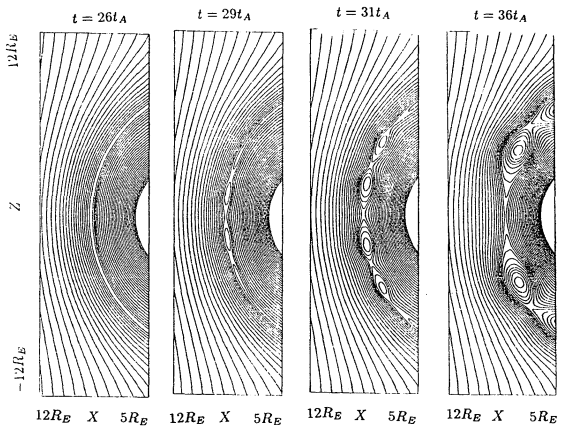

Figure 2.15 Enlarged snapshots of magnetic configurations at four different times near the magnetopause in Case 4.

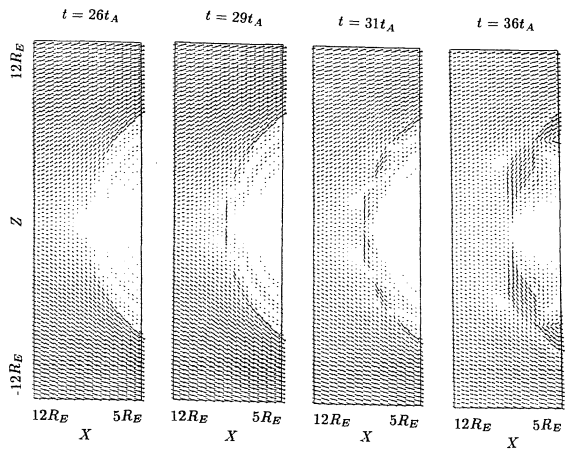

Figure 2.16 Plasma flow patterns near the magnetopause at four different times in Case 4.

sheet. In response to the onset of reconnections at $t = 29t_A$, the current sheet changes accordingly. At $t = 31t_A$, the magnetic islands have already grown to larger sizes and changes in the current sheet structure can be clearly seen. The previous thin current sheet is now dilated where magnetic islands have formed, and layered structures of current sheet begin to appear inside magnetic islands. The originally one-layer current sheet now bifurcates into two layers to encircle each island. The bifurcation of the current sheet is especially clear at $t = 36t_A$. Furthermore, it will be demonstrated later in this subsection, plasmas across the two current layers bounding the equatorward portion of the low-latitude magnetic islands are accelerated to a high speed. These two current layers resemble those from the classical Petschek type single X-line reconnection, in which a pair of slow shocks (corresponding to a pair of current layers) are attached to the diffusion region. *Petschek* [1964] argued that in a reconnection process most plasmas are accelerated by slow shocks. The enhanced plasma flow speed associated with magnetic islands may also be caused by the same acceleration mechanism.

Figure 2.19 shows the electric field E_y distributions near the magnetopause at different times. E_y here is calculated by (2.9). Figure 2.20 is the corresponding 3-D plot of Figure 2.19. Before the reconnection at $t = 26t_A$, E_y drops uniformly across the magnetopause boundary similar to Case 1. This relatively uniform profile of E_y is changed tremendously by the formation of the magnetic islands. It is seen from Figure 2.20 and Figure 2.19 that associated with each magnetic island, E_y in the equatorward portion of the island is increased while E_y in the poleward portion is reduced. Correspondingly, in Figure 2.20, a bump is seen in the equatorward portion of the magnetic island and a dip appears in the poleward portion of the magnetic island with two deeper dips located on the two sides. This feature of E_y associated with magnetic islands is common to all magnetic islands. As will be shown below, the E_y value in the poleward portion of these magnetic islands is negative (dusk to dawn) while the E_y value in the equatorward

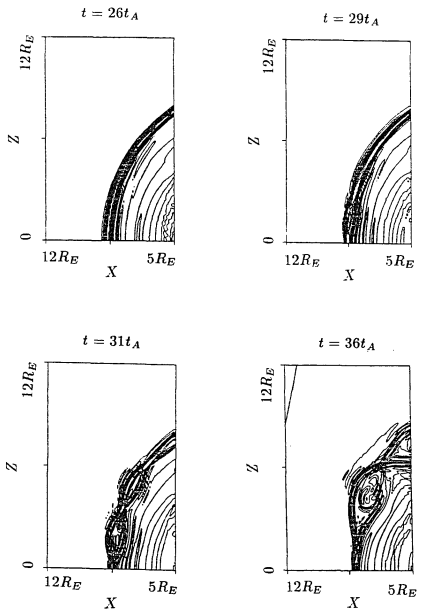

Figure 2.17 Contour of current density J_y near the magnetopause (northern hemisphere) at four different simulation times in Case 4.

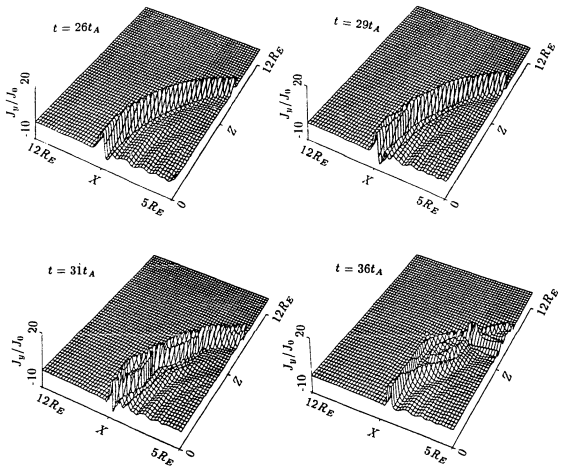

Figure 2.18 The corresponding 3-D profiles of current density J_y in Figure 2.17.

portion is positive (dawn to dusk). This bipolar feature of E_y is consistent with the poleward motion of the magnetic islands. In the magnetic island, the resistivity is small (see Figure 2.23 and discussion therein). Therefore, the magnitude of E_y is associated with the first term on the right-hand side of equation (2.9) (i.e., E_y in the island consists of, roughly, the convection electric field only). In Figure 2.16, the enhanced plasma flows in magnetic islands are seen to be approximately along the tangential direction of the unperturbed magnetopause boundary. Hence, a bipolar structure of the magnetic normal components associated with a magnetic island would naturally suggest a bipolar structure for the induced electric field. Note that in the dayside single X-line reconnection as observed in Case 1, E_y throughout the whole reconnection region is of the same sign as that of the IMF, i.e., dawn to dusk.

In the following, the fine structures of magnetic islands formed along the magnetopause will be studied. To save time, the lower magnetic island formed at $t = 36t_A$ in the northern hemisphere is selected as an example. Figure 2.21 maps the diagnostic lines (solid lines) onto a background of magnetic field configuration (dashed line contour) at $t = 36t_A$. Four diagnostic lines (labelled in Figure 2.21 as lines aa', bb', cc', and dd') are in the radial direction across the magnetopause extending from $r = 7R_E$ to $r = 11R_E$ and with latitudes of $\theta = 10^o, 20^o, 30^o$, and 40^o, respectively. Diagnostic line ee' is in the polar direction from $\theta = 10^o$–50^o at $r = 9R_E$. One of the widely used methods to present the experimental magnetic field and plasma velocity data near the magnetopause is to decompose vectors into the so-called boundary normal coordinates [*Sonnerup and Cahill*, 1967; *Russell and Elphic*, 1978] in which one axis is in the normal direction of the magnetopause surface and the other two axes lie in a plane perpendicular to the normal direction of the magnetopause surface. The three axes in the boundary normal coordinate system then form a local Cartesian coordinate system. In the magnetopause boundary normal coordinates, the magnetopause normal direction

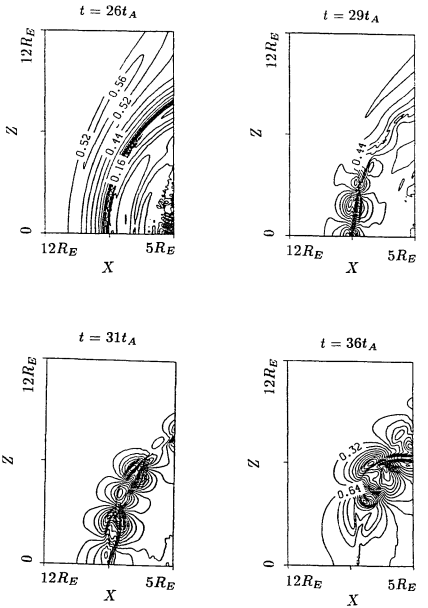

Figure 2.19 Contour of electric field E_y near the dayside magnetopause (northern hemisphere) at four different times in Case 4.

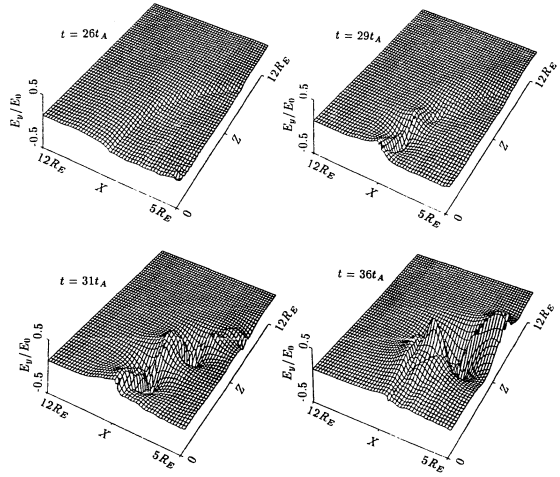

Figure 2.20 Corresponding 3-D profile of E_y distribution in Figure 2.19.

is found by the so-called minimum variance method [*Sonnerup and Cahill*, 1967]. The presentation of simulation data along the diagnostic lines shown above will not use the boundary normal coordinate system. Instead, the vector quantities in the simulation plane are decomposed into the radial component and azimuthal component. Recall that the initial magnetopause boundary of this simulation is on a circle with $r = 10R_E$. Hence, as a good approximation in this simulation, the radial direction is used as the magnetopause normal direction and the azimuthal direction as the tangential direction. In this coordinate system, the positive radial direction is designated as pointing away from the earth and the positive azimuthal direction point from low latitude to high latitude. The simulation data presented below and later in this chapter indicate that this simple procedure gives a good approximation for the present simulation. Figures 2.22*a* to 2.22*e* present J_y, **B**, **v**, and E_y measured along the five diagnostic lines in Figure 2.21: lines aa', bb', cc', dd',and ee', respectively. In Figures 2.22*a* to 2.22*d*, the reconnection layer is bounded by two straight dashed lines. The term reconnection layer is used here to designate the region consisting of reconnected magnetic field lines only.

Figure 2.22*a* shows the simulation data along line aa' which passes through the equatorward end of the magnetic islands. Corresponding to the active reconnection site at the subsolar point, a northward high-speed plasma jet is seen (the narrow peak of v_θ) at $r \sim 8.5R_E$ where the magnetic field reverses its sign. The peak of v_θ at $r \sim 8.5R_E$ reaches about $\sim 1.5V_{A0}$. Note that on each side of the reconnection layer, or the magnetic field reversal region, $|B| \sim 1.5$ (measured at $r \sim 8.1R_E$ and $8.7R_E$). Hence, the peak value of v_θ is about the local Alfvén speed (based on a constant ρ) immediately upstream of the reconnection layer. The normal flow profile shows that the plasmas converge towards the magnetopause: $v_r > 0$ on the magnetosphere side and $v_r < 0$ on the magnetosheath side. Consistent with the converging flow, the electric

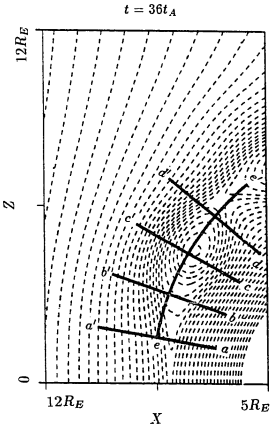

Figure 2.21 Map of the five diagnostic lines (heavy solid lines) aa', bb', cc', dd', and ee' drawn against a background of magnetic field lines (dashed lines) of Case 4 at $t = 36t_A$.

field E_y is positive on both sides. However, the speed of normal flow is much smaller than that of the plasma jet. The local Alfvén Mach number immediately upstream of the reconnection layer is $\sim$ 0.15 on the magnetosheath side and $\sim$ 0.08 on the magnetosphere side (calculated at $r \sim 8.1R_E$ and $8.7R_E$, respectively). Hence, we see that in an island-forming reconnection, plasma can also be accelerated locally to very high speed (in this case to the local upstream Alfvén speed) as predicted theoretically for the steady-state single X-line reconnection.

Figure 2.22*b* shows the simulation data at a higher latitude ($\theta = 20^o$) along line bb'. It can be clearly seen that the current sheet has bifurcated. The two new current layers are now located at $r \sim 8.25R_E$ and $9R_E$. Crossing these two current sheets from outside the reconnection layer, both magnetic field strength $|B|$ and the tangential component B_θ inside the reconnection layer are reduced sharply from the outside values. In addition, the reversal of B_θ occurs at a point between the two current sheets. Therefore, the two MHD discontinuities associated with the two current sheets are likely to correspond to the slow shocks. Also the sudden enhancement of v_θ immediately downstream of the current sheets seems to indicate that plasmas are accelerated by the MHD shocks associated with the two current sheets. Furthermore, the plasma jet in the reconnection layer maintains approximately the same value as at $\theta = 10^o$ (see Figure 2.22*a*) but is wider in the radial direction. The flows outside the reconnection layer are still small and directed toward the reconnection layer. E_y remains positive outside and inside the reconnection layer.

Figure 2.22*c* presents the simulation data along diagnostic line cc' which crosses the magnetic island near its center at $\theta = 30^o$. The magnetic B_θ component reverses its sign gradually through the whole island region and no large discontinuity structures are seen. B_r is small (negative) but nonzero. The $|B|$ profile shows a large pile-up

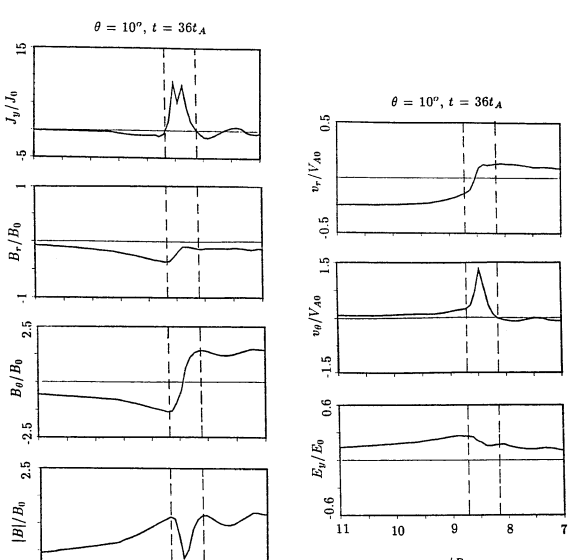

(a)

Figure 2.22 (a) Simulation data along diagnostic line aa' at $\theta = 10^o$ across the magnetic islands formed at $t = 36t_A$ in Case 4. J_y, B_r, B_θ, $|B|$, v_r, v_θ, and E_y are current density, radial component of magnetic field (positive in the anti-earthward direction), azimuthal component of magnetic field (positive in the poleward direction), strength of magnetic field, radial component of velocity, azimuthal component of velocity, and electric field, respectively.

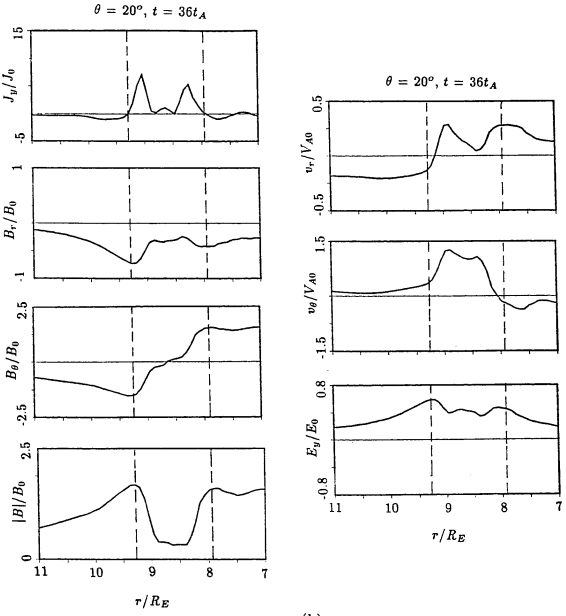

(b)

Figure 2.22 (b) Simulation data along diagnostic line bb' at $\theta = 20°$.

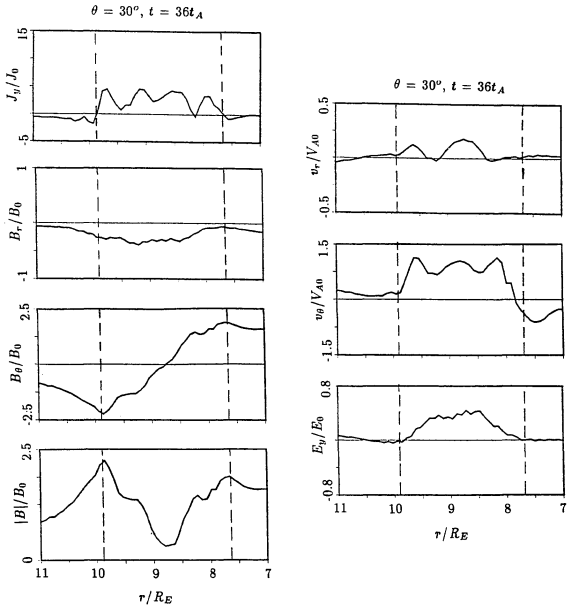

(c)

Figure 2.22 (c) Simulation data along diagnostic line cc' at $\theta = 30^o$.

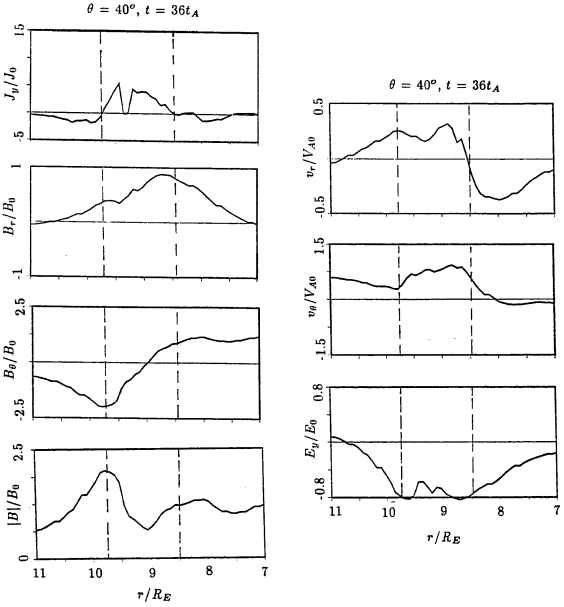

(d)

Figure 2.22 (d) Simulation data along diagnostic line dd' at $\theta = 40°$.

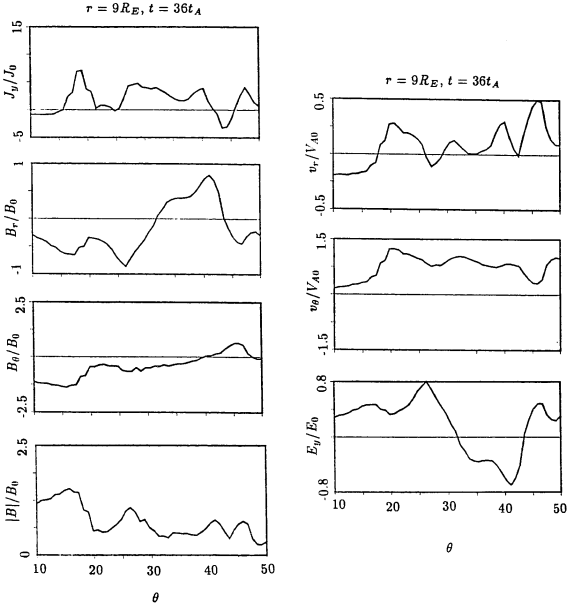

(e)

Figure 2.22 (e) Simulation data along diagnostic line ee' at $r = 9R_E$.

of magnetosheath magnetic fields with a strength comparable to that on the magnetospheric side. The two current layers seen in Figure 2.22*b* can still be identified at $r \sim 9.7R_E$ and $7.9R_E$ but the current density is reduced by ~30%. A region of high current density appears near the island center. Similar to Figure 2.22*b*, v_θ increases sharply downstream of the magnetic island boundary layers (at $r \sim 9.7R_E$ and $7.9R_E$). Also note that the v_θ profile shows a weak three-layer structure within the island region with v_θ peaking at $r \sim 9.5R_E$, $8.7R_E$, and $8.1R_E$. A large reverse (southward) flow is seen just outside the magnetic island on the magnetospheric side (also present in Figure 2.22*b*). A comparison with Figure 2.16 shows that this reverse flow corresponds to the vortex flow centered near the magnetospheric side of the magnetic island. Outside the magnetic island, the induced electric field E_y approaches zero. Inside the magnetic island, E_y remains large and positive.

Diagnostic line dd' crosses the magnetic island at its poleward end. As shown in Figure 2.22*d*, a noticeable feature in the magnetic field is the large positive normal component B_r peaked at $r \sim 8.7R_E$ which is near the magnetospheric side of the magnetic island boundary. Contrary to the convergent flow around the equatorward portion of the magnetic island, the flow pattern outside the magnetic island is now divergent (flowing away from magnetic island) as indicated by the v_r profile (positive on magnetosheath side and negative on magnetospheric side). A look at Figure 2.16 shows that the earthward flow ($v_r < 0$) on the magnetospheric side is also part of the vortex flow discussed above. The electric field E_y now turns to negative with its minimum inside the magnetic island.

Figure 2.22*e* shows simulation data along diagnostic line ee'. The bipolar feature (negative and positive signature) of the magnetic normal component B_r across the magnetic island can be clearly seen. Associated with this bipolar signature of B_r, as noted earlier, is the bipolar structure of E_y which goes from positive to negative

with increasing latitude. Interestingly enough, the point where E_y reverses its sign (at $\theta \sim 32^o$) coincides with the point where B_r reverses sign. In addition, the peak magnitude of E_y in the island region is almost six times larger than that of E_y in the solar wind away from the magnetopause. The v_θ profile along the magnetic island shows an asymmetric feature. The peak of v_θ is located near the equatorward end of the magnetic island at $\theta \sim 20^o$, above which v_θ decreases with increasing latitude. This feature will be discussed extensively in section 4 in association with observations.

Next the distributions of the current-dependent anomalous resistivity along the magnetopause for Case 4 will be shown. The implication of the distributions will be discussed in relation to the reconnection patterns. Shown in Figure 2.23 is the distribution of $\eta(J)$ (see equation (2.5)) at different times near the magnetopause in the x-z plane. At $t = 26t_A$, the magnetopause current density exceeds slightly the critical current intensity ($J_c = 10$) in the region from $\theta = 0^o$ to $\sim 40^o$. As a consequence, a narrow strip of higher resistivity appears along the magnetopause up to $\theta \sim 40^o$. In the rest of the region, the resistivity distribution is constant ($= \eta_b$). At this time, no reconnection has been observed yet (cf. Figure 2.15). At $t = 29t_A$, the resistivity is enhanced largely at two points ($\theta = 0^o$ and $\sim 10^o$) in the magnetopause. A careful comparison with Figure 2.15 shows that these two points are the location of the two X lines (northern hemisphere). At a higher latitude ($\sim 30^o$) in the magnetopause, there is another enhanced resistivity region but the magnitude of the enhanced resistivity in this region is smaller than that at the two lower latitude points. Figure 2.15 shows that in this higher latitude region of enhanced resistivity, a third X line is about to be formed. At $t = 31t_A$, it is seen in Figure 2.15 that in the northern hemisphere, two magnetic islands are formed due to magnetic reconnections at three X lines, which are located at $\theta \sim 0^o$, 20^o, and 40^o, coinciding with the three regions having a large resistivity

enhancement in Figure 2.23. At $t = 36t_A$, the resistivity enhancement, though reduced by 50%, remains at the subsolar point but has disappeared elsewhere.

It is seen that the appearance of a new reconnection site is always associated with a local enhancement of resistivity. The resistivity enhancement is further caused by the local enhancement of current intensity. However, what leads to the enhancement of the current density in the first place, remains unclear. It is possible that the unstable tearing modes may be responsible for the enhancement of current density too. In any case, for reconnections induced by current-dependent resistivity, the process seems a mutually interactive one. First, the initial small fluctuation of current density and, consequently, the small local enhancements of resistivity at several points will trigger magnetic reconnections at these points. The onset of magnetic reconnections will further enhance the current density and, in effect, the resistivity at X lines. The enhancement of resistivity will, in turn, speed up the reconnection process. Hence, this mutually inducing process will lead quickly to the impulsive reconnections as evidenced by Figure 2.24, which shows the variation of the electric field E_{sp} at the subsolar point with time. As pointed out in subsection 2.3.1, E_{sp} corresponds to the reconnection rate at the subsolar point. In Figure 2.24, it is seen that E_{sp} increases quickly after $t \sim 29t_A$ and reaches a maximum at $t \sim 31t_A$. After reaching the maximum, E_{sp} again drops sharply. The variation of E_{sp} indicates a typical impulsive reconnection process at the subsolar point for Case 4.

It should be noted that the magnetic reconnection pattern in Case 4 is, of course, not the only type for the dayside magnetopause. Case 4 serves mainly to demonstrate one possible family of dayside reconnections: the small-scale impulsive reconnections with multiple reconnection sites. A phenomenological model describing the similar reconnection process at the dayside magnetopause has been suggested by *Lee and Fu* [1985]. The term multiple X-line reconnection originates from their initial paper and is

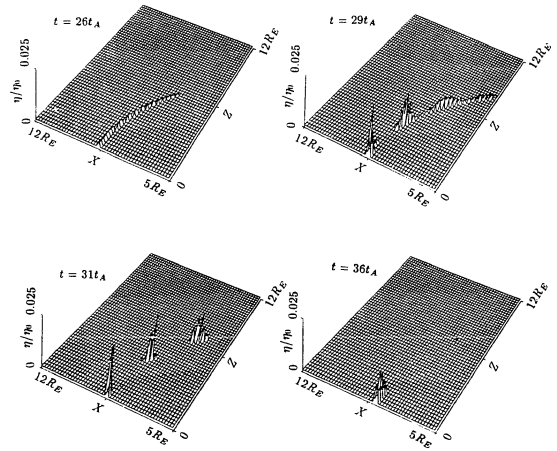

Figure 2.23 Distribution of anomalous resistivity η near the dayside magnetopause at four different times in Case 4. η_0 is the normalization unit for resistivity.

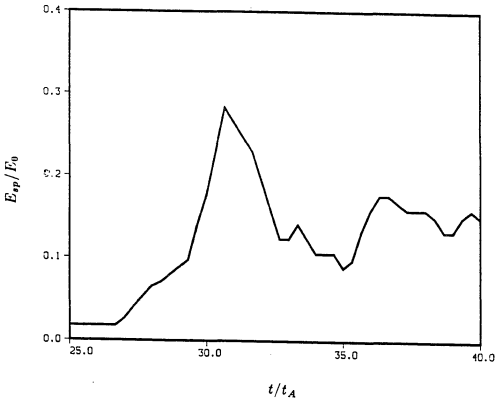

Figure 2.24 Variation of magnetic reconnection rate at the subsolar point as a function of time in Case 4. E_{sp} is the electric field at the subsolar point and is defined as the reconnection rate at that point.

used by these authors to refer to the type of magnetic reconnections in which magnetic islands are formed. In addition, they have used their dayside multiple X-line reconnection model to interpret successfully the observed flux transfer events (FTEs). In section 2.4, the magnetic and plasma signatures produced by the reconnection processes in Case 4 will be examined and compared with those of FTEs.

2.3.3 Effect of solar wind Alfvén Mach number

The effect of the solar wind Alfvén number on the dayside reconnections has been studied by *Podgorny et al.* [1978] in laboratory experiments. In their experiments, an artificial magnetosphere was produced as a result of interaction between a super-Alfvénic flow of collisionless plasma and the magnetic field of a dipole. In the presence of a southward magnetic field component in the plasma, Dungey-type steady magnetic reconnection prevails for Alfvén Mach numbers just above unity ($\sim$ 1.5). However, when the Alfvén Mach number increases to $\sim$ 10, a large magnetic bubble (a magnetic island) is observed in front of the dayside magnetopause as a result of two X-type neutral points formed near the polar cleft. Due to the limited resolution of the experiments, the small-scale structures inside this large magnetic bubble were unknown.

In the present simulation, the solar wind Alfvén Mach number M_{sw} is another parameter that can be changed. By definition, $M_{sw} = B_{sw}/v_{sw}$ (in normalized units). A change in M_{sw} can be caused by a change in either B_{sw} or v_{sw}. In the cases presented below, v_{sw} is fixed while B_{sw} changes. Recall that our initial configuration is an equilibrium between the incompressible flow (the solar wind flow) and a dipole field (the geomagnetic field). To change v_{sw} would also require a change in the dipole field strength to maintain the equilibrium. Hence, in the normalized units v_{sw} will not be changed.

We now present two simulation cases, Case 5 and Case 6, to demonstrate the effect of M_{sw}. In Case 4 the Alfvén Mach number is low ($M_{sw} = 2$). In Case 5, M_{sw} is increased to 4 and in Case 6, M_{sw}=6. All the other parameters in Case 5 and Case 6 are the same as in Case 4 (see also Table 2.1).

In Case 5, the solar wind Alfvén Mach number is $M_{sw} = 4$. Figure 2.25*a* shows the magnetic field patterns at $t = 34t_A$ and $t = 39t_A$ and Figure 2.25*b* shows the corresponding flow patterns. At $t = 34t_A$, one long and thin magnetic island is formed in each hemisphere. Within each of these long magnetic islands two smaller islands begin to appear. The formation of the long magnetic islands is caused by magnetic reconnections at the subsolar point and at two high latitude locations (on the magnetopause near $x = 5R_E$). At $t = 39t_A$, the long magnetic island has split into two magnetic islands, which have grown to large sizes and are being convected poleward. We now compare the reconnection patterns of Case 4 and Case 5 at the early stage of reconnections. In the comparison, we choose the $t = 29t_A$ instance for Case 4 and $t = 34t_A$ for Case 5 (note that reconnections start at a later time in Case 5 than in Case 4). In both cases, one reconnection site is at the subsolar point. However, in Case 5 the second reconnection site has shifted to high latitude (near $\theta \sim 60^o$) while in Case 4 the second reconnection site is at $\theta \sim \pm 10^o$. Therefore, it is seen that reconnection sites tend to move to higher latitude when M_{sw} is increased. Later on, the magnetic field pattern at $t = 39t_A$ in Case 5 looks similar to that of Case 4 at $t = 36t_A$ (see Figure 2.15). However, two apparent differences can be identified. First, in Case 5 the bulge of magnetic islands (at $t = 39t_A$) on the magnetosheath side is larger than that on the magnetospheric side, while in Case 4 the bulge of magnetic islands (at $t = 36t_A$) is almost symmetric on both sides. The asymmetry of the magnetic island bulge in Case 5 is expected to be due to the large difference in magnetic field strength on the two sides of the magnetic island. Second, the open flux layer enveloping the magnetic

island in Case 4 is absent in Case 5 ($t = 39t_A$). At $t = 39t_A$, the reconnected field lines in Case 5 are all the closed field lines of magnetic islands. This indicates that in Case 5, the same amount of magnetic flux is reconnected at both ends of the magnetic island while in Case 4 more magnetic flux is reconnected at the low-latitude end of each magnetic island, forming open magnetic field lines enveloping the magnetic island from below. This implies that when M_{sw} increases, the reconnection rate at higher latitudes tends to increase.

In Case 6, the solar wind Alfvén Mach number is further increased to $M_{sw} = 6$. Figures 2.26*a* and 2.26*b* show the dayside reconnection patterns of magnetic field and plasma flow, respectively, at three different times. It is seen that the high-latitude reconnection becomes dominant. At $t = 38t_A$, no reconnection occurs near the subsolar point (low-latitude region). Instead, a long magnetic island centered at the subsolar point is formed as a result of reconnections at two high-latitude points in the northern and southern hemispheres. The magnetic island grows with time and later two magnetic islands are formed inside the large island due to reconnection at the subsolar point. However, the reconnection process at the subsolar point is much weaker than that at the two high-latitude ends of the large island. In fact, in Figure 2.26*b*, significant equatorward flows are seen inside the large island near its two high-latitude ends. These equatorward flows are caused by plasma accelerations associated with the high-latitude reconnection. In the whole process, the large island is stagnant at the dayside magnetopause, while the interplanetary magnetic fields keep piling up in front of this magnetic island. In addition, as in Case 5, the magnetic bulge caused by the large island is larger on the magnetosheath side than on the magnetospheric side. This geometrical asymmetry in the bulge seems to be a common feature when the magnetic field strength has a large asymmetry on the two sides of the magnetic island. The large magnetic island formed in Case 6 is very similar to that observed in *Podgorny et al.*'s

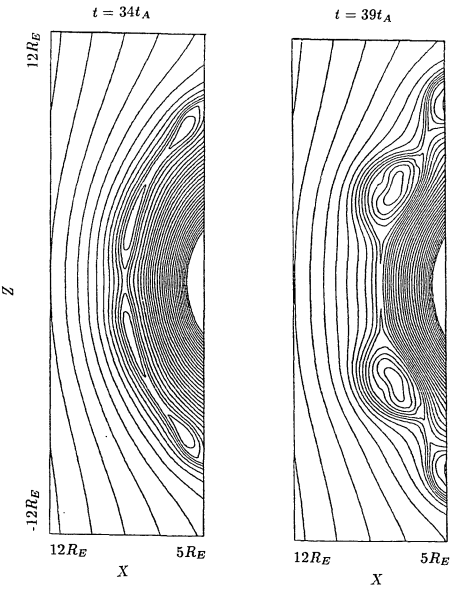

Figure 2.25 (a) Magnetic field configurations near the dayside magnetopause at $t = 34t_A$ and $t = 39t_A$ in Case 5.

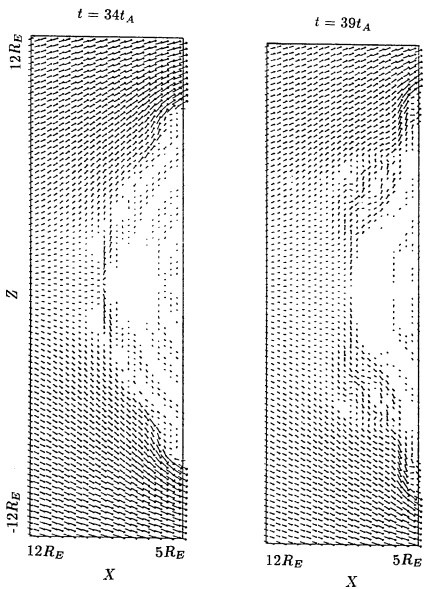

(b)

Figure 2.25 (b) Plasma flow patterns near the dayside magnetopause at $t = 34t_A$ and $t = 39t_A$ in Case 5.

[1978] experiment for a high Alfvén Mach number ($\sim$ 10) and in the particle simulation by *Allen and Swift* [1989].

The simulations presented above suggest that when the solar wind Alfvén Mach number increases, the dayside reconnections tend to shift to higher latitude. For a very large M_{sw}, the high-latitude reconnection may become the dominant dayside reconnection process. Similar latitudinal dependence of the dayside reconnection process on the solar wind Alfvén Mach number is observed by *Podgorny et al.* [1978]. Note that though the simulation presented here is only a two-dimensional one, the experiment conducted by Podgorny et al. is in a more realistic 3-D geometry. In *Lee and Fu*'s [1986*a*] locally driven reconnection, a large magnetic island would later split at the stagnation point of plasma flow and the daughter islands would be subsequently expelled poleward. Hence, the large island in Case 6 is also expected to be split and expelled poleward later.

If the large magnetic island can indeed be formed at the dayside magnetopause as in Case 6, the chances of observing it are high due to its large size, which is expected to be $\sim$ 5–10R_E in the north-south direction and $\sim$ 1–2R_E in the radial direction. However, since one satellite can usually sample data in a very limited region, simultaneous observations by many satellites at spatially separated regions are needed to obtain a global picture of the large island. One feature that may be used for the identification of the large island at the dayside magnetopause in satellite observations is the equatorward plasma flow at high latitude and the associated large normal magnetic component (positive in the northern hemisphere and negative in the southern hemisphere).

Finally, the 3-D configuration of the large magnetic island in Case 6, which results from high-latitude reconnection, is worth further study.

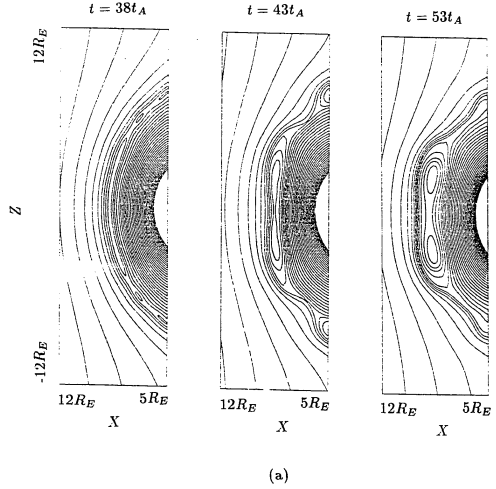

Figure 2.26 (a) Magnetic field configurations near the dayside magnetopause at $t = 38t_A$, $t = 43t_A$, and $t = 53t_A$ in Case 6 .

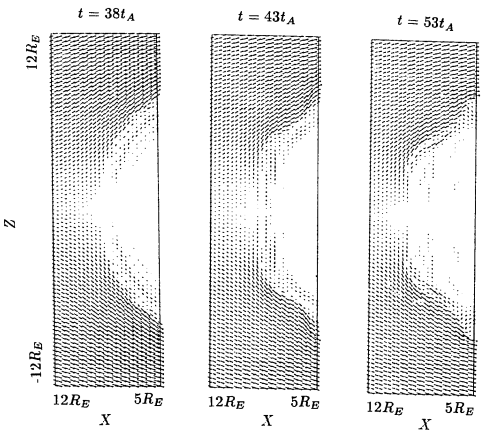

(b)

Figure 2.26 (b) Plasma flow patterns near the dayside magnetopause at $t = 38t_A$, $t = 43t_A$, and $t = 53t_A$ in Case 6.

2.4. Flux Transfer Events and Impulsive Reconnections at the Dayside Magnetopause

2.4.1 Flux transfer events

Based on the ISEE spacecraft magnetic field data, *Russell and Elphic* [1978] reported impulsive magnetic events near the dayside magnetopause. These events are characterized by a bipolar signature in the magnetic field component normal to the dayside magnetopause. The events were termed flux transfer events (FTEs), which they interpreted as being due to the passage of open magnetic flux tubes formed by patchy or localized reconnections. The properties of FTEs were later further studied and discussed by a number of authors [*Paschmann et al.*, 1982; *Scholer et al.*, 1982; *Daly et al.*, 1981, 1984; *Cowley*, 1982; *Rijnbeek et al.*, 1984; *Saunders et al.*, 1984; *Berchem and Russell*, 1984]. Figure 2.27 shows an example of FTEs as they appear in observational data obtained by ISEE 1 and 2 [*Saunders et al.*, 1984]. In Figure 2.27, plasma density, velocity, and the magnetic field observed in the vicinity of the magnetopause (magnetosheath side) are displayed as a function of time. $\tilde{N}_e$ and $\tilde{N}_p$ are the number densities of energetic electrons and protons, respectively. B_N is the magnetic field component normal to the magnetopause and B_L and B_M are two other components in a boundary normal coordinate system discussed earlier. Three FTEs are identified at times of $\sim$ 1319 UT, 1325 UT, and 1342 UT. Each event is bounded by two vertical dashed lines in Figure 2.27. In each event, B_N shows an bipolar variation with an positive-negative excursion. FTEs with a negative-positive B_N excursion are also observed. In terms of *Rijnbeek et al.*'s [1984] classification, the former type of FTEs is defined as "standard" FTEs, while the later type are the "reverse" FTEs. FTEs are found all over the dayside

magnetopause region covered by the ISEE spacecraft on both the magnetosheath and magnetospheric sides.

Statistical studies of satellite data have revealed some of the general features of FTEs. It has been found that the majority of FTEs occur when the magnetic field in the magnetosheath has a southward component. The close correlation of the occurrence of FTEs with the IMF orientation provides strong evidence that FTEs are closely associated with magnetic reconnection on the dayside magnetopause. The properties of FTEs observed in the magnetosheath and in the magnetosphere are similar, suggesting a common source for the FTE generation. Observations indicate that FTEs are separated temporally by 5–15 minutes with each event lasting about 1–2 minutes. The cross-section of the flux tube is typically 1 R_E^2, elongated in the north-south direction. FTEs with a positive-negative B_N signature ("standard" FTEs) are preferentially observed in the northern hemisphere, while FTEs with a negative-positive B_N excursion ("reverse" FTEs) occur most frequently in the southern hemisphere. This spatial distribution of B_N signatures suggests that FTEs originate at low-latitude region rather than in the cusp regions. Apart from the magnetic field signatures, FTEs are also characterized by a mixture of magnetosheath and magnetospheric particles. These facts strongly support the hypothesis that FTEs represent encounters of reconnected flux tubes [*Paschmann et al.*, 1982]. Enhanced plasma flow speeds ($\sim$ 100 km/s) are often seen in crossings of FTEs near the magnetopause [*Paschmann et al.*, 1982]. These observations further show that the enhanced plasma flow speeds are near the trailing end of an FTE. This asymmetry in the enhanced plasma flow speed distribution may be an indication of ongoing magnetic reconnections at the equatorward portion of the FTE bulge [*Paschmann et al.*, 1982; *Sonnerup*, manuscript,1988].

Since their discovery, FTEs have attracted a large amount of attention from magnetospheric physicists and have come to play an important role in the study of solar

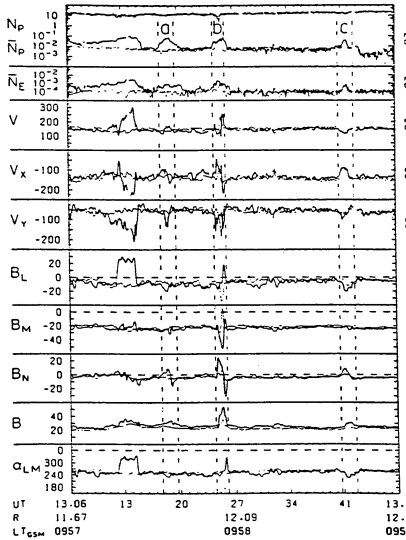

Figure 2.27 ISEE-1 (heavy trace) and ISEE-2 (light trace) magnetic field and plasma measurements from the outbound magnetosheath passage on October 23, 1978. The plasma data are shown in the top five panels, and consist of various density and flow parameters. The magnetic field recordings are displayed in boundary normal coordinates where B_N is outward along the boundary normal, B_L is along the projection of the GSM Z-axis in the magnetopause plane, and B_M completes the orthogonal triad and points westward. The bottom panel shows the field angle in the LM plane, defined by $\alpha_{LM} = tan^{-1}(B_M/B_L)$. ISEE-1's position is given at the base of the fig. in terms of geocentric radial distance (R) in Earth radii, and GSM local time (LT_{GSM}) and latitude (LAT_{GSM}) (Saunders et al., 1984).

wind-magnetosphere interactions. There is a large body of experimental evidence which is suggestive of FTE's close associations with magnetic reconnections. It is therefore not surprising that almost all the theoretical FTE models have invoked magnetic reconnections. For this reason, FTEs have contributed largely to the recent conceptual changes in our dayside reconnection pictures (for a review of various reconnection models motivated by FTEs, see Chapter 1 and the references therein). At the same time, interpretations of FTEs have become in a way a process of testing and developing new dayside reconnection models. Although the detailed magnetic reconnection geometry is not known, it is now widely accepted that FTEs represent either moving magnetic tubes as in Russell-Elphic model [*Russell and Elphic*, 1978] and Lee-Fu model [*Lee and Fu*, 1985] or the bulged open flux loops as in Scholer's [1988*a*] and Southwood et al.'s [1988] model.

In subsection 2.4.2 and 2.4.3, we will use our simulation results to illustrate two types of dayside reconnection, which can produce major FTE signatures.

2.4.2 Multiple X line reconnections

Lee and Fu [1985] proposed an FTE model, in which FTEs are considered as passages of magnetic islands (or magnetic flux tubes in 3-D configuration) resulting from multiple X-line reconnections at the dayside magnetopause (see Chapter 1 for a review). The magnetic reconnection pattern in Case 4 (described in section 2.3.2) resembles in many ways the theoretical picture of Lee-Fu's dayside multiple X-line reconnections. In the following, the magnetic field and plasma flow signatures produced by the multiple X-line reconnections in Case 4 will be compared with those of FTEs. The comparison shows that some of the magnetic and plasma signatures resulting from reconnection patterns in Case 4 are in good agreement with the observed features of FTEs.

Observations show that in the northern hemisphere the bipolar B_N signature is often seen to have a positive-negative excursion while in the southern hemisphere a negative-positive B_N excursion is observed. This feature of FTEs can be explained by the reconnection processes described previously in Case 4. In Figures 2.14 and 2.15, it was seen that magnetic islands formed in the low-latitude region are later convected poleward. Hence, a fixed observer (say, in a satellite) close enough to the magnetopause would see a bipolar impulse of B_N at each pass of a magnetic island. Since the magnetic fields on the magnetosheath side are pointing southward and on the magnetospheric side northward, the bipolar B_N impulse will show a positive-negative (negative-positive) excursion in the northern hemisphere (in the southern hemisphere). Furthermore, one of the observational facts is that FTEs are observed more frequently at high latitudes while their origin seems to be in the low-latitude region [*Russell et al.*, 1985; *Southwood et al.*, 1986]. The present simulation is also consistent with this property of FTEs. As Case 4 shows, the magnetic islands are formed at low latitudes initially and are later convected to high-latitude region. In the process of poleward convection, the island size also grows. Hence, a larger size of magnetic islands and a stronger B_N component at higher latitude make them easier to detect.

As mentioned in subsection 2.4.1, one important feature that strongly suggests ongoing magnetic reconnections at the equatorward portion of magnetic flux tubes is the plasma flow speed enhancement at the trailing end of FTEs. In Figure 2.16, which shows the flow pattern of Case 4, an enhanced-flow region is associated with each moving magnetic island (this is particularly clear at $t = 36t_A$). This indicates that magnetic islands are moving faster than the ambient plasmas. The latitudinal distribution of the tangential velocity v_θ at $t = 36t_A$ for the lower magnetic island in the northern hemisphere is shown in Figure 2.22*e*. The peak of v_θ is near the trailing end of the magnetic island. The magnitude of v_θ near the trailing end of the magnetic island is

approximately equal to the local Alfvén speed just upstream of the reconnection layer (see Figure 2.22*a* and the discussions therein). The value of v_θ in the trailing end is expected, since magnetic reconnection at the equatorward end of the island (in this case, the subsolar point) is still in progress with a nonzero reconnection rate as shown in Figure 2.24.

The trailing end plasma flow speed enhancement observed in FTEs [*Paschmann et al.*, 1982] can be explained in terms of the multiple X-line reconnection process. Suppose that magnetic reconnection at the equatorward end of the magnetic islands occurs during the poleward convection of the magnetic island and dominates over the reconnection at the poleward end of the same magnetic island. Plasma near the equatorward portion of the magnetic island will be accelerated to a speed faster than the ambient plasma. At the same time, a magnetic island moving away from the equatorial region at a speed faster than the ambient plasma must push its way through the ambient plasma at the poleward end of the magnetic island. Consequently, plasma flow speed is reduced at the poleward end of the magnetic island. Case 4 of the simulation supports such an argument at least qualitatively. Hence, in addition to the bipolar B_N signature, the Lee-Fu type of multiple X-line reconnection seems to be also capable of generating the observed asymmetric enhanced plasma flow patterns associated with FTEs.

To this point, the comparison of the present simulation with FTEs has only been made at a fixed time. Observationally, FTEs are identified in the magnetic and plasma data recorded by satellites as a function of time (cf. Figure 2.27). In order to provide a more accurate and realistic comparison, several probes have been placed at fixed locations near the magnetopause for Case 4. These probes will record magnetic field and plasma velocity as a function of simulation time. The probes are placed in three different regions: magnetosheath, magnetopause, and magnetosphere. In the following, the variation of the magnetic field and plasma velocity with time as seen by nine probes

will be presented in Figures 2.28*a*–*i*. In each figure, the region of the FTE-like event is marked by two vertical dashed lines. As in Figures 2.22*a* to *e*, the magnetic field and velocity are decomposed into normal components, B_r and v_r, and tangential components, B_θ and v_θ. The nine probes are all in the northern hemisphere and are located at $r = 8R_E$, $8.7R_E$, and $9.4R_E$, and $\theta = 10^o$, 23^o, and 36^o, respectively (cf. Figure 2.21 for the approximate locations of probes). For the convenience of discussions, the two hemisphere magnetic islands in the northern hemisphere in Case 4 (see Figures 2.15 and 2.16) will be named island 1 (the lower one) and island 2 (the upper one).

Magnetosheath events

Figures 2.28*a* to 2.28*c* below show the magnetic and plasma data recorded by three probes at $r = 9.4R_E$ and $\theta = 10^o$, 23^o and 36^o, respectively. In these figures, B_θ is negative throughout the diagnostic time and, therefore, the FTE-like events are observed in the magnetosheath.

In Figure 2.28*a*, a negative B_r pulse is seen around $t \sim 30t_A$. Both v_r and v_θ are small during the event. The small plasma velocity indicates that the probe is outside the magnetic island region all the time. The negative B_r pulse means that the probe sees only the magnetic disturbance caused by the lower portion of island 1. The compression of the magnetosheath field by the passing island is evidenced by an increase in $|B_\theta|$. The v_r becomes negative at $t \sim 30t_A$, which indicates a earthward flow towards magnetopause during and after the passage of island 1.

At latitude $\theta = 23^o$ as shown in Figure 2.28*b*, the bipolar positive-negative FTE signature of B_r is seen during the interval from $t \sim 31t_A$ to $\sim 39t_A$. A small enhancement in v_θ is seen near the trailing end of this FTE-like event.

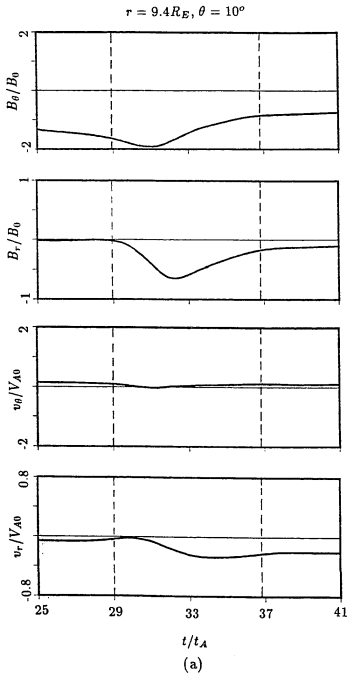

Figure 2.28 Magnetic and plasma flow measurements at fixed probes. (a) Magnetic field and plasma flow measured by probe 1 placed at $r = 9.4R_E$ and $\theta = 10°$.

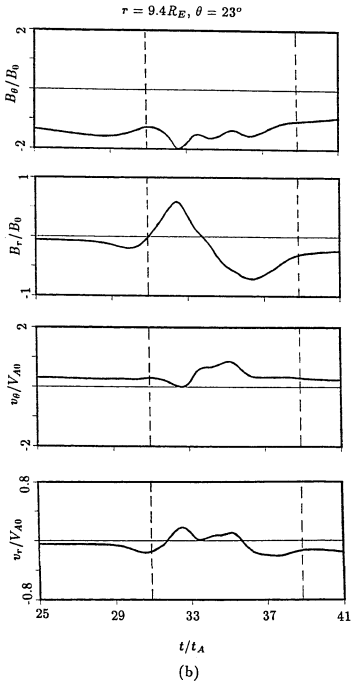

Figure 2.28 (b) Magnetic field and plasma flow measured by probe 2 placed at $r = 9.4R_E$ and $\theta = 23°$.

At high latitude $\theta = 36^o$ (Figure 2.28c), a positive-negative bipolar B_r pulse appears from $t \sim 34t_A$ to $t \sim 39t_A$. At the trailing end of the B_r bipolar pulse, there is a large enhancement in v_θ. The positive-negative B_r pulse together with this large v_θ enhancement implies that the probe sees the passing of island 1 near its center region. Note that B_θ is negative and is almost zero near the end of the event. Hence the trailing portion of the FTE-like pulse is very close to the magnetopause. The present result is consistent with satellite observations [*Paschmann et al.*, 1982] that enhanced plasma flow speed regions are usually seen in FTEs in or very close to the magnetopause. The negative B_r pulse immediately ahead of the positive-negative B_r pulse in Figure 28c corresponds to the passing of the trailing end of island 2. Associated with this negative B_r pulse is a small v_θ enhancement peaking at $t \sim 32t_A$.

Magnetopause events

Figures 2.28*d* to 2.28*f* show the magnetic and plasma data recorded by three probes at $r = 8.7R_E$ and $\theta = 10^o$, 23^o and 36^o, respectively. These FTE-like events are classified as magnetopause events, since B_θ changes its sign.

At $\theta = 10^o$, B_r only shows a negative pulse from $t \sim 29t_A$ to $t \sim 37t_A$. A small v_θ enhancement is seen, peaking at the trailing end of the B_r pulse; v_r remains small during the event. The v_θ enhancement and negative B_r pulse indicate that the probe is inside island 1 and sees the passing of the trailing end. Since the probe is near the subsolar point, the velocity enhancement associated with magnetic reconnection at the subsolar point is not very high.

At $\theta = 23^o$, the probe detects a very clear FTE-like positive-negative B_r pulse from $t \sim 32t_A$ to $t \sim 38t_A$ and a large v_θ enhancement peaking at the the trailing end of the B_r pulse. This corresponds to the passage through the core region of island 1.

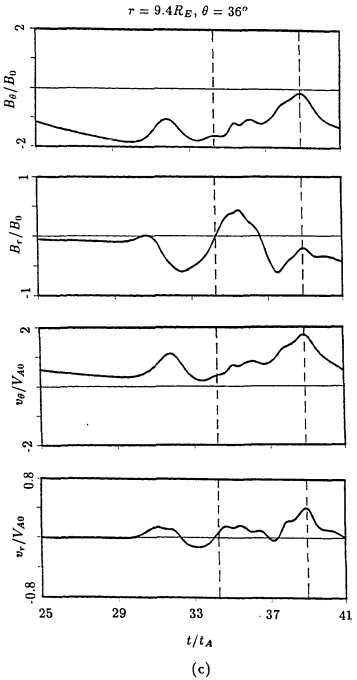

Figure 2.28 (c) Magnetic field and plasma flow measured by probe 3 placed at $r = 9.4R_E$ and $\theta = 36°$.

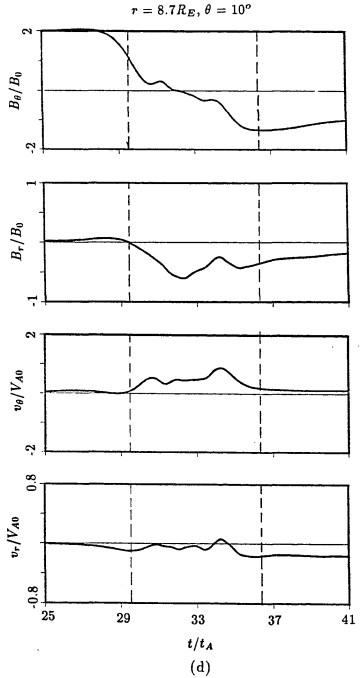

(d)

Figure 2.28 (d) Magnetic field and plasma flow measured by probe 4 placed at $r = 8.7R_E$ and $\theta = 10^o$.

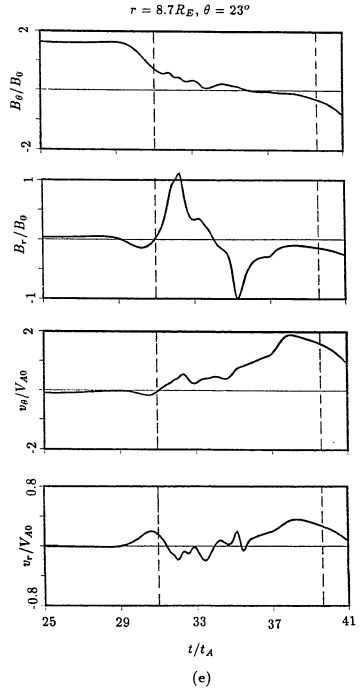

(e)

Figure 2.28 (e) Magnetic field and plasma flow measured by probe 5 placed at $r = 8.7R_E$ and $\theta = 23^o$.

At a higher latitude $\theta = 36^o$, the probe begins to see the passage of island 2 before island 1. As shown in Figure 2.28*f*, two FTE-like positive and negative B_r pulses are seen together with a v_θ enhancement. The first positive-negative B_r pulse corresponds to the passage of island 2 and the second pulse is associated with island 1. The v_θ enhancement associated with island 2 is centered in the trailing end of the pulse, while the v_θ enhancement associated with island 1 peaks at the trailing end.

Magnetosphere events

Figures 2.28*g* to 2.28*i* present the magnetic and plasma data recorded by three probes placed at $r = 8R_E$ and $\theta = 10^o$, 23^o and 36^o, respectively. In these figures, B_θ is positive and the three FTE-like events can be considered as magnetospheric events.

At low latitude $\theta = 10^o$ (Figure 2.28*g*), the probe sees only a negative B_r pulse while the plasma velocity is close to zero. Therefore, the B_r pulse is caused by the passing of the equatorward portion of island 1. A large B_θ during the event indicates that the probe is away from the magnetopause.

At $\theta = 23^o$ (Figure 2.28*h*), a bipolar FTE-like B_r pulse can be clearly identified. This FTE-like B_r pulse can be identified as caused by the compression of the geomagnetic fields by the passing of island 1. The increase of B_θ is also due to the compression of the geomagnetic fields. The negative-positive v_r variation shows that the plasma poleward of the island is expelled away from the the island and the plasma in the trailing end converge towards the island.

At $\theta = 36^o$ (Figure 2.28*i*), immediately following a small negative B_r pulse from $t \sim 31t_A$ to $t \sim 34t_A$, a complete positive-negative bipolar pulse occurs. The negative B_r pulse preceding the bipolar B_r pulse is due to the compression of the geomagnetic field by the passing of the equatorward portion of island 2. The later bipolar pulse

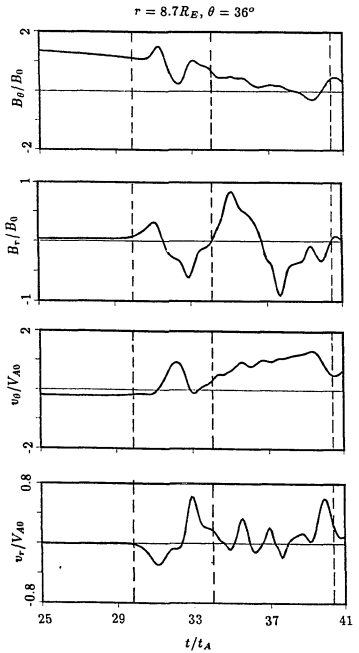

Figure 2.28 (f) Magnetic field and plasma flow measured by probe 6 placed at $r = 8.7R_E$ and $\theta = 36^o$.

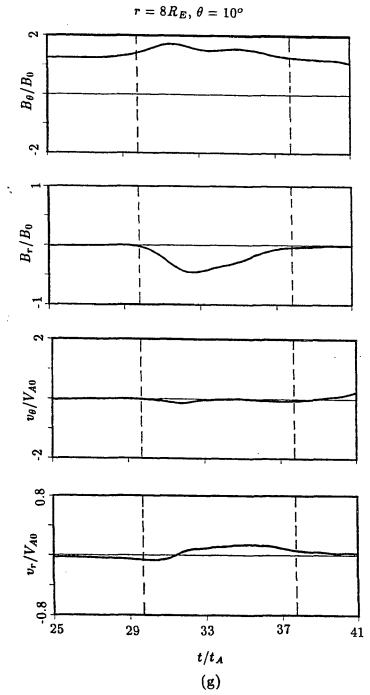

Figure 2.28 (g) Magnetic field and plasma flow measured by probe 7 placed at $r = 8R_E$ and $\theta = 10°$.

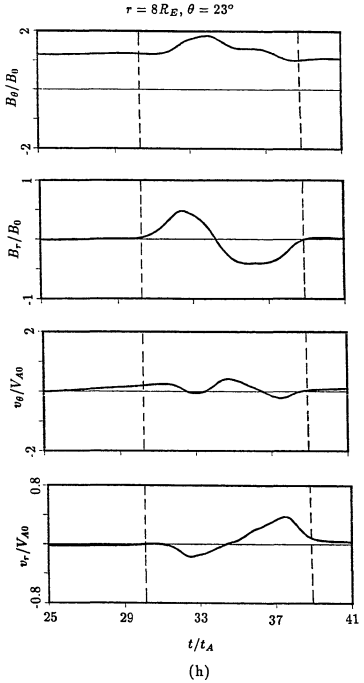

Figure 2.28 (h) Magnetic field and plasma flow measured by probe 8 placed at $r = 8R_E$ and $\theta = 23°$.

corresponds to the passing of island 1 near its core on the magnetospheric side as is implied by the largely enhanced v_θ and the decrease in B_θ. In addition, a large positive v_r pulse near the end of the bipolar pulse shows a large plasma flow towards the magnetopause after the passage of island 1.

Some of the magnetic and plasma properties revealed in Figures 2.28*a* to 2.28*i* are summarized and discussed in the following.

(1) The simulation suggests that the poleward convection of magnetic islands formed by the dayside multiple X-line reconnections can indeed generate FTE-like bipolar B_N signatures in the magnetosheath, magnetopause, and magnetosphere. The observation of a bipolar B_N pulse does not necessarily correspond to the passage of the magnetic island itself through the observation point. In the magnetosheath and magnetosphere, a bipolar B_N may be caused by the passage of rippled magnetic structure due to the compression of the magnetosheath or magnetospheric field by the moving magnetic island. The bipolar B_N pulse in this category can be identified by the absence of enhanced plasma flow speed.

(2) In the simulation, the tangential plasma velocity enhancement is sometimes found to be associated with the bipolar B_N pulse. The enhanced tangential plasma flow velocity either is concentrated or appears as peaks in the trailing end of the bipolar pulse. This asymmetry in flow speed enhancement found in our simulation is in good agreement with observations. Observations [e.g., *Paschmann et al.*, 1982] further show that FTEs with enhanced plasma flow speed are preferentially those seen near the magnetopause. This is also consistent with the multiple X-line reconnection picture of FTEs since, as the above simulation shows, the enhanced plasma flow speed appears only within the magnetic island region. Also as shown above, an enhanced v_θ usually corresponds to a small or zero B_θ, while the magnetopause position is roughly identified as where B_θ is zero.

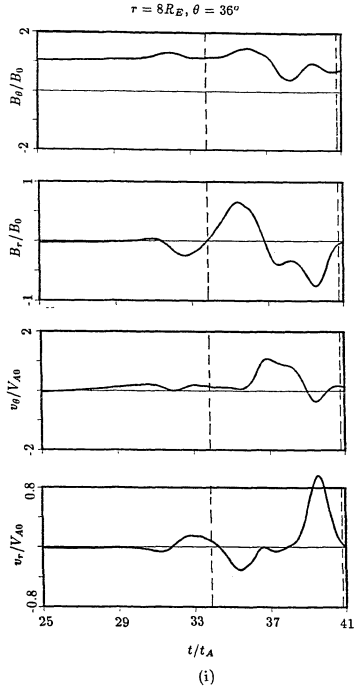

Figure 2.28 (i) Magnetic field and plasma flow measured by probe 9 placed at $r = 8R_E$ and $\theta = 36^o$.

(3) In Case 4, the duration of the bipolar B_r structure ranges from 6–8t_A (3–4 minutes), close to the observed duration of an FTEs.

(4) At low latitude regions ($\theta < 10^o$ in Case 4), the complete B_N pulse may not be seen. Instead, a positive or negative B_N pulse may appear, corresponding to the passage of the equatorward portion of an magnetic island. *Rijnbeek et al.* [1984] have included the single B_N pulse events as "irregular" FTEs.

2.4.3 Bursty single X-line reconnection

In subsection 2.3, based on the simulation cases with constant resistivity, it was suggested that in the presence of small resistivity or a large magnetic Reynolds number, dayside reconnection may occur preferentially in the form of multiple X-line reconnections. However, a particular type of single X-line reconnection may still be possible even in the presence of a locally enhanced resistivity. This is the bursty single X-line reconnection process proposed independently by *Southwood et al.* [1988] and *Scholer* [1988*a*] in an attempt to explain FTEs. These authors argued that a sudden enhancement and a subsequent reduction of the reconnection rate at a local point on the magnetopause can generate a bulged magnetic field region, which produces the bipolar normal magnetic field component signature of FTEs. This model is usually referred to as the bursty reconnection model, in which magnetic reconnection occurs only at one point (i.e., single X line reconnection). In order to generate a large enough magnetic bulge, in addition to the sudden enhancement and reduction of the reconnection rate, one prerequisite condition is the existence of a long current sheet, which is typical of the dayside magnetopause. Therefore, if the occurrence of local impulsive change of the reconnection rate can be justified at the dayside magnetopause, this model may be another potential candidate for FTEs. One possibility is that, as suggested by *Southwood* [1987], the

reflection of current surges between the dayside region and ionosphere modulates the reconnection rate at the subsolar point. A similar bursty single X line reconnection process and the resulting magnetic field bulge structure were predicted and studied analytically earlier by *Biernat et al.* [1987].

Below is persented a simulation ,Case 7, which reproduces the single X-line bursty reconnection at the dayside magnetopause. In Case 7, the magnetic reconnection is triggered at the subsolar point by a sudden local resistivity change. To simulate this case, the resistivity form assumed in equation (2.5) is replaced by

$$\eta = \eta_l e^{-[(x-x_0)^2+(z-z_0)^2]/l_0^2} e^{-(t-t_0)^2/\tau^2} + \eta_b. \tag{2.13}$$

The first term on the right-hand side represents a local impulsive resistivity while the second term is the usual background resistivity. It is seen in (2.13) that resistivity will be enhanced around a local area centered at $x = x_0$ and $z = z_0$ near $t = t_0$ for a period of τ. A small $\eta_b = 0.00025$ is used such that a long current sheet can be formed at the dayside magnetopause before reconnection. The resistivity onset time is chosen as $t_0 = 26t_A$ when the long current sheet, as shown in the simulation, has formed at the magnetopause. Since we intend to trigger magnetic reconnection at the subsolar point, which at time $t = 26t_A$ is found to be at $x = 9R_E$, we set $x_0 = 9R_E$, $z_0 = 0$, and $l_0 = 2R_E$. Finally, we set $\tau = 2t_A \sim 1$ minute, which is of the order of the duration of one FTE, and $\eta_l = 0.06$.

With the small η_b and the local impulsive resistivity component in (2.13), bursty reconnection is observed, as is expected, in Case 7 at the subsolar point. A large magnetic bulge is formed and later convected poleward. Figure 2.29*a* shows two snapshots of the magnetic field configurations in Case 7 near the magnetopause at $t = 30t_A$ and $t = 36t_A$ and Figure 2.29*b* gives the the corresponding plasma flow patterns. At $t = 30t_A$, as shown in Figure 2.29*a*, the sudden enhancement of the resistivity at the

subsolar point leads to impulsive magnetic reconnection at that point and, as predicted by *Southwood et al.* [1988] and *Scholer* [1988a], two large magnetic bulges are formed, one in the northern hemisphere and the other in the southern hemisphere. The spatial scale of each magnetic bulge at $t = 30t_A$ is $\sim 2R_E$ in the radial direction and $\sim 3R_E$ in the azimuthal direction, approximately the scale size of FTEs. Since no reconnections occur at higher latitudes, the magnetic field line at the poleward ends of the magnetic bulges are not closed (or reconnected). Hence the magnetic bulges are made up of open field lines only. It is seen that the shape of the two magnetic bulges are similar to magnetic islands (for example, those in Case 4) and, therefore, it is expected that these large magnetic bulges can bend magnetic field lines in the normal direction sufficiently to produce the FTE B_N bipolar signature also. As in the magnetic island case (Case 4), the two magnetic bulges formed at low latitudes are later convected poleward. By $t = 36t_A$, the major portion of the two magnetic bulges have been convected out of the low-latitude region. Associated with the magnetic bulges, as shown in Figure 2.29*b*, a region of enhanced plasma flow speed can be identified. This indicates that, like magnetic islands, the magnetic bulges are also moving poleward at a faster speed than the ambient plasma. The average tangential speed of the moving magnetic bulges is approximately the local Alfvén speed calculated in the immediate vicinity of the magnetic bulge on the magnetospheric side. This value of the convection speed of the magnetic bulge is the consequence of ongoing magnetic reconnection at the equatorward end of the magnetic bulge (subsolar point). Figure 2.30 shows the y-component of the electric field at the subsolar point E_{sp} (or reconnection rate) as a function of time. In Figure 2.30, E_{sp} increases sharply after $t \sim 26t_A$, reaching a peak at $t \sim 28.5t_A$, and afterwards drops sharply to less than one-third of the peak value. The profile of E_{sp}

suggests an impulsive reconnection process at the subsolar point similar to Case 4. This impulsiveness is caused by a sudden resistivity change.

In this simulation, the bursty single X-line reconnection process is reproduced by a sudden resistivity change at the subsolar point. In reality, there may be many other mechanisms to trigger a local impulsive reconnection. No matter what processes act as the initial triggering agents, the magnetic configuration and plasma flow features in a single X-line impulsive reconnection are expected to be similar to those in Case 7. The resultant magnetic bulge and the associated enhanced plasma flow speed shown in Case 7 suggest that bursty single X-line reconnections may be another potential source of FTEs, in addition to the multiple X-line reconnection process.

2.4.4 Multiple X-line reconnections versus bursty single X line reconnections

At first glance, multiple X-line reconnections and bursty single X-line reconnections seem to be two different processes. A close examination of the two reconnection processes will reveal some common features. First, the two reconnection processes are impulsive. Second, they share some topological resemblances. In fact, as already noted in subsection 2.3.2, each magnetic island formed at the dayside magnetopause in Case 4 is wrapped by a layer of open magnetic flux connecting the interplanetary magnetic field and the geomagnetic field (cf. Figure 2.15). Although in a multiple X-line reconnection process magnetic reconnections occur at several points, reconnection rates at different reconnection sites are not necessarily the same. The layers of open flux surrounding the magnetic islands in Case 4 are due to the fact that more magnetic flux is reconnected at the equatorward end of the magnetic islands. The open flux layer in Case 4 of multiple X line reconnection has been noted by *Sonnerup* [manuscript, 1988] who pointed out that this open flux layer forms the essential ingredient in Southwood et al.'s

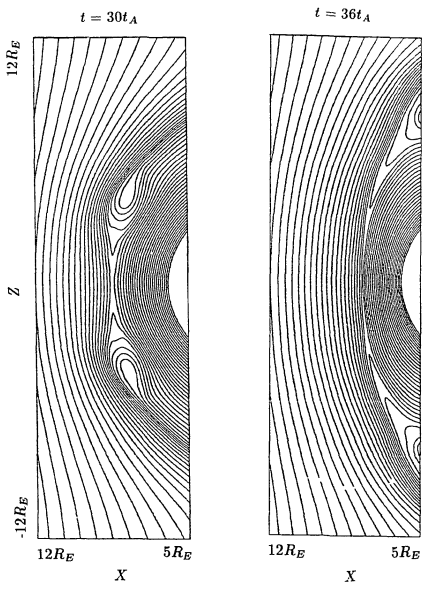

Figure 2.29 (a) Magnetic field configurations of Case 7 near the dayside magnetopause at $t = 30t_A$ and $t = 36t_A$. Bursty single X-line reconnection is shown.

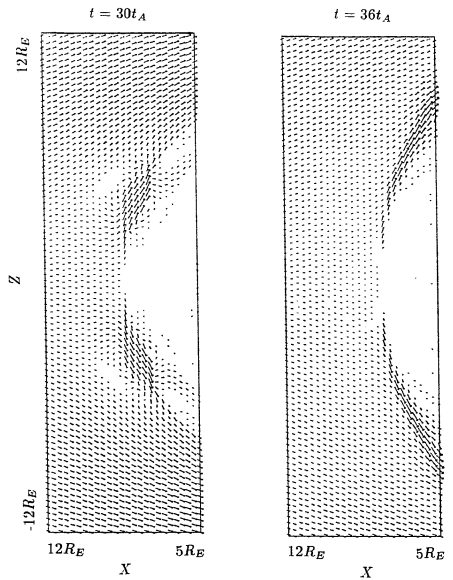

(b)

Figure 2.29 (b) Plasma flow patterns of Case 7 near the dayside magnetopause at $t = 30t_A$ and $t = 36t_A$.

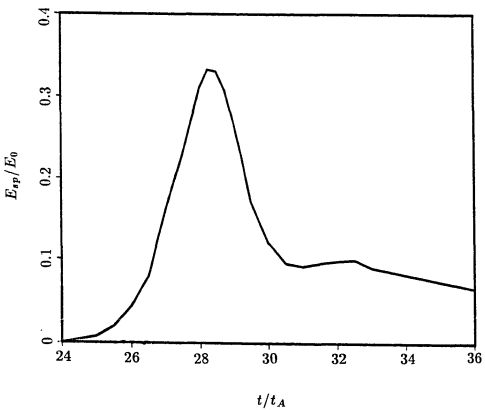

Figure 2.30 Variation of magnetic reconnection rate as defined by E_{sp} as a function of time at the subsolar point in Case 7.

and Scholer's bursty single X-line reconnection model. In two-dimensional geometry, the basic topological differences between the two reconnection processes are illustrated in Figure 2.31. Figure 2.31 shows magnetic structures resulting from multiple X line reconnections (left bulge in the figure) at two sites (marked by cross symbols) and single X-line bursty reconnection (right bulge in the figure). The left magnetic bulge in Figure 2.31 is assumed to be caused by two X-line reconnections with a larger reconnection rate at the lower end of the bulge. Suppose that for the left bulge in Figure 2.31, the magnetic reconnection rate at the lower reconnection site is much larger than that at the upper reconnection site. One would expect to see a thick layer of open magnetic flux surrounding a small island. When this difference of reconnection rates at two sites increases further, the magnetic island region will shrink further and become less identifiable. Therefore, bursty single X-line reconnection may be considered as an extreme case of two-site multiple X-line reconnections in which the reconnection rate at one of the reconnection sites approaches zero. In general, the magnetic structure resulting from multiple X line reconnections consists of one (several) open flux layer(s) and one (several) magnetic island region(s) while that resulting from bursty single X-line reconnection consists of an open flux layer only.

In three dimensions, the open flux layer in both reconnection models becomes a band of open magnetic field lines of finite longitudinal extent. These open field lines provide the coupling between the magnetosphere and the magnetosheath in a FTE event. In the presence of a B_y component in the interplanetary magnetic field, the magnetic island in two-dimensional case will become a magnetic flux tube. As pointed out by *Lee* [1986], magnetic flux tubes may be connected at one end to the geomagnetic field, or at both ends, or even not at all. In addition, the ionospheric footprint of the open flux band will also be in the form of a band extending in the longitudinal direction

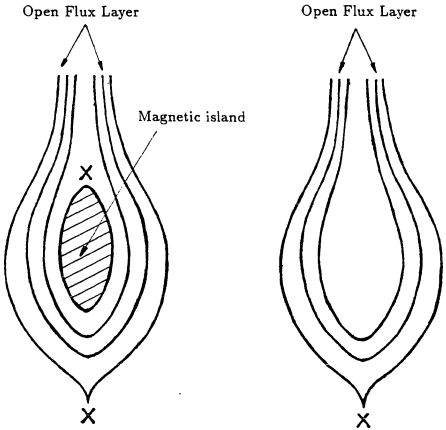

Figure 2.31 Schematic sketch of magnetic bulge structures resulting from the Lee-Fu type of multiple X-line reconnection (left bulge) and bursty single X-line reconnection (right bulge). The cross symbols represent reconnection sites or X line positions. Solid lines denote magnetic field lines and the shaded region in the left bulge represents a magnetic island region.

and that of the flux tubes will be in the form of a circular patch provided that at least one end of the flux tube is connected to the geomagnetic field.

Hence, multiple X-line reconnection is a more general form of the impulsive reconnection process, which in essence has included the bursty single X-line reconnections as an extreme case. Alinost all magnetic and plasma signatures resulting from bursty single X-line reconnection can be generated in multiple X-line reconnections, but not vice versa.

2.5. More on Multiple X Line Reconnections.

In sections 2.3, it was demonstrated that the multiple X-line reconnection as proposed by *Lee and Fu* [1985] is a possible type of dayside reconnection process and, in addition, may dominate the dayside reconnection processes due to the small resistivity in space plasma and the long dayside magnetopause. The single X-line reconnection, on the other hand, if it ever occurs at the dayside magnetopause, may take the form of bursty reconnection at the subsolar point as suggested by *Southwood et al.* [1988] and *Scholer* [1988a]. The latter assertion is supported by the observations too. Based on ISEE satellite data, *Sonnerup et al.* [1981] found that each of the reported instances of steady reconnection at the magnetopause has FTEs associated with it, [*Rijnbeek et al.*, 1984]. A comparison of these two reconnection models given in section 2.4 implies that multiple X-line reconnections should be considered as a more general form of dayside reconnections, including the bursty single X-line reconnection as an extreme case. Based on one simulation case of multiple X-line reconnection (Case 4), we have explored in section 2.4 one of the potential applications of Lee-Fu type of multiple X line recomections, namely, the interpretation of flux transfer events (FTEs). As established in section 2.4, the Lee-Fu type of multiple X-line reconnection (Case 4)

can indeed provide a consistent and natural explanation for FTEs. In this section, following a discussion of the 3-D effect on the multiple X-line reconnections, two other magnetospheric and ionospheric phenomena, the cusp region hydromagnetic waves and FTE footprints in ionosphere, will be discussed in relation to the Lee-Fu type multiple X-line reconnections.

2.5.1 Multiple X-line reconnections in three-dimensionality

In the two dimensional configurations, the Lee-Fu type of dayside multiple X-line reconnections are observed in the simulations, resulting in a chain of poleward moving magnetic islands (cf. Case 4) as predicted in the original Lee-Fu model. However, the corresponding three-dimensional configuration of these magnetic islands and related open field lines are not revealed in the simulations. The fundamental questions concerning the 3-D multiple X-line reconnections at the dayside magnetopause are: (1) what determines the longitudinal extent of the active reconnection region? (2) what is the reconnection geometry near the ends of the magnetic flux tubes?

In the presence of a finite y component in the interplanetary magnetic field, which is often the case, the 2-D magnetic islands would correspond to spiral magnetic flux tubes. At the dayside magnetopause, the length of these magnetic flux tubes should be finite. To produce magnetic flux tubes of finite longitudinal extent, the multiple X-line reconnections have to occur in a region of limited longitudinal extent. In the original Lee and Fu's multiple X-line reconnection model, the length of the flux tubes are long, 4–10 R_E. If the length of the flux tubes is reduced to $\sim$1–3 R_E, the process is called a patchy multiple X-line reconnection [*Lee*, 1986]. For the patchy multiple X-line reconnection process, *La Belle-Hamer et al.* [1988] have proposed a possible mechanism. They argued that Kelvin-Helmholtz (KH) instabilities at the dayside magnetopause can

modulate the current sheet, creating separated pinched regions. Since the growth rate of the tearing instability will be enhanced in these pinched current sheet regions and diminished in the regions separating them, patchy multiple X-line reconnections are expected to occur. On the other hand, the geometry of the magnetopause surface itself and the solar wind flow may naturally modulate dayside reconnections on a large scale. In a recent local 3-D MHD simulation of driven multiple X-line reconnections [*Fu, Lee, and Shi*, manuscript, 1989], the magnetic flux tubes caused by multiple X-line reconnections are observed to be formed first near the stagnation point. The magnetic flux tubes are short at this stage. Later, as the active reconnection regions along several X lines begin to shift sideways, the length of the magnetic flux tubes increases while the flux tubes are being convected outward at the same time. This result may apply to 3-D reconnection processes at the dayside magnetopause subsolar point which is the stagnation point for solar wind flows. Despite the above hypothesis on the processes which may be responsible for the finiteness of magnetic flux tubes resulting from multiple X line reconnection, no conclusive evidence has been provided in either La Belle-Hamer et al.'s work or the 3-D simulation by *Fu, Lee, and Shi* [manuscript, 1989]. First, the patchy mechanism proposed by *La Belle-Hamer et al.* [1988] remains to be tested in 3-D simulations (their original work was based only on 2-D simulations). Second, the significance of the stagnation point flow in determining the length of the flux tube requires a systematic study.

Another aspect of the 3-D multiple X-line reconnection that is still not very clear is the reconnection geometry at the two ends of the magnetic flux tube. As shown in Figure 2.15, in a 2-D situation, the formed magnetic island is clearly decoupled from both the interplanetary magnetic field (IMF) and the geomagnetic field. In a 3-D situation, the magnetic flux tube can also provide such coupling through connections to the IMF at one end of the flux tube and to the geomagnetic field at the other. However,

the reconnection topology at the ends of the magnetic flux tubes may not be as simple as envisioned in theoretical models since most of these assume that all magnetic field lines at the ends of the flux tubes will be reconnected collectively either to the IMF or to the geomagnetic field. The 3-D simulation by *Fu, Lee and Shi*[manuscript, 1989] demonstrated that the reconnection topology at the ends of magnetic flux tubes are highly complicated. Their simulation indicates that at the end of the magnetic flux tube, the tube field lines will reconnect with field lines on both sides of the current sheet in a chaotic way, forming the so-called "frayed" flux tubes. The effect of the frayed flux tubes on the coupling of the IMF and geomagnetic field is worth further investigation.

2.5.2 Cusp region hydromagnetic waves

Ground-based studies of the cusp region magnetic field variations in the ultralow frequency (ULF) range ($\sim 10^{-3}$–10^{-1} Hz) have provided evidence that some of the variations are associated with the proximity of the observing location to the cusp [e.g., *Samson et al.*, 1971; *Troitskaya*, 1984; *Olson*, 1986]. *Olson* [1986] examined ULF variations in data acquired at two polar cap stations (Cape Parry and Sachs Harbor, Northwest Territories, Canada). He reported that enhanced power occurred in the ULF band near local noon on almost every day, principally at frequencies near 1–10 and 30–50 mHz. He identified the 1- to 10- mHz band with fluctuations in the ionospheric currents associated with the cusp boundary and its motions, whereas he attributed the power in the 30- and 50- mHz band to direct penetration of hydromagnetic radiation from the cusp. The in-situ near-Earth observations by spacecraft also have reported the more or less continuous presence of variations in the magnetic field in the ULF range in the cusp region [e.g., *Frank*, 1971; *Heikkila and Winningham*, 1971]. *Glassmeier et al.* [1984]

performed a case study using simultaneous data from ISEE 1 and 2 near the dayside magnetopause, from GOES 2 and 3 satellites at synchronous altitude, and from a number of ground-based stations. They concluded that FTEs are likely candidates for some Pc 5 range pulsations.

Motivated by the above observations, *Lee et al.* [1988] proposed a generation mechanism for some of the cusp region hydromagnetic waves, especially the Pc 5 pulsations. They argued that the magnetic islands (or flux tubes) formed in multiple X-line reconnections will compress the adjacent geomagnetic field lines and, as a result, magnetic ripples are produced on these closed geomagnetic field lines. Along with the poleward-moving magnetic islands, the rippled magnetic fields will propagate toward the cusp region and eventually down to the ionosphere. If FTEs are due to multiple X-line reconnection as suggested by *Lee and Fu* [1985], then the time scale of these magnetic ripples can be determined from the FTEs. The observed duration of a single FTE event is observed to about 2 minutes, with an interval between successive events of about 5–10 minutes. Therefore, the period of oscillations (ripples) on closed geomagnetic field lines will be $T \sim$ 2–10 min. The period corresponds to a frequency of 2–8 mHz, falling into the range of Pc 5 pulsations. Therefore, they concluded that multiple X-line reconnection may be one of the energy sources for the generation of cusp region ultralow-frequency hydromagnetic waves. The above generation process can be illustrated in the present simulations. In Figure 2.15, which shows the evolution of magnetic islands due to Lee-Fu type of multiple X-line reconnection, the formation and subsequent poleward convection of magnetic islands along the dayside magnetopause indeed generate propagating magnetic ripples on the outermost closed geomagnetic field lines.

2.5.3 FTE footprints in the ionosphere

As discussed above, the magnetic flux tubes formed in 3-D multiple X-line reconnections may exhibit highly complicated tube-end reconnection topology. However complicated the reconnection topology may be, those flux tube field lines connected with geomagnetic field lines will provide coupling of the magnetic flux tubes to the geomagnetic fields and subsequently to the ionosphere. It is predicated in the multiple X-line reconnection model that field-aligned current, $J_{\parallel}$, is generated by the spiral magnetic field structure in the flux tubes and that if the magnetic flux tubes are connected to the geomagnetic field, the transverse magnetic field of the flux tube will propagate as Alfvén waves away from the magnetopause towards the ionosphere. Along with the Alfvén waves, $J_{\parallel}$ will also propagate down into the ionosphere. The injection of $J_{\parallel}$ into the ionosphere can produce one large vortex in the ionosphere [*Lee*, 1986]. The highly localized $J_{\parallel}$ in the ionosphere would induce an impulse in the vertical component of the magnetic field. Such an impulse in the vertical component of the ground magnetic field has been observed by *Lanzerotti et al.* [1986].

2.6. Summary and Discussion

This chapter presented studies of the magnetic reconnections at the dayside magnetopause by a 2-D global incompressible MHD simulation. By including the global geometry of the geomagnetic dipole field and that of solar wind flow and the interplanetary magnetic field, the simulation presented in this chapter successfully reproduces the impulsive multiple X-line reconnection process [*Lee and Fu*, 1985] on a global scale at the dayside magnetopause. In addition to the Lee-Fu type multiple X-line reconnections, other dayside reconnection processes predicted by theories or observed in experiment are also simulated, notably, the quasi-steady state single X-line reconnection, the

bursty single X-line reconnection, and the high-latitude multiple X-line reconnection. In particular, the magnetic and plasma signatures produced by Lee-Fu type multiple X-line reconnections in the simulation are applied to explain the observed flux transfer events (FTEs) at the dayside magnetopause. Major results obtained in this chapter are summarized below:

1. Magnetic reconnection at the earth's dayside magnetopause is found to be characterized by its diversity of reconnection patterns. In the single X-line reconnection category, the quasi-steady state subsolar point reconnection suggested first by *Dungey* [1961] and bursty reconnections proposed by *Southwood et al.* [1988] and *Scholer* [1988a] are shown to be two possible dayside reconnection processes; in the multiple X-line reconnection category, Lee-Fu type reconnection and high-latitude reconnection are seen; other reconnection patterns which are still not described in the available theories are also observed.

2. On the basis of the simulation cases in section 2.3.1, it is suggested that the transition of recomection patterns from the quasi-steady state single X line type to the multiple X-line type is determined by the magnetic Reynolds number at the dayside magnetopause. In the simulation, quasi-steady state single X-line reconnection is observed to occur only for small magnetic Reynolds numbers ($\leq$ 100 in the simulation), while multiple X-line reconnection occurs when the magnetic Reynolds number is large ($\geq$ 200 in the simulation). The occurrence of multiple X line reconnections is speculated to be caused by the unstable tearing mode or local fluctuations due to the nonuniform solar pressure and IMF stresses. In either case, the existence of a long magnetopause current sheet caused by a large magnetic Reynolds number is a necessary condition. Since the observed magnetopause is long, it is suggested that multiple X-line reconnection may dominate the dayside reconnection processes.

3. For the Dungey type single X-line reconnection at the subsolar point, Case 1 in subsection 2.3.1 implies that a global steady state may not exist due to the constant erosion of the magnetopause. The erosion of the magnetopause has been observed by satellites. However, it is possible to define a local quasi-steady state of reconnection near the subsolar point in the frame of a moving subsolar point.

4. In the multiple X-line reconnection category, the current-dependent anomalous resistivity and the solar wind Alfvén Mach number are found to be two additional parameters capable of modifying the reconnection patterns.

In the absence of the current-dependent resistivity (or in case of constant resistivity), dayside reconnection occurs always at two points on each side of the subsolar point, forming a stagnant magnetic island. However, various reconnection patterns may appear, if the current-dependent resistivity is added. In that case, reconnection tends to occur wherever the current density in the magnetopause current layer exceeds the critical current density, J_c, for the enhancement of the current-dependent resistivity (see (2.5)). Hence, the critical current density, J_c, is the most important parameter in current-dependent resistivity. With a J_c of the order of the average current density in a tangential magnetopause (Case 3 in subsection 2.3.2), local fluctuations in the magnetopause current layer lead to formation of several magnetic islands. In this case, the tearing mode instability may be important in regulating the reconnection pattern. On the other hand, with a J_c much larger than the average current density in the magnetopause, reconnection will occur where the magnetopause current sheet is most pinched by the solar wind (for example, at high latitude in Case 6). In this case, the reconnection pattern may depend largely on the solar-wind dynamic pressure and IMF stresses.

One example of the effect of the current-dependent anomalous resistivity, the Lee-Fu type of multiple X-line reconnection, was simulated in subsection 2.3.2. The Lee-Fu type reconnection is characterized by the formation and convection of small-scale magnetic islands (of spatial scale of $\sim 2R_E$) along the dayside magnetopause. One interesting feature found in the Lee-Fu type of reconnection is the bipolar structure of the dawn-dusk component of the electric fields.

In subsection 2.3.3, the effect of the solar wind Alfvén Mach number was explored. It is found that when the solar wind Alfvén number is large, the dayside reconnections tend to occur at higher latitude. This dependence of the reconnection types on the solar wind Alfvén Mach number is qualitatively consistent with laboratory experiments [*Podgorny et al.*, 1978].

5. For the Lee-Fu type of dayside reconnections, a comparison is made in subsection 2.4.2 between the magnetic and plasma signatures produced by the reconnection process and that of the observed FTEs. As predicted in the original Lee-Fu's FTE model, it is observed in the simulation that Lee-Fu type multiple X-line reconnections can indeed produce the primary FTE identifying signature, i.e., the bipolar B_N signature, and the associated enhanced plasma flow speed. Consistent with the observations of the internal flow structure of FTEs, the enhanced plasma flow speed is also found to be concentrated or peaking in the trailing end of each bipolar B_N impulse (FTEs).

Another FTE model, the bursty single X-line reconnection, is also simulated in subsection 2.4.3 and compared with Lee-Fu's model. It is suggested in section 2.4.4 that the bursty single X-line reconnection may represent an extreme case of the Lee-Fu type reconnection process.

The final remarks in this section concern the limitations and applicability of the simulation results obtained in this chapter. Because of limited computer memory and

computing time, the simulation model used in this chapter is subject, as are most global simulations, to various degrees of simplifications.

First, the simulation is a two-dimensional one. Three-dimensionality may modify the dependence of the dayside reconnection patterns on the parameters studied in this chapter. On the global scale ($\sim 10R_E$), the interplanetary magnetic fields (IMF) may slip around the magnetopause surface and move tailward in the real 3-D magnetosphere, leading to a lesser degree of magnetic flux pile-up in front of the dayside magnetopause. On the small scale (of the order of 1 R_E), the magnetic islands resulting from 2-D multiple X-line reconnection becomes magnetic flux tubes in a 3-D situation. As discussed in section 2.5, the 3-D counterpart of magnetic islands, magnetic flux tubes, will introduce new topological and dynamic problems.

Second, the simulation is an incompressible MHD simulation. Two of the consequences of the incompressible simplification are the absence of the bow shock in front of the dayside magnetopause and the lack of plasma density asymmetry at the dayside magnetopause. In the reality, the plasma density on the magnetosheath side of the magnetopause is much higher than that on the magnetospheric side. As will be demonstrated in Chapter 3, the plasma density asymmetry at the magnetopause may have direct impact on the dayside reconnection layer structure. On the other hand, the IMF flux pile-up region in front of the magnetopause present in each simulation case may be considered as corresponding to the magnetosheath region behind the bow shock. It is anticipated that apart from the possibility of the fine layer structures of the dayside reconnection being modified by the plasma density asymmetry, the compressibility effect on the overall reconnection patterns should be small [*Lee and Fu*, 1986*a*; *Lee and Fu*, 1986*b*]. Hence, the present incompressible approach can still provide useful information regarding the dayside magnetic reconnections.

Third, though the spatial resolution in the present simulation near the dayside magnetopause is the highest ($0.075R_E$) among all reported global simulations, the grid size at the magnetopause may still be large compared to the thickness of the observed magnetopause current layer, which is about 300 km–1000 km ($\sim 0.05R_E$–$0.15R_E$) [*Berchem and Russell*, 1982]. As a result, the thickness of the magnetopause current layer formed in the present simulation is larger than the observed thickness (for example, it is $\sim 0.5R_E$ in Case 4 at $t = 26t_A$). For an improved spatial resolution, the thickness of the magnetopause current layer can be further reduced in the simulation. This would in effect increase the length of the magnetopause current layer. A longer current sheet will make the dayside magnetopause more susceptible to the multiple X-line type of reconnections. Hence, the spatial resolution used at the dayside magnetopause in this simulation should not affect the statement made above that the dayside reconnection may favor the multiple X-line type.

Finally, the coupling of the dayside reconnections to the ionosphere and magnetotail is not included in the simulation. The ionospheric boundary in the simulation is represented by a simple numerical boundary at a radius of $2.5R_E$, which is designed to absorb all the incoming waves in that region. On the nightside, a low-resolution grid mesh is used. In reality, the ionosphere and processes in the magnetotail may also influence the dayside reconnection.

Chapter 3. Structure of the Reconnection Layer at the Dayside Magnetopause

3.1 Introduction

In the framework of magnetohydrodynamic formulation, a number of theoretical models have been proposed to describe the magnetic reconnection processes. The earliest Sweet-Parker [*Sweet*, 1958; *Parker*, 1957, 1963] model describes a magnetic field annihilation process in which there is a small inflow of plasma towards a current layer separating two regions of antiparallel magnetic fields. The magnetic field reconnection rate in Sweet-Parker model is mainly determined by the resistivity. Since in space plasma the resistivity is usually very small, the reconnection rate in the Sweet-Parker model turns out to be too small to account for any significant energy conversion. *Petschek* [1964] suggested a new reconnection model in which the reconnection region consists of a small diffusion region of Sweet-Parker type and two pairs of slow shocks attached to the diffusion region. In Petschek's model, a large reconnection rate is achieved due to the acceleration of incoming plasma by slow shocks, an efficient way of converting magnetic field energy to plasma thermal and flow energy.

The important contribution of Petschek is the idea that the diffusion region, where magnetic reconnection actually occurs, is only a small region of the entire reconnection configuration and the large part of energy conversion takes place in the so-called convection region or the reconnection layer. In Petschek's picture, the configuration of

magnetic reconnection consists of two inflow regions, two outflow regions, and a diffusion region. The outflow region has been variously referred to as "boundary layer" [*Petschek*, 1964], "field reversal region" [*Vasyliunas*, 1975], and "reconnection layer" [*Heyn et al.*, 1988]. Here we will adopt the terminology of *Heyn et al.* [1988]. Figure 3.1 illustrates schematically the configuration of magnetic reconnection based on Petschek's model. In Petschek's model, the reconnection layer is bounded by two pairs of slow shocks. The subsequent dayside reconnection models have mostly originated from Petschek's idea, namely, a large outflow region and a small diffusion region. However, Petschek's model only applies in a symmetric case with identical plasma and magnetic field configurations on the two sides of the current layer. At the earth's dayside magnetopause, the plasma and magnetic configurations on the magnetosheath and magnetospheric sides are highly asymmetric. Hence, in most of the following dayside reconnection models, Petschek's recomection layer has been further modified to incorporate the asymmetry at the dayside magnetopause.

Levy et al. [1964] were the first to propose a qualitative reconnection model for the asymmetric flow and field conditions at the earth's dayside magnetopause. They considered the extreme case in which the plasma density on the magnetospheric side is exactly zero. In their model, the pair of slow shocks bounding the reconnection layer in Petschek's model is replaced by an intermediate wave (rotational discontinuity; large amplitude Alfvén wave) and a narrow slow expansion fan. The intermediate wave, which marks the magnetopause, accomplishes the magnetic field direction reversal and an associated plasma acceleration parallel to the magnetopause. The magnetic field magnitude remains unchanged across this wave but it then increases to its higher magnetospheric value in the slow expansion fan across which the plasma pressure also is reduced to match the low pressure in the magnetosphere. *Levy et al.*'s [1964] model was later further elaborated by *Yang and Sonnerup* [1977] as shown in Figure 3.2. Note,

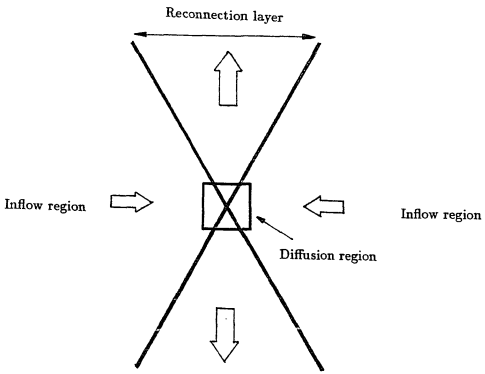

Figure 3.1 The configuration of magnetic reconnection in the Petschek model. The plasma inflow regions are to the left and right of the figure. They enclose a small central diffusion region above and below which are the two outflow regions or the reconnection layer.

in Figure 3.2, that an expansion wave is assumed in the magnetosheath to bend the magnetosheath field lines. In reality, this expansion wave may not exist and the bending of magnetic field lines in the magnetosheath proceeds in a much smoother way as they approach the magnetopause.

In a recent theoretical paper, *Heyn et al.* [1988] have extended the analysis of *Petschek* [1964] so that the Petschek model can now in principle be used to predict the structure of the reconnection layer for the general case of unequal plasma densities, arbitrary magnetic fields and plasma velocities. They formulated the reconnection process in terms of a Riemann problem, i.e., an initial value problem using the ideal MHD equations. As an initial condition, they took two constant states separated by a tangential discontinuity. Following the introduction of a localized tangential electric field, or switch-on of reconnection, the accompanying perpendicular field and flow components propagate along the initial tangential discontinuity which then evolves into several MHD wave modes. The reconnection layer in their model is in general bounded by two rotational discontinuities, and, inside the reconnection layer, slow shocks or slow expansion fans are needed to form a match between the different magnetic field strengths on the two sides. Using realistic values for the plasma and magnetic field quantities appropriate to Earth's dayside magnetopause, *Biernat et al.* [1988] have applied Heyn et al.'s analysis to the dayside magnetopause. They found that in general, the reconnection layer structure is intermediate to those analysed by *Petschek* [1964] and *Levy et al.* [1964], who assumed complete symmetry (equal number densities and field strengths) and asymmetry (zero magnetospheric number density), respectively.

By using ISEE and AMPTE satellite data, some authors [*Paschmann et al.*, 1979; *Sonnerup et al.*, 1981; *Gosling et al.*, 1982; *Paschmann et al.*, 1986] have shown evidence for the occurrence of the large-amplitude Alfvén waves (rotational discontinuities), as predicted in Levy et al.'s model, at the earth's magnetopause. Their most important

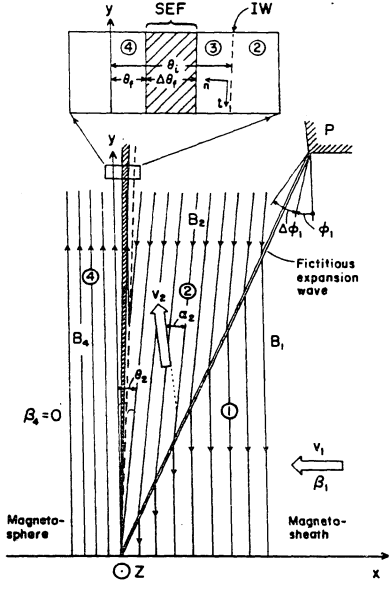

Figure 3.2 Levy et al.'s [1964] dayside reconnection model. Upper half of compressible slow-mode model of magnetopause reconnection for $M_{A1} = 0.2$ and $\beta_1 = 2\mu_0 p_1 / B_1^2 = 2$. The intermediate wave (IW) marking the magnetopause is shown as a dashed line. The slow mode expansion fan (SEF) is shaded (Yang and Sonnerup [1977]).

criterion for identifying reconnection was the detection of accelerated plasma flows near the magnetopause. More recently, *Rijnbeek et al.* [1988] re-examined the ISEE data from a magnetopause crossing on 8 September 1978 previously interpreted as an example of magnetic reconnection. They found from the data strong evidence for a combination of slow shocks and Alfvén waves. They concluded that the concept of reconnection layer proposed by *Petschek* [1964] provides a useful framework for interpreting satellite data. However, due to the insufficient observational data, the dayside reconnection configuration remains unclear. On the other hand, in the earth's magnetotail where the plasma and magnetic field configurations are more or less symmetric, the existence of standing slow shocks in Petschek's model was confirmed by *Feldmann et al.* [1984, 1987] using ISEE 3 satellite data.

This chapter presents studies of the structure of the reconnection layer under different symmetry conditions through numerical simulations using a two-dimensional magnetohydrodynamic code. Specifically, the study systematically considered how the reconnection layer structure varies with the degree of asymmetry in magnetic fields and plasma densities on the two sides of a plane current sheet. The results will be applied to the dayside magnetopause.

The simulation model is described in section 3.2 and the simulation cases are presented and discussed in section 3.3. Based on the simulation results, the possible dayside reconnection layer structures are discussed in section 3.4. Subsection 3.5 contains the summary of this chapter.

3.2 Simulation Model

3.2.1 Basic equations

A two-dimensional compressible magnetohydrodynamic (MHD) simulation was carried out to study the reconnection layer structures in an asymmetric configuration characteristic of the dayside magnetopause. The basic equations are the set of one-fluid MHD equations:

$$\frac{\partial \rho}{\partial t} = -\nabla \cdot (\rho \mathbf{v}) \tag{3.1}$$

$$\frac{\partial (\rho \mathbf{v})}{\partial t} = -\nabla \cdot [\rho \mathbf{v}\mathbf{v} + (p + \frac{B^2}{2\mu_0})I - \frac{1}{\mu_0}\mathbf{B}\mathbf{B}] \tag{3.2}$$

$$\frac{\partial \mathbf{B}}{\partial t} = \nabla \times (\mathbf{v} \times \mathbf{B}) - \nabla \times (\eta \mathbf{j}) \tag{3.3}$$

$$\frac{\partial \epsilon}{\partial t} = -\nabla \cdot \mathbf{S} \tag{3.4}$$

with

$$\mathbf{j} = \frac{1}{\mu_0} \nabla \times \mathbf{B} \tag{3.5}$$

$$\mathbf{S} = (\epsilon + p + B^2/2\mu_0)\mathbf{v} - (\mathbf{B} \cdot \mathbf{v})\mathbf{B}/\mu_0 + \eta \mathbf{j} \times \mathbf{B}/\mu_0 \tag{3.6}$$

$$\epsilon = \rho v^2/2 + B^2/2\mu_0 + p/(\gamma - 1) \tag{3.7}$$

where ρ is the plasma mass density, $\mathbf{v}$ is the velocity, p is the gas pressure, $\mathbf{B}$ is the magnetic field, $\mathbf{j}$ is the electrical current density, η is the electrical resistivity, γ is the adiabatic constant chosen to be $\gamma = 5/3$, μ_0 is the magnetic permeability in free space, and I is a unit tensor.

3.2.2 Initial Conditions

The present simulation is a local one which simulates the magnetic reconnection in a slab current sheet, which is a plane perpendicular to the x-axis and centered at $x = x_0$. The initial magnetic fields on both sides of the current sheet are strictly antiparallel and contain only the z component. In the dayside magnetopause situation, the x-axis and z-axis in the simulation are in the sunward direction and in the northward direction,

respectively. In such an initial current sheet configuration, each physical quantity varies in the x-direction. Specifically, the initial magnetic field configuration is given by

$$B_z(x) = \frac{1}{2}(B_{10} - B_{20}) - \frac{1}{2}(B_{10} + B_{20}) \tanh[(x - x_0)/a] \tag{3.8}$$

where B_{10} and B_{20} are the magnetic field strengths on Side 1 and Side 2 of the current sheet, respectively, and a is the half-thickness of the current sheet. The initial plasma density is given by

$$\rho(x) = \frac{1}{2}(\rho_{10} + \rho_{20}) + \frac{1}{2}(\rho_{20} - \rho_{10}) \tanh[(x - x_0)/a] \tag{3.9}$$

where ρ_{10} and ρ_{20} are the plasma densities on Side 1 and Side 2 of the current sheet, respectively. Note that in the asymmetric cases of the subsequent simulations, Side 1 denotes the magnetospheric side and Side 2 the magnetosheath side. Hence, B_{10} and ρ_{20} are always greater than or equal to B_{20} and ρ_{10}, respectively, since the magnetic field strength on the magnetosheath side of the magnetopause current layer is usually smaller than that on the magnetospheric side while the opposite is true for the plasma density.

The initial configuration is set in a pressure equilibrium which requires that the total pressure, the magnetic pressure plus gas pressure, is constant throughout the simulation domain. If we now define β_1 and β_2 to be the ratios of gas pressure to magnetic pressure on Side 1 and Side 2, respectively, the initial condition of pressure balance can be expressed as

$$\frac{B_{10}^2}{2\mu_0}(1 + \beta_1) = \frac{B_{20}^2}{2\mu_0}(1 + \beta_2) = \frac{B^2(x)}{2\mu_0} + p(x), \tag{3.10}$$

where $B_{10}^2/2\mu_0$ and $B_{20}^2/2\mu_0$ are magnetic pressures on Side 1 and Side 2. Hence, the initial pressure profile is determined by (3.8) and (3.10)

Figure 3.3 illustrates schematically the initial profiles of z component of magnetic field $\mathbf{B}_x$, y component of the current density J_y, plasma density ρ, and gas pressure p.

In addition, only the spontaneous magnetic reconnection processes were simulated for this chapter and, therefore, the initial plasma velocity was set to zero everywhere in the simulation box.

3.2.3 Numerical procedures

The simulation domain is a rectangular box in the x-z plane, extending in the x direction from -10a to 10a and from 0 to -40a in the z direction. In all simulation cases, magnetic reconnection will be triggered at the $(x, z) = (x_c, 0)$ point, where $x = x_c$ is the position at which the initial $B_z(x)$ is zero. Note that in the asymmetric case, x_c is different from x_0 in (3.8). In the case of the dayside magnetopause, the simulation domain is in the southern hemisphere with the subsolar point of the dayside magnetopause located at the reconnection point, or X point. Therefore, the system is assumed to be symmetric about the simulation boundary at $z = 0$. For the whole simulation domain, 101×72 grid points are used and the grid mesh is uniform. The resolution is then $\Delta x = 0.2a$ in x and $\Delta z = 0.56a$ in z.

Since only spontaneous magnetic reconnection processes will be simulated, the simulation boundaries at $x = -10a$, $10a$, and $z = 40a$ are assumed to be "free" on which the derivative of each physical quantity with respect to the boundary normal direction is set to zero. The bomdary at $z = 0$, as mentioned above, is a symmetric

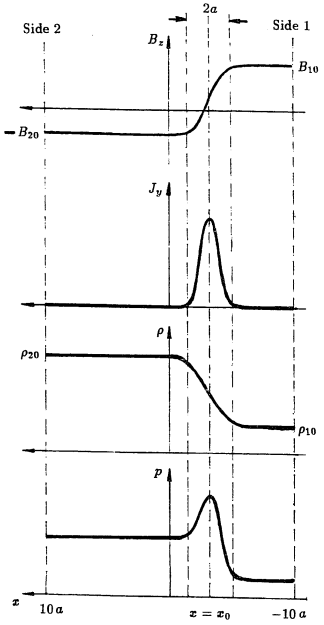

Figure 3.3 Schematic illustration of the initial profiles of B_z, J_y, ρ, and p in the simulation. The thickness of the initial current sheet centered at $x = x_0$ is $2a$.

one on which the following symmetric (or antisymmetric) conditions are imposed

$$\begin{cases} B_x(x,z) = B_x(x,-z), \\ B_z(x,z) = -B_z(x,-z), \\ \rho(x,z) = \rho(x,-z), \\ v_x(x,z) = v_x(x,-z), \\ v_z(x,z) = -v_z(x,-z), \\ p(x,z) = p(x,-z), \end{cases} \tag{3.11}$$

where v_x and v_z are the x and z components of the plasma velocity and p is the gas pressure.

In the simulation, the three basic quantities used for normalization are the initial magnetic field strength B_{20} and initial plasma density ρ_{20} on Side 2 of the initial current sheet and the initial current sheet half-thickness a (note that in the asymmetric case, Side 2 is the magnetosheath side). Normalization units of all the physical quantities are expressed as a function of these three basic quantities. Table 3.1 lists the normalization units for each physical quantity.

TABLE 3.1 Normalization Units of the Simulation

physical quantity	normalization unit
magnetic field	$B_0 = B_{20}$
plasma density	$\rho_0 = \rho_{20}$
velocity	$V_{A0} = B_{20}/\sqrt{\mu_0 \rho_{20}}$
pressure	$p_0 = B_{20}^2/\mu_0$
length	a
current density	$j_0 = B_{20}/\mu_0 a$
resistivity	$\eta_0 = \mu_0 a V_{A0}$
time	$t_A = a/V_{A0}$

Note that in Table 3.1, the normalization unit for velocity V_{A0} is the Alfvén velocity on Side 2, the magnetosheath side in the asymmetric cases, of the current sheet and the normalization unit for time t_A is the Alfvén transit time based on a and V_{A0}.

Finally, the finite differencing method used for equations (3.1)–(3.4) is the two-step Lax-Wendroff scheme with a third-order artificial diffusion term [*Lapidius*, 1967]. A detailed description of the numerical scheme is presented in the Appendix.

3.2.4 Initialization of reconnection

In MHD simulations of magnetic reconnection initialized from a plane model of current sheet configuration (like the one used here), two different methods have been used. The first method is the driven experiment [e.g., *Hayashi and Sato*, 1978; *Biskamp*, 1986; *Lee and Fu*, 1986*a*]. In the driven experiments, the plasmas and magnetic fields on the two sides of the current sheet plane are pushed towards the current sheet region to initiate the magnetic reconnection. For this reason, the magnetic reconnection achieved in this way has been termed "driven reconnection". In the second method, the magnetic reconnection is triggered by a local resistivity enhancement (anomalous resistivity effect) at the center of the current sheet. The magnetic reconnection achieved by this method is sometimes called "spontaneous reconnection" [e.g., *Ugai and Tsuda*, 1977; *Ugai*, 1983, 1984; *Scholer*, 1989]. In the present simulation, the magnetic reconnection will be initiated by the latter method, namely, an assumed local resistivity enhancement.

In particular, the resistivity used in the present simulation is assumed as

$$\eta = \eta_a e^{-(x-x_c)^2/x_i^2} e^{-z^2/z_i^2} (1 - e^{-t/\tau}) + \eta_b, \tag{3.12}$$

A resistivity enhancement model similar to the one in (3.12) has been used by *Scholer* [1989]. The first term on the right-hand side of (3.12) is the local time-dependent

resistivity which increases from zero at $t = 0$ to a maximum of η_a over a time period of about τ within a local region centered at $(x, z) = (x_c, 0)$ (recall x_c is the location in the initial current sheet where B_z is zero). The spatial scale of the local region for the resistivity enhancement is about x_l in the x direction and z_l in the z direction. The second term on the right-hand side of (3.12) is a small constant background resistivity. In the simulation, the following parameters are chosen for the resistivity model: $\eta_a = 0.1\eta_0$, $\eta_b = 0.001\eta_0$, $x_l = 2a$, $z_l = 3a$ and $\tau = 10t_A$. x_c is determined in individual cases depending on x_0, B_{10} and B_{20}.

3.3 Reconnection Layer Structures: Simulation Results

The simulation cases presented in this section will demonstrate that the reconnection layer structure in a 2-D configuration varies significantly depending on the degree of asymmetry between the two sides of the current sheet plane. For a symmetric current sheet configuration, a pair of slow shocks are observed in the simulation as predicted by *Petschek* [1964]. However, in an asymmetric configuration typical of the dayside magnetopause, the pair of slow shocks observed in the symmetric case is replaced by an intermediate shock on the magnetosheath side and a weak slow shock (barely identifiable in some cases) on the magnetospheric side. The number and features of the MHD discontinuities in the reconnection layer are found to be related directly to the degree of asymmetry in the plasma densities and magnetic field on the two sides of the current sheet. In addition, the plasma β value, the ratio of gas pressure to magnetic pressure, is found to be another parameter that can modify the strength of the MHD shocks. With increasing β, the shock structures in the recomection layer tend to become weaker.

The intermediate shocks were earlier classified as extraneous solutions of the Rankine-Hugoniot equations [e.g., *Jeffrey and Taniuti*, 1964; *Kantrowitz and Petschek*, 1966].

However, the recent numerical results from *Wu* [1987, 1988*a*, 1988*b*] based on resistive MHD equations show that a nonlinear plane transverse MHD wave can steepen to form an intermediate shock which appears stable and that, in the interaction between a non-coplanar rotational discontinuity and an intermediate shock, a long time may elapse before the disintegration predicted by *Kantrowitz and Petschek* [1966] takes place. Based on these results, Wu has proposed that intermediate shocks may be present in many space plasma situations in the solar wind or at the earth's dayside magnetopause during reconnection events. The structure of resistive MHD intermediate shocks has also been examined recently by *Hau and Sonnerup* [1988].

Seven simulation cases will be presented in this section. Table 3.2 lists the parameters used in each simulation case and the major features of the reconnection layer revealed.

TABLE 3.2 Simulation cases and parameters used

case	layer structure	B_{10}/B_{20}	ρ_{10}/ρ_{20}	β_1	β_2
Case 1	SS & SS	1	1	0.1	0.1
Case 2		1	1	5	5
Case 3	SS(IS) & SS	1.5	1	0.1	1.5
Case 4	SS & SS	1	0.5	0.1	0.1
Case 5	IS & SS	1	0.1	0.1	0.1
Case 6	IS & SS	1.5	0.1	0.1	1.5
Case 7		3	0.1	0.1	9

The second column in Table 3.2 gives the discontinuities bounding the reconnection layer observed in the corresponding cases, where SS and IS denote slow shock and intermediate shock, respectively.

3.3.1 Symmetric magnetic reconnections

Two symmetric cases, Case 1 and Case 2, are simulated with largely distinctive β values. In both Case 1 and Case 2, the initial plasma densities and magnetic fields are set to be equal on the two sides of the current sheet. The purposes of Case 1 and Case 2 are, first, to show the pair of slow shock structures in the reconnection layer as predicted in the classical symmetric reconnection model, and, second, to study the effect of β on the MHD discontinuity structure.

Case 1: small β case

In Case 1, $\beta = 0.1$ is used. Figure 3.4 shows the evolution of the magnetic field, plasma velocity field, and current sheets at two different times $t = 37t_A$ (Figure 3.4*a*) and $t = 63t_A$ (Figure 3.4*b*). Figure 3.5 shows the corresponding 3-D profiles of current density J_y at $t = 37t_A$ and $t = 63t_A$. At $t = 37t_A$, a small magnetic bulge is formed in the current sheet as a result of magnetic reconnection at $(x, z) = (0, 0)$. Associated with the magnetic bulge, the current bifurcates into two distinctive sheets that correspond to two MHD discontinuities. Within the magnetic bulge region, plasmas are accelerated in the negative z direction. At $t = 63t_A$, the size of the bulge has grown in both x and z directions. The formation of a magnetic bulge due to the sudden enhancement of the local reconnection rate at a single X point and the associated slow shocks have been predicted and studied analytically by *Biernat et al.* [1987]. In their calculation, the magnetic bulge that formed will propagate with the upstream Alfvén speed along the current sheet away from the reconnection site after reconnection is switched off. In Case 1, a comparison between the magnetic field configuration at $t = 37t_A$ and $t = 63t_A$ shows that the bulge is also propagating in the negative z direction. Again associated with the magnetic bulge at $t = 63t_A$ are two current sheets. Across these two current

sheets, the magnetic field lines (approximately in the $z > -24a$ region) are bent sharply towards the x direction, which is characteristic of slow shocks. At the same time, the converging plasma flows towards the reconnection layer from both sides are turned sharply towards the negative z direction immediately downstream of the current sheets (in approximately the $z > -24a$ region). This flow pattern is also consistent with Petschek's model in which the plasmas from upstream of the reconnection layer are accelerated by the slow shocks.

In the following, the magnetic and plasma configurations at $t = 63t_A$ will be used to show that the features of the pair of MHD discontinuities which are located approximately in the region above $z > -24a$ and are associated with the pair of current sheets are consistent with those of slow shocks. Figures 3.6*a* and *b* show the profiles of the simulation quantities across the reconnection layer at $t = 63t_A$ along two straight diagnostic lines at $z = -24a$ and $z = -12a$, respectively. The position of each MHD discontinuity identified in Figure 3.6 is marked by a vertical dashed line.

In Figure 3.6*a*, two MHD discontinuities are found to be associated with the two peaks of current density J_y located at $x \sim \pm 2a$. In Figure 3.6, these two MHD discontinuities are indicated by the two vertical dashed lines labelled with the letters *SS*. It is seen clearly that across these two current sheets from upstream of the reconnection layer, both the magnitude of B_z and magnetic field strength $|B|$ decrease sharply while the plasma density and pressure increase greatly, indicating the existence of two MHD discontinuities. The x component of the plasma velocity v_x converges towards the reconnection layer (v_x is positive for $x < 0$ and negative for $x > 0$), excluding the possibilities of expansion waves or tangential discontinuities. In the reconnection layer v_x is exactly zero. These features are consistent with the properties of slow shocks. Across these two MHD discontinuities, the magnitude of v_z increases to $\sim 0.7V_{A0}$, where V_{A0} is the upstream Alfvén speed.

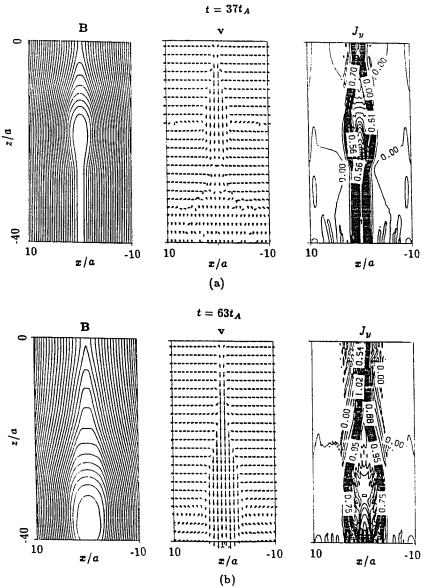

Figure 3.4 Configurations of magnetic field, plasma flow patterns, and current sheet structures at (a) $t = 37t_A$ and (b) $t = 63t_A$ in Case 1. Left panels plot contours of magnetic vector potential, or magnetic field lines; middle panels plot the plasma velocity vectors, the length of which are proportional to the magnitude of the velocity; right panels plot the contours of the y-component of current density J_y.

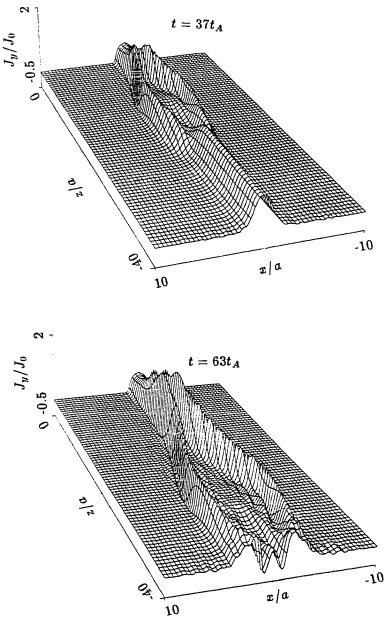

Figure 3.5 Corresponding 3-D profiles of current density J_y in Figure 3.4.

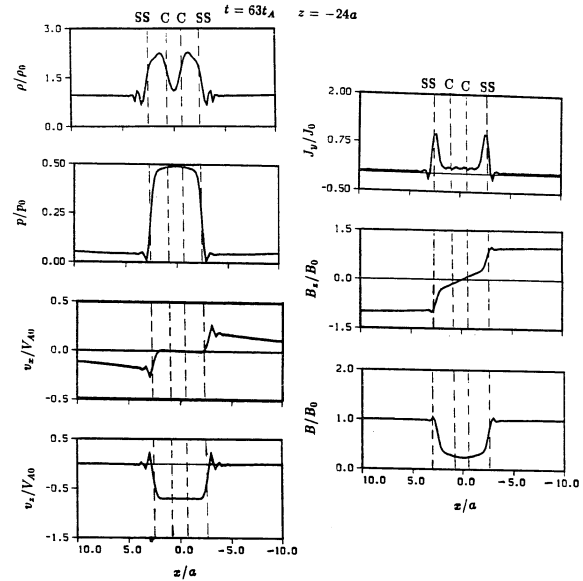

Figure 3.6*a* Profiles of the simulation quantities across the reconnection layer at $z = -24a$ and $t = 63t_A$ in Case 1. The approximate positions of the identified discontinuities are marked by vertical dashed lines in the figure, where SS denotes the slow shock and C denotes the contact discontinuity.

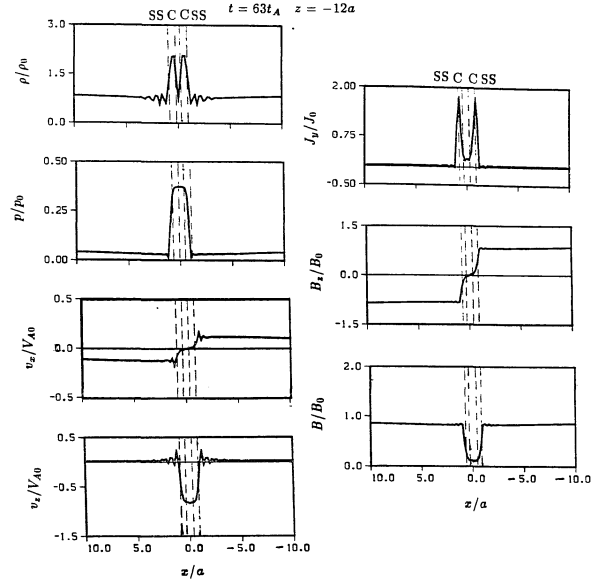

Figure 3.6*b* **Profiles of the simulation quantities across the reconnection layer at $z = -12a$ and $t = 63t_A$ in Case 1. The approximate positions of the identified discontinuities are marked by vertical dashed lines in the figure, where SS denotes the slow shock and C denotes the contact discontinuity.**

The profiles of magnetic and plasma quantities at $z = -12a$, as shown in Figure 3.6*b*, are similar to those at $z = -24a$ (shown in Figure 3.6*a*), except that the separation between the two MHD discontinuities is narrowed.

Note that, as can be seen in Figure 3.6 and later in Figure 3.14, ripples in simulation quantities appear near the two edges of the reconnection layer in the upstream region. These ripples are small numerical fluctuations, not physical waves. Since the amplitudes of these ripples remain small during the whole simulation time, the simulation results should not be affected.

Another common feature revealed in both Figures 3.6*a* and *b* is the appearance of a plasma density minimum at the center of the reconnection layer (at $x = 0$). The plasma densities are seen, first, to increase across the outer pair of slow shocks and, then, to decrease quickly again near the center of the reconnection layer, reaching a local minimum at $x = 0$. Corresponding to this decrease in plasma density, the gas pressure p, the magnetic field B, and v_z change only slightly, while v_x remains nearly zero and B_x is nonzero in the whole recomection layer region. These features are suggestive of the existence of two contact discontinuities between which the plasma density drops. In Figure 3.6 these two MHD discontinuities are marked by two dashed vertical lines labelled with the letter *C*.

A comparison of the current sheet structure at $t = 37t_A$ and $t = 63t_A$ implies that the two identified slow shocks bounding the reconnection layer are propagating into the upstream region of the reconnection layer; as a result, the layer width expands. However, an accurate propagating speed normal to the discontinuity is difficult to calculate in the simulation. As a rough estimation, the half-distance L_d between the two discontinuities was divided by the simulation time to obtain the approximate normal speed averaged over this period. For example, the half-distance between the two discontinuities at $t = 63t_A$ and $z = -24a$ is about $L_d \sim 2a$. Hence, the average normal

speed of discontinuities at $z = -24a$ is about $V_d \sim 2a/63t_A = 0.03V_{A0}$. With this V_d, the upstream plasma flow speed v'_{n1} normal to the discontinuity in the frame of the discontinuity can be estimated, where subscripts n and 1 in v'_{n1} denote the normal component and upstream value, respectively. At $t = 63t_A$ and $z = -24a$, v'_{n1} is estimated to be about $0.26V_{A0}$ (measured from plasma data in Figure 3.6*a*). In obtaining v'_{n1}, the inclination angle ϕ between the discontinuity and negative z direction is taken to be $\phi \sim 10^o$ (measured on the J_y contour plot as the inclination angle of the corresponding current sheet with respect to the negative z-axis). On the other hand, the phase speed V_{sl} of a slow mode wave propagating in the normal direction of the discontinuity is given by

$$V_{sl}^2 = \frac{1}{2}\{V_A^2 + c_s^2 - [(V_A^2 + c_s^2)^2 - 4V_A^2 c_s^2 \cos^2\theta]^{1/2}\} \tag{3.13}$$

where V_A is the Alfvén speed defined by $V_A = B/\sqrt{\mu_0\rho}$, c_s is the sound speed defined by $c_s = \sqrt{\gamma p/\rho}$, and θ is the angle between the magnetic field and the normal of the discontinuity. In our estimation, the angle θ is obtained by $\theta = 90^o - (\alpha - \phi)$, where α is the angle between magnetic field lines at the discontinuity and negative z axis and is calculated by the relation $\alpha = |\tan^{-1}(B_x/B_z)|$. At $t = 63t_A$ and $z = -24a$, since θ is measured to be less than 5^o, V_{sl} upstream of the discontinuities is determined by (3.13) as $V_{sl} < 0.08V_{A0}$ which is much less than v'_{n1}.

Case 2: large β case

In Case 2, all the parameters are the same as in Case 1, except that a large β value is used: $\beta_1 = \beta_2 = 5$. Figure 3.7 shows the profiles of magnetic field, plasma velocity, and current density at two different times for Case 2. Figure 3.8 gives the corresponding 3-D profiles of current density J_y in the x-z plane. From Figure 3.7, it is seen that the general patterns of magnetic reconnection in Case 2 and Case 1 are similar. As in Case 1, the

magnetic bulge formed grows and at the same time propagates outward in the negative z direction. An enhanced plasma speed region is seen to be associated with the magnetic bulge which is bounded by the two bifurcated current sheets. However, the sharp MHD discontinuities in Case 1 are absent in Case 2. Across the whole reconnection layer, magnetic field lines bend and reverse sign smoothly. Correspondingly, the current density J_y in the two current sheets bounding the reconnection layer region is small and the thickness of the current sheets is wider (see Figure 3.8).

Figures 3.9*a* and *b* show the profiles of simulation quantities across the reconnection layer at $t = 64t_A$ and $z = -12a$ and $-24a$ in Case 2, respectively. In Figures 3.9*a* and *b*, it is seen that the discontinuity structure in both magnetic field and plasma quantities is not evident. For example, at $z = -12a$ (Figures 3.9*a*), the peak value of the current density is only about 25% of that in Case 1 at $t = 63t_A$ and $z = -12a$ (Figure 3.6*b*). The plasma density and pressure jump across the current sheets in Case 2 are also much smaller than in Case 1. In Case 2 at $t = 64t_A$ and $z = -12a$ and $-24a$, the pressure and density jump across the current sheets are only about 20% and 10%, respectively, while in Case 1 at $t = 63t_A$, the corresponding profiles of pressure and density at $z = -12a$ and $-24a$ shows an increase of about 6000% for pressure and 100% for density. The magnitude of the plasma speed in the reconnection layer in Case 2 is close to that in Case 1 but it is apparent that the reconnection layer in Case 2 has become wider. On the two sides of the reconnection layer, the plasma flows are converging towards the reconnection layer as in Case 1. Except for a much smoother variation in Case 2, the magnetic field profiles in Case 2 are similar to those in Case 1.

Based on Case 1 and Case 2, it is suggested that in a 2-D symmetric configuration, a pair of slow shocks may develop in the process of reconnection. This pair of slow shocks will bound the reconnection layer region in which another pair of MHD contact discontinuities may exist to account for the large density drop at the center of the

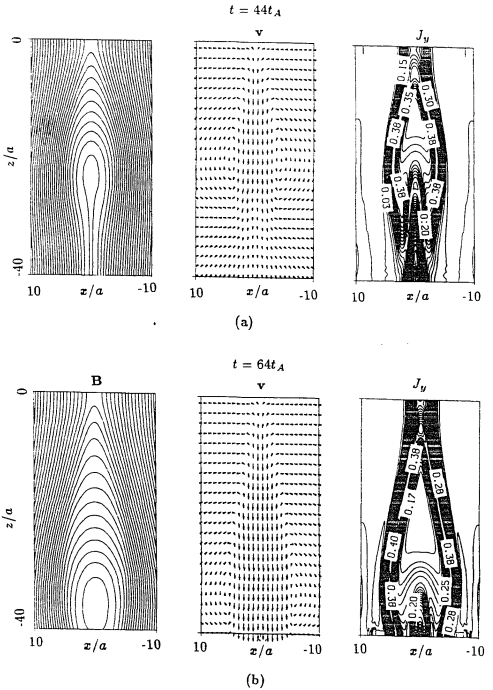

Figure 3.7 Configurations of magnetic field, plasma flow patterns, and current sheet structures at (a) $t = 44t_A$ and (b) $t = 64t_A$ in Case 2.

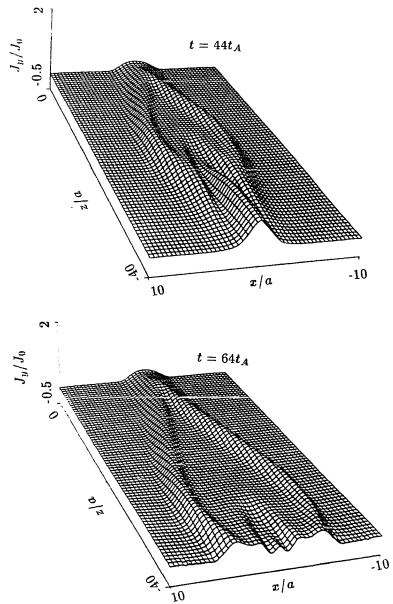

Figure 3.8 Corresponding 3-D profiles of current density J_y in Figure 3.7.

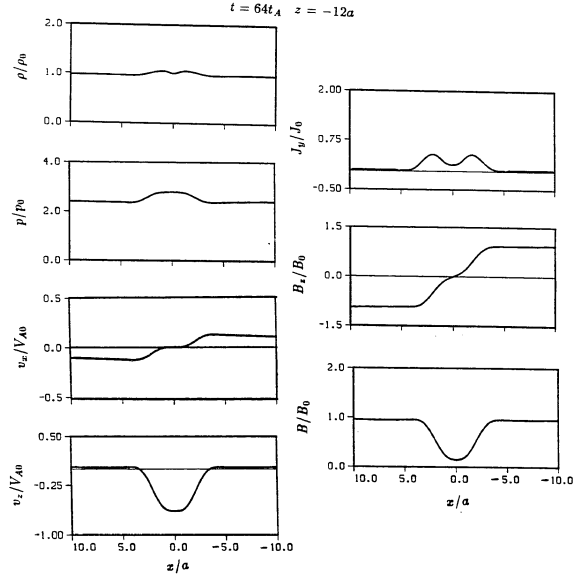

Figure 3.9a Profiles of the simulation quantities across the reconnection layer at $z = -12a$ and $t = 64t_A$ in Case 2.

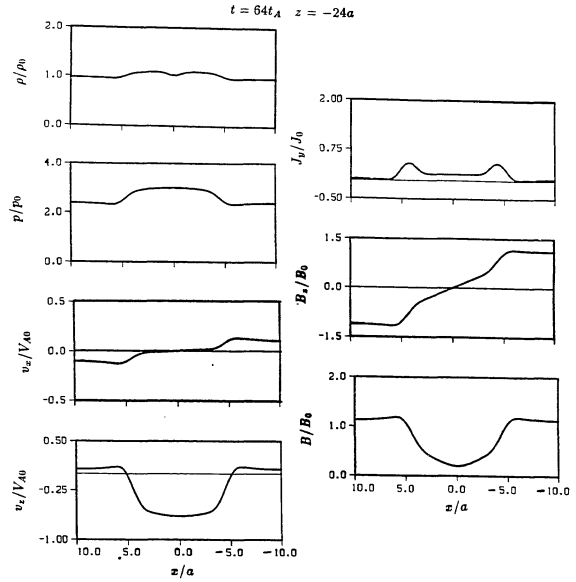

Figure 3.9*b* **Profiles of the simulation quantities across the reconnection layer at $z = -24a$ and $t = 64t_A$ in Case 2.**

reconnection layer. At the initial stage of reconnection, the slow shocks are likely to propagate perpendicular to the shock front into the upstream region and as a result, the width of the reconnection layer will increase. Across the pair of slow shocks from the upstream region, plasmas will be accelerated in the outflow direction by the $\mathbf{j} \times \mathbf{B}$ forces associated with the strong current intensity in the slow shocks. However, in the presence of a large β, sharp MHD discontinuity structures such as slow shocks are unlikely to develop in the reconnection layer. In the earth's magnetotail, the plasma β is low and the plasma and magnetic configuration is more or less symmetric (compared to the dayside situation) with respect to the north-south direction. Therefore, the formation of slow shocks is expected to be a common feature in the tail reconnection. The existence of a pair of slow shocks attached to the reconnection layer was first suggested by *Petschek* [1964]. Later, in symmetric MHD simulations, the slow shock structures have been observed in driven reconnection as well as spontaneous reconnection [e.g., *Sato*, 1979; *Fu and Lee*, 1986; *Scholer*, 1989].

3.3.2 Asymmetric magnetic reconnection

In subsection 3.3.1, it has been demonstrated that 2-D symmetric magnetic reconnection is characterized by the development of a pair of slow shocks bounding the reconnection layer. In this section, the properties of magnetic reconnections in an asymmetric configuration are investigated.

Case 3: asymmetry in the magnetic field

Case 3 studied the effect of asymmetry in the magnetic field on the reconnection process. In Case 3, the plasma density on both sides of the current sheet is identical while magnetic field strength B_{10} on Side 1 (right side of the simulation box) is increased

to $1.5B_{20}$ (recall that B_{20} is used as the normalization unit). On Side 1 with high magnetic field strength, $\beta_1 = 0.1$ is used and the initial pressure balance then requires that $\beta_2 = 1.5$ on Side 2 (see (3.10)). Since, as will be shown below, the magnetic bulge resulting from reconnection in Case 3 is larger on Side 2 (smaller magnetic field strength side), x_0 in (3.8) is set to $x_0 = -4a$ or, equivalently, the initial current sheet is moved to the right of the center line of the simulation box at $x = 0$.

Figure 3.10 shows the magnetic field and plasma patterns at $t = 47t_A$ and Figure 3.11 shows the corresponding 3-D profile of J_y in the x-z plane. The magnetic bulge on Side 2 (left side) is larger than that on Side 1, as can be determined by the larger curvatures of magnetic field lines on Side 2. The asymmetry in the magnetic bulge is also reflected in the plasma velocity pattern. As can be seen in Figure 3.10, the right boundary of the enhanced plasma speed region is almost parallel to the z-axis while the left boundary shows a bulged shape. Associated with the enhanced plasma flow speed region on Side 2 is a vortex flow pattern. The reconnection layer can be identified as the region bounded by the two current sheets which show a larger inclination angle with respect to the z-axis on Side 2 corresponding to the larger magnetic bulge on Side 2. In the plasma density distribution, a thin layer of high plasma density appears near the right boundary of the reconnection layer. Within the reconnection layer, the plasma thermal pressure is enhanced. It is seen that in the region approximately above $z > -15a$, the magnetic field lines reverse sign across the left branch of the current sheet. It will be shown below that this portion of the left branch of the current sheet may correspond to an intermediate MHD shock.

Figures 3.12*a* and *b* show the profiles of magnetic and plasma quantities across the reconnection layer at $t = 47t_A$ and $z = -12a$ and $z = -24a$, respectively.

In Figure 3.12*a*, the two current density peaks indicate the presence of two MHD discontinuities at $x \sim -2.5a$ and $x \sim -6a$. The two current density peaks also mark the

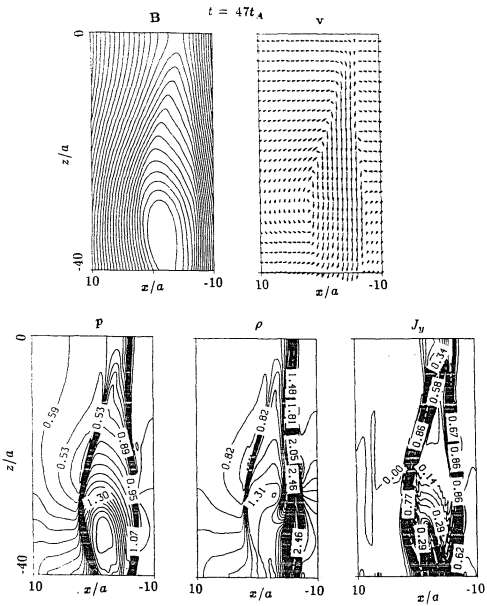

Figure 3.10 Configuration of magnetic field (upper left panel), plasma flow patterns (upper right panel), contours of pressure (lower left panel), contours of plasma density (lower middle panel), and contours of current density J_y at $t = 47t_A$ in Case 3.

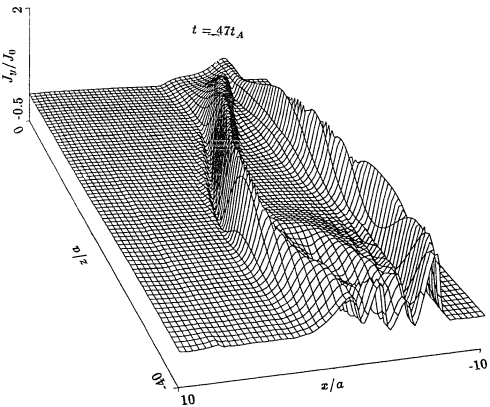

Figure 3.11 Corresponding 3-D profiles of current density J_y in Figure 3.10.

region of the reconnection layer at $z = -12a$. Across the right MHD discontinuity at $x \sim -6a$ from upstream of the reconnection layer, magnetic field strength $|B|$ decreases (but B_z does not reverse sign) while both plasma density ρ and thermal pressure p increases. Upstream of the reconnection layer on Side 1, the x component of plasma velocity, v_x, which is almost in the discontinuity normal direction, is positive, i.e., towards the reconnection layer. Hence, the MHD discontinuity corresponding to the right branch of the current sheet at $x \sim -6a$ may be a slow shock. However, the MHD discontinuity corresponding to the left branch of the current sheet at $x \sim -2.5a$ cannot be identified as a slow shock since B_z reverses its sign across the discontinuity, while in a slow shock the tangential component of the magnetic field at most is switched off (or becomes zero) in the downstream region. There are two MHD discontinuities across which the tangential component of the magnetic field can reverse its sign: the rotational discontinuity and the intermediate shock. However, since downstream of this discontinuity both ρ and p are increased, it cannot be a rotational discontinuity either. Hence, the MHD discontinuity at $x \sim -2.5a$ may correspond to an intermediate shock. It is necessary to check the upstream normal flow velocity v'_{n1} in the frame of the discontinuity to see if it is super-Alfvénic, as this is a required condition for the formation of an intermediate shock. The phase velocity of Alfvén waves propagating in the normal direction of the discontinuity is given by

$$V_{An}^2 = V_A^2 \cos\theta, \tag{3.14}$$

where θ and V_A are defined in (3.13). By the same method used in Case 1, the following characteristic parameters are obtained for the left intermediate shock at $t = 47t_A$ and $z = -12a$: $V_d \sim 0.04V_{A0}$, $\phi \sim 20^o$, $\alpha \sim 27^o$. The upstream values of normal flow speed, magnetic field strength B, and plasma density are measured directly in Figure 3.12a. Finally, we obtain $v'_{n1} \sim 0.4V_{A0}$ and $V_{An} \sim 0.2V_{A0}$. Hence, the upstream

Alfvén Mach number M_{An1} in the frame of discontinuity is about 2, consistent with the super-Alfvénic condition for the formation of intermediate shocks.

At $z = -24a$, as shown in Figure 3.12*b*, the right branch of the current sheet now located at $x \sim -7a$ still corresponds to a slow shock. However, the intermediate shock corresponding to the left branch of the current sheet at $z = -12a$ is now replaced by a slow shock located at $x \sim 0.7a$.

The appearance of an intermediate shock in Case 3 is a feature not observed in the symmetric cases (Case 1 and Case 2). Case 3 shows that closer to the reconnection point (X point), the reconnection layer is bounded by a slow shock on the side with a larger magnetic field strength (Side 1) and an intermediate shock on the side with a weaker magnetic field strength (Side 2), while farther away from the X point, the reconnection layer on both sides is bounded by two slow shocks. This mixed state of slow shock and intermediate shock along the left boundary of the reconnection layer exists throughout the simulation run. Furthermore, the two contact discontinuities associated with the density ρ drop within the reconnection layer identified in the symmetric case still exist in Case 3 in the reconnection layer, except that the left one corresponds to a much smaller density drop than the right one. As in the symmetric case, a region of enhanced plasma flow speed appears in the reconnection layer of Case 3. However, in Case 3, the enhanced plasma flow speed region shifts to Side 1 with larger magnetic field strength (in fact, at $x = -12a$ as shown in Figure 3.12*a*, the whole enhanced $|v_z|$ region is almost all in the $B_z > 0$ region).

Case 4: Small asymmetry in plasma density

In Case 4, magnetic field and plasma β values on Side 1 and Side 2 are symmetric: $B_{10}/B_{20} = 1$ and $\beta_1 = \beta_2 = 0.1$; a small asymmetry in plasma densities on Side 1 and

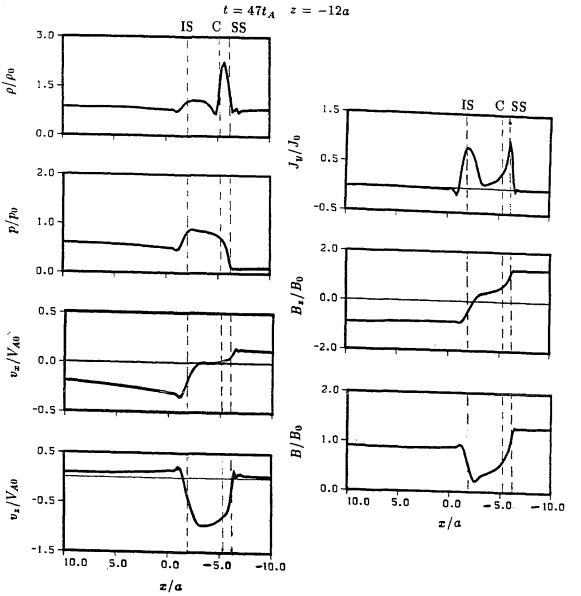

Figure 3.12*a* Profiles of the simulation quantities across the reconnection layer at $z = -12a$ and $t = 47t_A$ in Case 3. The position of the intermediate shock is marked by the vertical dashed line labelled IS.

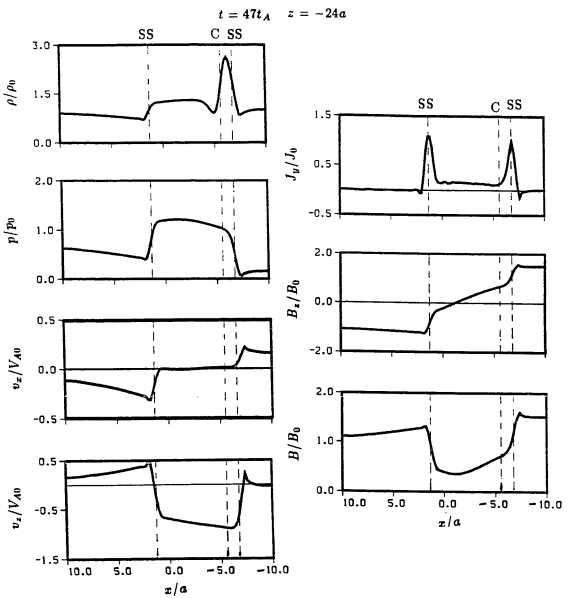

Figure 3.12*b* Profiles of the simulation quantities across the reconnection layer at $z = -24a$ and $t = 47t_A$ in Case 3.

Side 2 is assumed: $\rho_{02}/\rho_{01} = 2$.

Figure 3.13 shows the magnetic field configuration, flow pattern, and current sheet structure at $t = 50t_A$ for Case 4. One apparent feature of magnetic field configuration which is different from that in the symmetric case is that the bending of magnetic field lines near the left boundary of the reconnection layer is much larger than that near the right boundary. It will be shown below that this large bending of magnetic field lines corresponds to a switch-off slow shock downstream of which the tangential component of the magnetic field is zero (or switched off).

Figure 3.14 shows the profiles of simulation quantities at $z = -24a$ and $t = 50t_A$. A careful examination of Figure 3.14 shows that the two current density peaks located at $x \sim 0.5a$ and $-4a$ correspond to two slow shocks. In particular, it can be seen from the B_z profile in Figure 3.14 that downstream of the left slow shock B_z is zero. This suggests that this discontinuity may be a switch-off slow shock. In the reconnection layer, the two contact discontinuities can be identified near the density minimum and are marked in Figure 3.14 by two vertical dashed lines labelled with the letter *C*. In the reconnection layer at $z = -24a$, it is seen that plasma is accelerated to a speed of about V_{A0} in the negative z direction. The profiles of simulation quantities at several other locations above $z > -24a$ were also examined. Qualitatively, the structure of the reconnection layer was similar to those revealed at $z = -24a$ (shown in Figure 3.14).

Hence, Case 4 suggests that with a small asymmetry in plasma density, the reconnection layer structure resembles qualitatively the one in the symmetric case except that the bending of magnetic field lines across the slow shock on the side with a larger plasma density (Side 2 in Case 4) tends to be stronger, corresponding to a larger decrease in the tangential component of the magnetic field downstream of the discontinuity. It will be shown in the next simulation case, Case 5, that when the plasma density asymmetry on the two sides becomes even larger, the bending of magnetic field lines across the

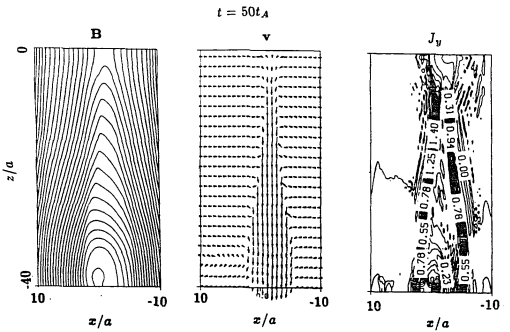

Figure 3.13 Configuration of magnetic field (left panel), plasma flow patterns (middle panel), current sheet structure (right panel) at $t = 50t_A$ in Case 4.

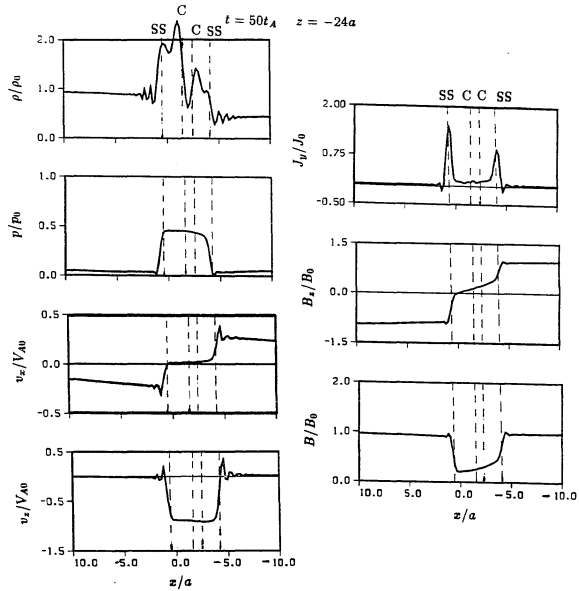

Figure 3.14 Profiles of the simulation quantities across the reconnection layer at $z = -24a$ and $t = 50t_A$ in Case 4.

discontinuity on the side with greater plasma density is so large that the magnetic field virtually reverses its sign downstream of the discontinuity, suggesting the existence of an intermediate shock there.

Case 5: large asymmetry in plasma density

In Case 5, the asymmetry in plasma density is increased to $\rho_{02}/\rho_{01} = 10$ while the rest of the parameters are the same as in Case 4.

Figure 3.15*a* shows the magnetic field configuration, plasma flow pattern, and current sheet structure at $t = 40t_A$ for Case 5. Figure 3.15*b* is the corresponding 3-D profile of current density J_y at $t = 40t_A$.

From Figure 3.15, it is seen that one of the features in Case 5 is that the intensities of the two branches of the current sheets are in sharp contrast in the region above $z > -30a$. The right branch of the current sheet bounding the reconnection layer is so weak that it is barely identifiable while the left one is strong. As a result, the jump of the tangential component of the magnetic field is small across the right branch of the current sheet but is large across the left branch. In fact, as can be seen from the magnetic field configuration in Figure 3.15, magnetic field lines reverse sign across the left branch of the current sheet in the region approximately above $z > -24a$. However, it is interesting to note that the magnitude of the plasma velocity in the reconnection layer does not exhibit a noticeable asymmetry in the x direction. Plasma across the left and right branches of the current sheet is accelerated by the $\mathbf{j} \times \mathbf{B}$ to high speed of comparable magnitudes despite the large difference in the intensities of the two branches of the current sheet. This fact is not surprising since the plasma density on the right side of the reconnection layer is an order of magnitude smaller than that on the left

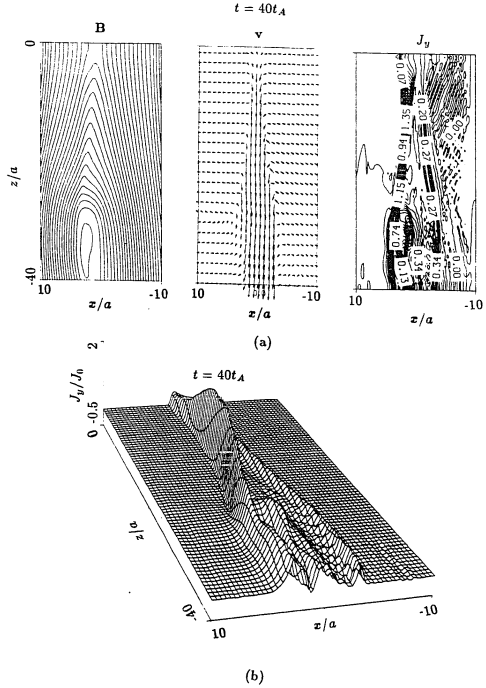

Figure 3.15 (a) Configuration of magnetic field (left panel), plasma flow patterns (middle panel), current sheet structure (right panel) at $t = 50t_A$ in Case 5; (b) the corresponding 3-D profile of current density J_y.

side. Hence, the force needed to accelerate plasma to the same high speed on the right side is also smaller.

Figure 3.16 shows the profiles of simulation quantities across the reconnection layer at $z = -18a$ and $t = 40t_A$ for Case 5. First, from the profile of the current density J_y, it is seen that peak value of the left branch of the current sheet at $z = -18a$ is much larger than that of the right branch of current sheet. In the figure, the two J_y peaks are located at $x \sim 0.4a$ and $-0.3a$, respectively. The peak values of J_y are about $2J_0$ for the right peak and $0.3J_0$ for the left one. This indicates that the jump in the tangential component of the magnetic field is much larger across the left branch of the current sheet than across the right one. On further inspection, the behavior of the magnetic field and plasma quantities implies that the left branch of the current sheet may correspond to an intermediate shock while the right one is a weak slow shock. In the present case with a large density asymmetry, two major features which are in contrast to those in the Case 4 with a small density asymmetry are: (1) the magnetic field jump in tangential component is much larger on the left side (large density side) than on the right side (small density side) of the reconnection layer and (2) the right density bump in the reconnection layer is now small compared to the left one. In Case 5, the jump in the tangential magnetic field component across the left boundary of the reconnection layer (or the left branch of the current sheet) is so large that the tangential component of the magnetic field virtually reverses its sign from upstream to downstream region of the discontinuity, implying an intermediate shock, while in Case 4, the tangential component of magnetic field is only nearly switched off across the left branch of the current sheet, which may correspond to a switch-off shock. Furthermore, in Case 5, though the left contact discontinuity associated with the left large bump in the plasma density profile can still be identified in the reconnection layer, the corresponding right

contact discontinuity present in Case 4 is less obvious due to the small density variation associated with the right plasma density bump.

Approximately in the $z > -24a$ region, the profiles of magnetic field and plasma quantities across the reconnection layer at different z locations (not shown here) also show similar patterns to those in Figure 3.16. Therefore, it may be concluded that in the presence of a large plasma density asymmetry, the reconnection layer is likely to be bounded by an intermediate shock on the large plasma density side and a weak slow shock on the small plasma density side, while in the reconnection layer itself, only one contact discontinuity may be present.

Case 6 and Case 7: asymmetry in both magnetic field and plasma density

In Case 6 and Case 7, the ratio of the initial plasma densities on the two sides is still $\rho_{10}/\rho_{20} = 0.1$ but the asymmetry in the magnetic field is $B_{10}/B_{20} = 1.5$ and 3, respectively. On Side 1 the β value is fixed to $\beta_1 = 0.1$. Hence, an increase of magnetic field strength on Side 2 in Case 6 and Case 7 requires the β values on Side 2 to be increased to $\beta_2 = 1.5$ and 9, respectively. Note that Case 7 is a high β case with $\beta_2 = 9$ on Side 2.

Figure 3.17*a* shows the magnetic field configuration, plasma flow pattern, and current sheet structure at $t = 44t_A$ for Case 6. Figure 3.17*b* is the corresponding 3-D profile of current density J_y at $t = 44t_A$. From Figure 3.17, it is seen that, as in Case 3 which only has asymmetry in the magnetic field ($B_{01}/B_{02} = 1.5$), the magnetic bulge resulting from reconnection is larger on the low magnetic field side (Side 2) than on the high magnetic field side (Side 1). This asymmetry in magnetic bulge seems to be a common feature in a reconnection configuration in which magnetic field strength on two sides is not equal. The plasma flow pattern in Case 6 (at $t = 44t_A$) is also similar

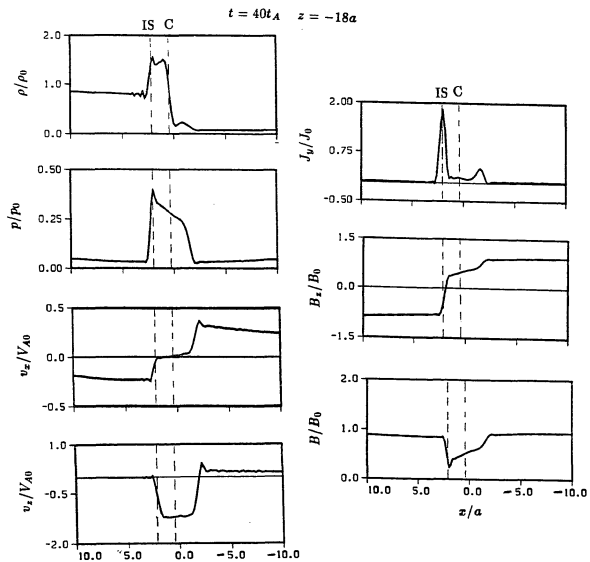

Figure 3.16 Profiles of the simulation quantities across the reconnection layer at $z = -18a$ and $t = 40t_A$ in Case 5.

to that in Case 3. However, unlike Case 3, Case 6 also has an asymmetry in plasma densities on the two sides. As a result, as can be seen from Figure 3.17*b*, in Case 6 the current density in the right branch of the current sheet is much weaker than that in the left branch. This same asymmetry in the left and right branches of the current sheet is also found in Case 5, which has only asymmetry in plasma densities on both side. In fact, a detailed diagnostic shows that the right branch of the current sheet is so weak that the magnetic field jump corresponding to it is almost negligible.

Figure 3.18 shows the magnetic field and plasma quantities across the reconnection layer at $z = -18a$. In Figure 3.18, it is seen that the reconnection layer is bounded on the left side (low magnetic field and high plasma density side) by an intermediate shock and on the right side by a very weak and almost unidentifiable slow shock. In this case, the large density drop in the reconnection layer cannot be identified as a contact discontinuity due to the existence of a finite normal flow ($v_x \neq 0$).

Figure 3.19 shows the magnetic field configuration, plasma flow pattern, and current sheet structure at $t = 42t_A$ for Case 7. The most apparent feature noted in Figure 3.19*a* is that the magnetic bulge associated with the reconnection layer is almost exclusively on the low magnetic field side (Side 2) while on the high magnetic field side (Side 1) of the reconnection layer the magnetic field lines are nearly straight lines. In the reconnection layer the plasma is seen to be accelerated to very high speed (higher than that in any of the previous cases, as will be shown in the following Figure 3.20). The high speed of plasma in the reconnection layer may be due to the strong magnetic field on one side of the reconnection layer.

The magnetic field reversal region in Case 7 is approximately in the $z > -24a$ region. As an example, Figure 3.20 shows the plasma and magnetic field quantities across the field reversal region or reconnection layer at $t = 42t_A$ and $z = -12a$. From Figure 3.20, it is seen that except for the large drops in plasma density and pressure in

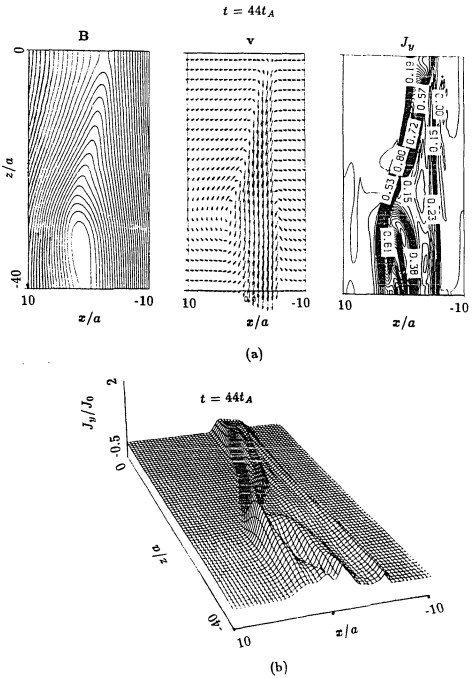

Figure 3.17 (a) Configuration of magnetic field (left panel), plasma flow patterns (middle panel), current sheet structure (right panel) at $t = 44t_A$ in Case 6; (b) the corresponding 3-D profile of current density J_y.

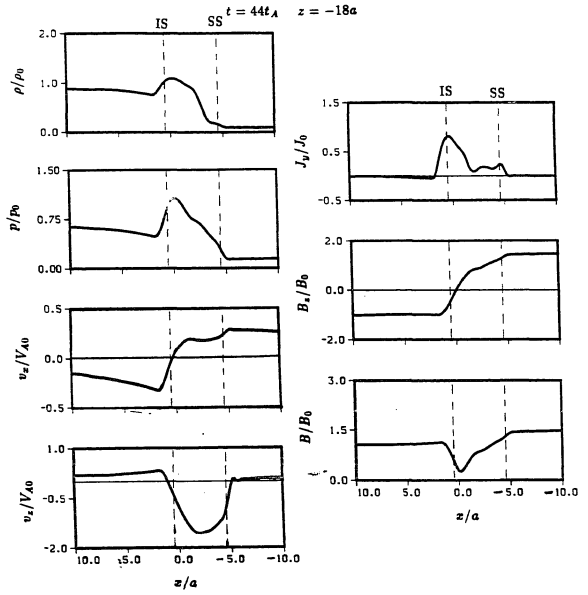

Figure 3.18 Profiles of the simulation quantities across the reconnection layer at $z = -18a$ and $t = 44t_A$ in Case 6.

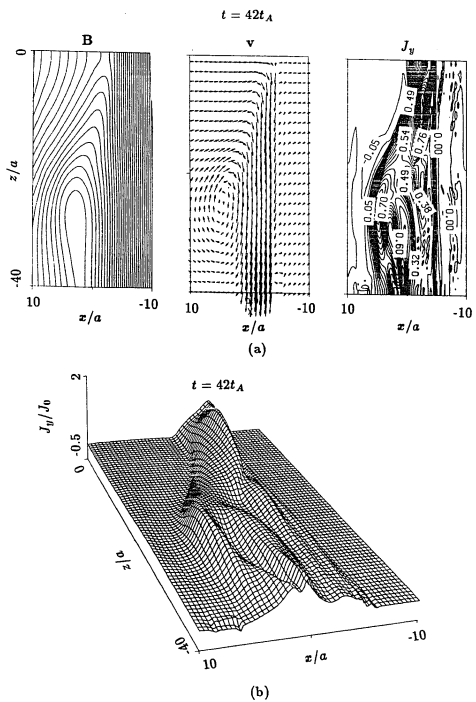

Figure 3.19 (a) Configuration of magnetic field (left panel), plasma flow patterns (middle panel), current sheet structure (right panel) at $t = 42t_A$ in Case 7; (b) the corresponding 3-D profile of current density J_y.

the reconnection layer, the transition of each quantity from Side 2 to Side 1 is smooth, or the discontinuity structure in the reconnection layer is very weak. Note that from Case 5 and Case 6, it is already seen that the discontinuity is weak on the side with a very low plasma density. Therefore, the weak discontinuity structure on Side 1 (right side) in Case 7 is an expected result. On the other hand, as is shown in the symmetric case (Case 2), the high β value tends to smooth out the sharp jumps in plasma and magnetic field quantities. In Case 7, the β value on the left side is very high ($\beta_2 = 9$) and, consistent with Case 2, the discontinuity structure is seen to be weak. One another feature revealed in Figure 3.20 is the high plasma speed in the reconnection layer, which reaches $|v_x| \sim 3V_{A0}$ at $x \sim -3a$, the highest in all simulation cases. Furthermore, most of this high-speed plasma jet is on the side with $B_z > 0$.

Both Case 5 and Case 6 are cases with a large plasma density ratio. The reconnection layer in both cases is found to be bounded by an intermediate shock on the high plasma density side and a weak slow shock on the low plasma density side. When the magnetic field strength on the low plasma density side is increased, as in Case 6, the slow shock on that side becomes even weaker while the jump in plasma and magnetic field quantities associated with the intermediate shock on the other side becomes smoother. If the magnetic field strength on the low plasma density side is further increased as in Case 7, the variation of plasma and magnetic field quantities across the reconnection layer is so smooth that discontinuity structures within the layer are difficult to identify.

3.4 Application to the Dayside Magnetopause

The earth's dayside magnetopause is a boundary which separates the magnetosheath (the shocked solar wind region) from the magnetospheric region (the geomagnetic field

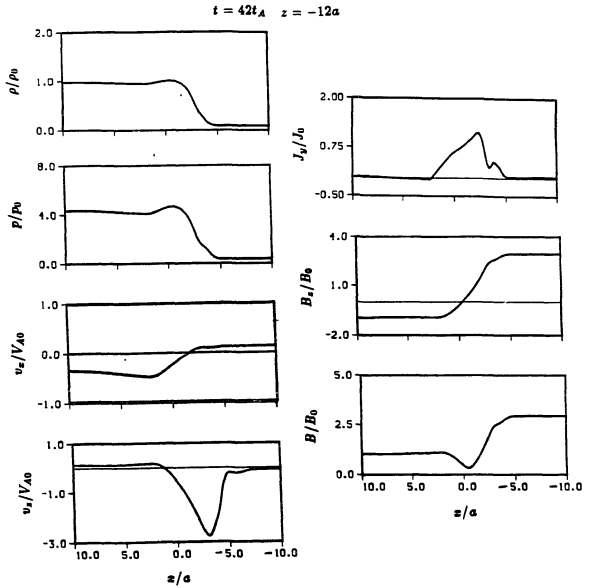

Figure 3.20 Profiles of the simulation quantities across the reconnection layer at $z = -12a$ and $t = 42t_A$ in Case 7.

region with contained plasma). On both sides of the magnetopause, plasma is magnetized. A noticeable asymmetry in the plasma and magnetic field parameters exists between the two sides. First, the plasma density is usually high in the magnetosheath and low in the magnetosphere. The plasma number density in the magnetosheath is on the order of 10 cm^{-3}, typical of many observed magnetopause crossings. Variations in this parameter may occur by up to an order of magnitude. For example, during storm times the density may be as high as 100 cm^{-3} [e.g., *Paschmann et al.*, 1986] and occasionally values as low as 1 cm^{-3} have been seen [e.g., *Gosling et al.*, 1982]. The ratio of the plasma density in the magnetosheath to that in the magnetosphere is typically 10:1. Deviations from the average number density in the magnetosphere may also occur, e.g., as the result of strong compression of the magnetosphere. Second, the magnetic field strength is usually higher on the magnetospheric side than on the magnetosheath side. The strong magnetic field strength on the magnetospheric side leads to a low plasma β value while on the magnetosheath side the plasma β value is often high or the plasma pressure is dominant over the magnetic pressure on the magnetosheath side.

3.4.1 Simulation cases

In these simulations, Petschek's model has been confirmed in the symmetric cases, Case 1 and Case 2, in which a pair of slow shocks is observed to bound the reconnection layer. However, Case 1 and Case 2 cannot be applied to the dayside magnetopause because they assumed equal plasma density on both sides. In simulation cases Case 5, Case 6, and Case 7, a large asymmetry in plasma density is assumed: $\rho_{10}/\rho_{20} = 0.1$. Hence, Case 5, Case 6, and Case 7 may be considered as suitable for the dayside magnetic reconnection process with the magnetosheath on Side 2 (high plasma density side) and the magnetosphere on Side 1 of the simulation configuration. In the following, the

reconnection layer structure observed in these three cases (Case 5, Case 6, and Case 7) will be re-examined in relation to the dayside magnetopause. For convenience in the discussion below, Side 1 (low plasma density side) in the simulation will be called the magnetospheric side and Side 2 (high plasma density side) the magnetosheath side. Note in all these three cases, the plasma β values on Side 1 are low ($\beta_1 = 0.1$ in all three cases) which is also typical of the magnetospheric side. The only difference in Case 5, Case 6, and Case 7 is the ratio of the magnetic field strength or the plasma β value in the magnetosheath.

In Case 5, the magnetic field strength on both sides of the magnetopause is equal. Hence, Case 5 corresponds to a low plasma β case (in terms of the β value in the magnetosheath). From Figure 3.15 and 3.16, it can be seen that the reconnection layer in Case 5 is bounded by an intermediate shock on the magnetosheath side and a weak slow shock on the magnetospheric side. The current sheet corresponding to the intermediate shock may be identified as the magnetopause, since the direction of magnetic field changes from a southward to northward direction (positive z direction in the simulation) in going from the magnetosheath to the magnetosphere.

We now closely examine the reconnection layer structure of Case 5 at $z = -18a$ and $t = 40t_A$, as shown in Figure 3.16. It is seen that the tangential plasma speed $|v_z|$ in the reconnection layer is enhanced to a value of about $1.3V_{As}$, where V_{As} denotes here the Alfvén speed on the magnetosheath side (recall that the normalization unit of velocity in the simulation is the Alfvén speed on Side 2 or the magnetosheath side). In Case 5, the Alfvén speed on the magnetospheric side is $V_{Am} \sim 3V_{As}$. Hence, the value of the plasma speed in the reconnection layer is greater than the magnetosheath Alfvén speed but less than the magnetospheric-side Alfvén speed. Also note that the enhanced $|v_z|$ region occurs almost exclusively between the intermediate shock, or magnetopause, and the weak slow shock. This region may be identified as the boundary layer of

the dayside magnetopause. The boundary layer is a region of plasma inside of or adjacent to the magnetopause that has properties unlike those observed either in the magnetosheath or magnetosphere. The converging flow of plasma in Case 5, as shown in Figure 3.16, indicates that the plasma in the boundary layer (the reconnection layer in this case) comes from both the magnetosheath side and the magnetospheric-side (v_x is negative, or antisunward, on the magnetosheath side and positive, or sunward, on the magnetospheric side). From Figure 3.16, it can be further seen that since the plasma pressure p varies little in this boundary layer while plasma density ρ is high in the left half of the boundary layer but low in the right half, the plasma in the boundary layer is made up of high-temperature plasma on the right side and low temperature plasma on the left side. One MHD discontinuity that can be identified in the reconnection layer of Case 5 is the contact discontinuity as shown in Figure 3.16. This contact discontinuity separates the high-temperature plasma from low-temperature plasma in the reconnection layer. However, in a collisionless plasma, as argued by *Barnes* [1971] and *Rijnbeek et al.* [1988], the contact discontinuity is unlikely to be found because the magnetic field component parallel to the plasma density gradient allows rapid diffusion of plasma along the gradient. Hence, in the real reconnection layer at the magnetopause, the high-temperature and low-temperature plasma may be in a mixed state. Another feature revealed in Figure 3.16 is the reduced magnetic field strength in the reconnection layer to maintain the approximate total pressure balance since the plasma pressure is enhanced in the reconnection layer. In interpreting one observational example of dayside reconnection, *Rijnbeek et al.* [1988] have used the reduced magnetic field strength in the identified reconnection layer as an indicator of slow shocks. However, as was seen in Case 5, the reduced magnetic field strength can be also associated with an intermediate shock.

In Case 6, the magnetic field strength B_m on the magnetospheric side is increased to $1.5B_s$, where B_s is the magnetic field strength on the magnetosheath side. Case 6 is a medium plasma β case ($\beta_2 = 1.5$ on the magnetosheath side). As in the low β case, Case 5, the reconnection layer in Case 6 is bounded by an intermediate shock on the magnetosheath side and a very weak slow shock on the magnetospheric side. Again, the magnetopause and the boundary layer can be identified as the current sheet associated with the intermediate shock and the enhanced $|v_z|$ region, respectively. As in Case 5, the enhanced plasma speed in the reconnection layer is greater than the magnetosheath side Alfvén speed but less than the magnetospheric side Alfvén speed ($|v_z|$ reaches a maximum value of about $1.7V_{As}$ at $x \sim 2a$ in Figure 3.18 while the Alfvén speed on the magnetospheric side $V_{Am} \sim 4.7V_{As}$ in Case 6). The reduction of magnetic field strength in the reconnection layer is large on the magnetosheath side but small on the magnetospheric side, corresponding to a weak slow shock. The major differences between the medium β case, Case 6, and small β case, Case 5, are that: (1) the thickness of the current sheet or the discontinuity corresponding the intermediate shock or magnetopause increases in Case 6, (2) the slow shock bounding the magnetospheric edge of the reconnection layer becomes even weaker in Case 6, (3) the contact discontinuity structure clearly identifiable in the reconnection layer of Case 5 is less evident in Case 6, and (4) the relative jump in plasma pressure p and density ρ across the intermediate shock is smaller in Case 6 than in Case 5.

As the plasma β in the magnetosheath is further increased, as demonstrated in Case 7 (Figures 3.19 and 3.20), discontinuity structures are difficult to identify in the dayside reconnection layer. The reconnection layer in Case 7 can be considered simply as corresponding to a nonlinear structure across which, from magnetosheath side, the magnetic field reverses its sign and increases to the magnetospheric value while both the plasma density and pressure decrease. The magnetopause in Case 7 corresponds

almost to the entire reconnection layer region. In the reconnection layer of Case 7, the plasma speed is also enhanced: $|v_z|$ reaches a maximum value of about $3V_{As}$ at $x \sim -3a$ in Figure 3.20. This maximum value of $|v_z|$ in the reconnection layer again is greater than the magnetosheath Alfvén speed V_{As} but less than the magnetospheric side Alfvén speed V_{Am}, which in Case 7 is about $9.5V_{As}$. Case 7 indicates that in the presence of a large magnetosheath β value or a large ratio of magnetic field strengths on both sides of the magnetopause, sharp discontinuity structures are unlikely to be found in the dayside reconnection layer.

The simulation cases discussed above indicate that: (1) for a low or medium plasma β in the magnetosheath, the reconnection layer is bounded by an intermediate shock (the magnetopause) on the magnetosheath side and a weak slow shock on the magnetospheric side, (2) for a large plasma β in the magnetosheath, sharp MHD discontinuity structures in the reconnection layer tend to be absent, (3) in all cases, the plasma speed in the reconnection layer is always enhanced and is greater than the Alfvén speed in the magnetosheath but smaller than the Alfvén speed in the magnetosphere, (4) the magnetic field strength in the reconnection layer is always reduced from the upstream value, and (5) in case of a low plasma β in the magnetosheath, a contact discontinuity is present in the reconnection layer.

3.4.2 Evolution of the dayside reconnection layer

In this subsection, we will provide a qualitative explanation of the simulation results on the dayside reconnection layer structures.

In the absence of magnetic reconnection, the dayside magnetopause may be considered as a tangential discontinuity. With the onset of magnetic reconnection, this tangential discontinuity may evolve into several other discontinuities constituting the

reconnection layer. One basic feature of magnetic reconnection is that the magnetic field direction reverses from one side to the other. In a symmetric case, *Petschek* [1964] has assumed that this field reversal can be achieved by two pairs of slow shocks bounding the reconnection layer, since the slow shock has the property of reducing the magnetic field component tangential to the shock front downstream of the slow shock. In Petschek's model, the outflow plasma downstream of the pair of nearly switch-off slow shocks flows with the upstream Alfvén velocity (Alfvén velocity in the inflow region) [e.g., *Vasyliunas*, 1975]. However, at the dayside magnetopause, the asymmetry in plasma and magnetic field parameters on the two sides of the magnetopause leads to largely different Alfvén speeds on two sides. The Alfvén speed V_{As} on the magnetosheath side is much smaller than the Alfvén speed V_{Am} on the magnetospheric side, due to the small plasma number density n_m and strong magnetic field strength B_m on the magnetospheric side and large plasma number density n_s and weak magnetic field strength B_s on the magnetosheath side. For example, if the typical ratios at the dayside magnetopause are taken to be $n_s/n_m \sim 10$ and $B_m/B_s \sim 3$, then $V_{Am}/V_{As} \sim 10$. This large difference in Alfvén velocities may lead to reconnection layers with a different discontinuity structure from that in Petschek's symmetric model. In the following, we will suggest a possible evolution pattern for the shock structures bounding the reconnection layer at the dayside magnetopause before reaching the quasi-steady state by assuming that the pairs of slow shocks in Petschek's model form at a very early stage of the reconnection.

The suggested evolution of the shock structure is illustrated in Figure 3.21. In Figure 3.21, SS denotes slow shock, IS denotes intermediate shock, and X denotes the reconnection point (or X point). Illustrated in the figure are the reconnection layer configurations at three time instances $t = t_1$, t_2, and t_3, where v_s and v_m are the plasma speeds in the reconnection layer downstream of the MHD shocks on the magnetosheath

and magnetospheric sides, respectively, with the superscripts 1, 2, and 3 corresponding to three different time instances. Plotted in Figure 3.21 is the upper half of the whole reconnection configuration. Suppose a pair of slow shocks (nearly switch-off) is formed immediately after the reconnection at $t = t_1$. Downstream of this pair of slow shocks, the plasmas will be flowing out with approximately the corresponding upstream Alfvén velocities: $v_s^{(1)} \sim V_{As}$ and $v_m^{(1)} \sim V_{Am}$. Since V_{Am} is much greater than V_{As} as pointed out above, there will be at $t = t_1$ a large velocity shear in the reconnection layer. Plasmas downstream of the slow shock on the magnetospheric side (right side in the figure) will move much faster than do plasmas downstream of the other slow shock. Since the reconnected field lines are convected out along with the out-flowing plasmas, the velocity shear in the reconnection layer will reduce the jump in the tangential magnetic field component across the discontinuity on the right side but increase it across the discontinuity on the left side. At this stage ($t = t_2$ in Figure 3.21), the discontinuity on the right side may become a weak slow shock while the discontinuity on the left side corresponds to a strong slow shock (the strength of the slow shock is defined here in terms of the magnitude of the jump in the tangential magnetic component across the slow shock). Hence, the current density $\mathbf{j}$ in the current sheets associated with the right and left shock waves will decrease and increase, respectively. As a result, the plasma speed decreases downstream of the right slow shock (weak slow shock) and increases downstream of the left slow shock (strong slow shock), since the plasma acceleration in the reconnection layer is mainly due to the Lorentz force ($\mathbf{j} \times \mathbf{B}$ force) associated with the shock waves. Eventually, at $t = t_3$, the plasma speed in the reconnection layer will become uniform, namely, $v_s^{(3)} = v_m^{(3)}$ while the left discontinuity will evolved into an intermediate shock and the right discontinuity into an even weaker slow shock. In addition, $v_s^{(3)}$ and $v_m^{(3)}$ will both be greater than V_{As} and smaller than V_{Am} (note that this is a feature observed in the asymmetric cases discussed in subsection 3.4.1).

At this time ($t = t_3$), the reconnection process is likely to reach a quasi-steady state and the magnetic field direction reversal is mainly accomplished by the intermediate shock. The current sheet associated with this intermediate shock will then mark the position of the magnetopause. Note that due to the large Alfvén velocity V_{Am} on the magnetospheric side, the whole process from $t = t_1$ to $t = t_3$ should be very short, with a time scale $\Delta t = t_3 - t_1$, the order of $\Delta t \sim l/V_{Am}$, where l is the width of the reconnection layer. Therefore, in a reconnection process with largely different Alfvén velocities on the two sides of the reconnection layer, the reconnection layer is likely to be bounded by an intermediate shock on the low Alfvén speed side and a weak slow shock on the high Alfvén speed side. The evolution process suggested above is only a qualitative one. The quantitative aspects of this process are worth further study.

3.5 Summary and Discussion

In summary, this chapter has presented studies of the reconnection layer structures under different symmetry conditions. In particular, the effects of three parameters on the structure of the reconnection layer were investigated systematically, these three parameters being the degrees of asymmetry in magnetic field strengths and in plasma densities on both sides of the reconnection layer and the plasma β value. The results are as follows:

1. In a symmetric configuration with low plasma β (Case 1), the reconnection layer is found to be bounded by a pair of slow shocks as predicted in *Petschek*'s [1964] original model. At the center of the reconnection layer, the plasma density shows a local minimum which is identified to be associated with a pair of contact discontinuities within the reconnection layer. The plasma flowing across the pair of slow shocks and into the reconnection layer from both sides is accelerated to high speed by the pair of slow

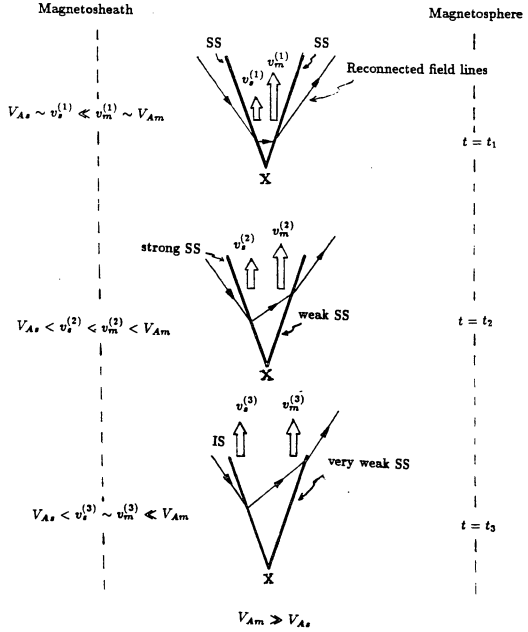

Figure 3.21 Evolution of the shock structure in the reconnection layer.

shocks in the outflow direction. In the reconnection layer, the magnetic field strength is reduced (a property of the slow shock) while the plasma pressure is increased. The result from this case may be applicable to the magnetic reconnection in the magnetotail.

However, when plasma β is high, the discontinuity structures in the reconnection layer appears to be less evident.

2. In the presence of an asymmetry in magnetic field strengths on the two sides of the reconnection layer (Case 3), intermediate and slow shocks may coexist to bound the low field edge of the reconnection layer, while the other edge of the reconnection layer is bounded by a slow shock downstream in which a thin layer of high plasma density appears.

3. For a small asymmetry in plasma densities on the two sides of the reconnection layer (Case 4), the structure of the reconnection layer resembles the symmetric case, qualitatively. The reconnection layer is also bounded by a pair of slow shocks and two contact discontinuities can be identified in the reconnection layer. However, the slow shock on the high plasma density side will be stronger than the slow shock on the other side.

For a large asymmetry in plasma densities (Case 5), the structure of the reconnection layer is different from that in the symmetric case both qualitatively and quantitatively. The reconnection layer is now bounded by an intermediate shock on the high plasma density side and a weak slow shock on the low plasma density side. Only one contact discontinuity can be identified within the reconnection layer.

4. For cases with large asymmetry in plasma densities (Case 5 and Case 6), an increase in magnetic field strength on the low plasma density side will not change qualitatively the reconnection layer structure on the two edges. However, in the case of a large magnetic field strength on the low plasma density side (corresponding to a large β value on the high plasma density side), the discontinuity structure in the reconnection

layer is not evident (Case 7), similar to the situation with a large β in the symmetric case (Case 2).

5. Case 5, Case 6, and Case 7 are cases with plasma and magnetic field parameters appropriate for the dayside magnetopause. In applying these cases to the dayside magnetopause, the magnetopause can be identified as corresponding to the intermediate shocks in Case 5 and Case 6 and to the whole reconnection layer in Case 7. In all three cases, the magnetopause boundary layer can be identified as the reconnection layer with enhanced plasma flow. The plasma in the boundary layer comes mainly from the magnetosheath side.

Hence, it is suggested that for low and medium β values, the reconnection layer at the dayside magnetopause may be bounded by an intermediate shock on the magnetosheath side and a weak slow shock on the magnetospheric side.

6. The appearance of intermediate shocks can be attributed to the large difference in Alfvén speeds on the two sides of the reconnection layer. Both asymmetry in plasma density and magnetic field strengths may cause such asymmetry in Alfvén speeds. Under the typical dayside magnetopause condition, the Alfvén speed on the magnetospheric side is usually much larger than the Alfvén speed in the magnetosheath. Hence, an intermediate shock is likely to appear to bound the magnetosheath edge of the reconnection layer while a weak slow shock is possible on the other edge of the reconnection layer.

Finally, the effects of β and B_y on the reconnection layer structure are discussed below.

The effect of plasma β on the strength of slow shocks has been studied by *Edmiston and Kennel* [1986], who conducted a parametric survey of the Rankine-Hugoniot solutions for slow MHD shock waves. They found that, when $C_{s1}^2 \gg C_{A1}^2$ (or, equivalently,

the plasma $\beta = (2/\gamma)C_{s1}^2/C_{A1}^2 \gg 1$), all slow shocks permitted by the evolutionary conditions are weak, where C_{s1} and C_{A1} are the upstream sound speed and Alfvén speed, respectively. The reason is that, when $C_{s1}^2 \gg C_{A1}^2$, the slow and intermediate MHD wave speeds are nearly equal. On the other hand, they found that slow shocks can be strong when $C_{S1}^2 \ll C_{A1}^2$ (or plasma $\beta \ll 1$). Their analytical results are consistent with our simulation. In addition, our simulation shows that plasma β may also affect the intermediate shocks significantly. This later subject is worth further investigation, as at the dayside magnetopause the plasma β in the magnetosheath varies considerably.

The simulation results presented in this chapter are purely two-dimensional cases in which $B_y = 0$. At the dayside magnetopause, it is common that the magnetosheath field and geomagnetic field are not strictly antiparallel, namely, $B_y \neq 0$. In this case, rotational discontinuity(ies) may exist to rotate the magnetosheath and magnetospheric fields to a common plane.

Chapter 4. Mechanisms for B_y Enhancement in the Current Sheet and Magnetic Flux Tubes at the Dayside Magnetopause and in the Magnetotail

4.1 Introduction

At the dayside magnetopause, a "bulge-out" feature in the magnetic field vector hodogram across the magnetopause current layer is observed [*Russell and Elphic*, 1978]. In the magnetotail neutral sheet, an enhanced magnetic field B_y component is often found [*Lui*, 1984]. In addition, there has been well established evidence that the magnetic flux tubes formed in the observed flux transfer events (FTEs) at the dayside magnetopause often have strong core magnetic field or guide field [*Paschmann et al.*, 1982]. Likewise, some of the magnetic flux tubes found in the magnetotail also reveal an enhanced core magnetic field [*Elphic et al.*, 1986; *Sibeck et al.*, 1984]. In this chapter, it will be shown that these observations may be related phenomena and could be explained by two proposed processes termed in this chapter as: (1) B_y enhancement in the current sheet and (2) B_y in the magnetic flux tubes. First, a mechanism is proposed in this chapter for the B_y enhancement in a current sheet. Second, another mechanism is suggested for the enhanced B_y flux associated with magnetic flux tubes formed in such a current sheet. Third, to illustrate and support the proposed mechanisms, computer simulations are carried out. Finally, the B_y enhancement in a current sheet and in magnetic flux tubes is applied to explain the observed "bulge-out" feature in magnetic

field hodograms at the dayside magnetopause, the enhanced dawn-dusk magnetic field component in the magnetotail, and the enhanced core magnetic field inside magnetic flux tubes.

In Section 4.2, observations of the "bulge-out" feature in magnetic field hodograms at the dayside magnetopause, the enhancements of dawn-dusk magnetic fields in the magnetotail current sheet, and enhanced core fields in magnetic flux tubes in the magnetosphere are presented. Section 4.3 reviews the relevant theories. Section 4.4 proposes the mechanism for the B_y enhancement in the current sheets while the mechanism for the core field enhancement associated with magnetic flux tubes is described in section 4.5. In both sections 4.4 and 4.5, related MHD simulation results are also presented and, on the basis of the proposed processes and the simulation results, explanations are provided for the observations cited above. Section 4.6 concludes the chapter with a summary and discussion.

Before continuing to the next section, the following provides a brief topological description of the magnetic field configurations to be used in the studies in this chapter. The current sheet structure is first illustrated, followed by a description of the magnetic flux tubes. The key terms B_y and core magnetic field used in this chapter will also be defined.

When two bodies of magnetized plasma approach close enough, a layer of current or current sheet will be formed at the interface of these two bodies of plasma, provided that the embedded magnetic fields on the two sides of the interface have an antiparallel component. Figure 4.1*a* illustrates the configuration of a current sheet in a two-dimensional geometry. In Figure 4.1*a*, the magnetic fields **B** are in the plane of the paper and directed to the right (above the current sheet) and to the left (below the current sheet). The current **I** in the current sheet is pointing inward perpendicular to the plane of the paper. When magnetic reconnection between the magnetic fields on

the two sides of the current sheet occurs at two sites in the current sheet. a magnetic island will be formed as shown in Figure 4.1*b*. In Figure 4.1*b*, the two reconnection sites are marked by two cross symbols. Such current sheet structures are found at the earth's dayside magnetopause in the presence of a southward interplanetary field and in the magnetotail where the magnetic fields in the northern sector and southern sector have a large antiparallel component. In Figure 4.1*a*, if, in addition to the antiparallel component in the plane of the paper as shown, the magnetic fields on the two sides of the current sheet also have a common component perpendicular to the plane of the paper, the magnetic field configuration will then be called a sheared one. In reality, the magnetospheric current sheets often are associated with the sheared magnetic configurations. Correspondingly, in a current sheet associated with sheared magnetic configuration, magnetic flux tubes can be formed as a result of magnetic reconnections along two reconnection lines (X lines), whereas in a strictly 2-D current sheet associated with only antiparallel magnetic fields, a magnetic island is formed. Hence, the magnetic flux tube may be called a 3-D "magnetic island". In a strictly 2-D configuration, the magnetic field at the center of a current sheet or magnetic island is exactly zero while, in a 3-D configuration, it could be finite and in the direction of the common magnetic field component. Figure 4.1*c* is a sketch of a magnetic flux tube at the core of which exists a non-zero magnetic field, referred to as the "core magnetic field" in the literature.

For convenience of presentation in this chapter, the common component of magnetic fields associated with a 3-D current sheet configuration (sheared magnetic field configuration) and the resultant magnetic flux tube will be defined as the B_y component. The y direction defined here should not be confused with the y direction in the GSM (Geocentric Solar Magnetospheric) coordinates. In the magnetotail, the common component of tail magnetic fields above (north) and below (south) the tail neutral sheet

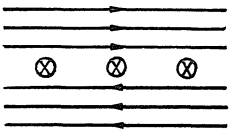

Current sheet

(a)

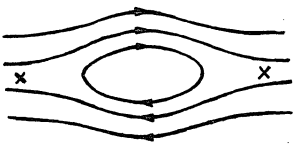

Magnetic island

(b)

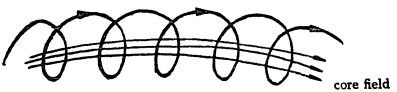

Magnetic flux tube

(c)

Figure 4.1 Schematic illustration of current sheet, magnetic island, and magnetic flux tube. (a) Two-dimensional current sheet. The solid straight lines are magnetic field lines in the direction of the arrows. The current I in the current sheet is perpendicular to the paper and directed inward as marked by three small circles with cross symbol. (b) Magnetic island formed in a 2-D current sheet. The solid lines are magnetic field lines and the two cross symbols mark the reconnection sites. (c) Magnetic flux tube with a core field. The heavy lines are magnetic field lines on the outer layer of the flux tube and the light lines are magnetic field lines near the core of the tube (core field).

is more or less in the y direction of the GSM coordinates. However, at the dayside magnetopause, the common component of the interplanetary magnetic field (IMF) and the geomagnetic field is not necessarily in the y direction of GSM coordinates. Only when the IMF is purely southward will the y direction used here coincide with that in the GSM coordinates.

4.2 Observations

4.2.1 Microstructures of the dayside magnetopause: the "bulge-out" feature

The "bulge-out" feature in magnetic field vector hodograms across the magnetopause was reported by *Russell and Elphic* [1978] in the satellite data from ISEE-1 and -2 magnetopause crossings. Figure 4.2*a* shows two typical cases of magnetic field variations across the dayside magnetopause presented in the original *Russell and Elphic* [1978] paper. The data in Figure 4.2*a* was obtained from ISEE-1 and -2 satellites' crossings of the dayside magnetopause on November 3, 1977. Shown in Figure 4.2*a* are the variations of the tips of magnetic field vectors from the magnetospheric side of the magnetopause current layer to the magnetosheath side. In Figure 4.2*a*, the letters m and s denote the magnetospheric side and magnetosheath side, respectively. Such a figure is called a hodogram of magnetic field vectors. The coordinate system in Figure 4.2*a* is the so-called boundary normal coordinates used widely in the presentation of magnetic field data at the dayside magnetopause. Figure 4.2*b* illustrates the boundary normal coordinates. The N direction is normal to the local magnetopause surface, the L direction is the projection of the Z direction in the Geocentric Solar Magnetospheric (GSM) coordinates onto the magnetopause surface defined by N, and M completes the right-handed orthogonal system. It is seen in Figure 4.2*a* that the B_N component (right panels) remains almost zero during the crossings, implying a tangential magnetopause

discontinuity, and the magnetic field vectors in the L-M plane (left panels) rotate across the magnetopause. In the L-M plane, the magnetic field vector shows a "bulge-out" feature. To define the term "bulge-out", Figure 4.2*c* illustrates two hodograms of a magnetic field vector, one with a "bulge-out" feature (lower hodogram) and the other without (upper hodogram). If the tips of the magnetic field vector **B** rotating from Side 1 to Side 2 across the current sheet all fall on a straight line connecting the tips of the two magnetic vectors on Side 1 and Side 2, the structure is called a "non-bulge-out" structure. On the other hand, if the magnetic field vectors in the rotation are all larger than those defined by the straight line connecting point 1 and 2, the structure is then called a "bulge-out" structure. The "bulge-out" feature of B_L and B_M hodograms as shown in Figure 4.2*a* exists in almost all the ISEE satellites magnetopause crossing cases studied by *Russell and Elphic* [1978] with a southward, northward, or horizontal interplanetary magnetic field (IMF) orientation. It is therefore likely to be a common feature of the dayside magnetopause current layer.

4.2.2 B_y enhancement in the magnetotail neutral sheet

In the earth's magnetotail, one of the signatures of the neutral sheet is the existence of a large dawn-dusk magnetic field component [e.g., *Lui*, 1984]. The neutral sheet in the earth's magnetotail was discovered almost two decades ago by magnetic field measurements from IMP 1 [*Ness*, 1965]. The neutral sheet was recognized as the region in which the magnetic field orientation reverses from pointing sunward to tailward or vice versa. For a group of multiple neutral sheet crossings, it is often found that the B_y (dawn-dusk) component of the magnetic field is nonzero and maintains the same sign throughout all crossings. Investigations of the relationship of the B_y component in the magnetotail and in the interplanetary magnetic field (IMF) reveal that B_y in the tail

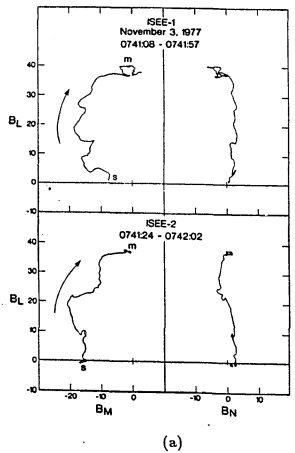

(a)

Figure 4.2 (a) Hodogram of high resolution magnetic field data in boundary normal coordinates across the magnetopause [*Russell and Elphic*, 1978]. s and m denote the magnetosheath side and magnetospheric side, respectively. The upper panel shows the measurements by ISEE-1 and the lower panel by ISEE-2. B_L, B_M, and B_N are magnetic field L, M, and N components, respectively, where N is in the normal direction of the local magnetopause surface.

Boundary Normal Coordinates

$\hat{N}$ **is normal to the magnetopause**

$$\hat{M} = \frac{\hat{N} \times \hat{Z}_{GSM}}{|\hat{N} \times \hat{Z}_{GSM}|}$$

$$\hat{L} = \hat{M} \times \hat{N}$$

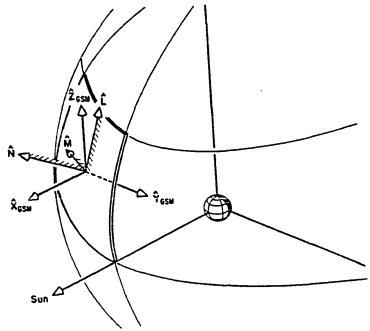

(b)

Figure 4.2 (b) The definition of boundary normal coordinates. N is normal to the local magnetopause surface, the L direction is the projection of the Z_{GSM} component on the magnetopause surface defined by N, and M completes the right-hand orthogonal system [*Berchem and Russell*, 1982].

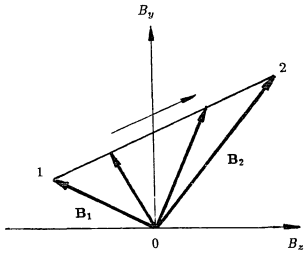

Non-"bulge-out"

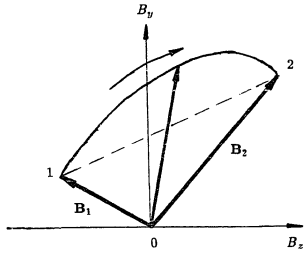

"bulge-out"

(c)

Figure 4.2 (c) Schematic illustration of hodograms with and without a "bulge-out" feature. Numeral 1 and 2 denote Side 1 and Side 2 of a current sheet where magnetic fields are $\mathbf{B}_1$ and $\mathbf{B}_2$, respectively. The heavy arrows are magnetic field vectors and the light arrows indicate the direction of rotation of magnetic vectors across the current sheet. The curves connecting point 1 and point 2 are traces of the tips of the rotating magnetic field vector. The upper hodogram does not have a bulge-out feature, while the lower one is a "bulge-out" hodogram.

is correlated to the B_y in the IMF [*King*, 1977; *Fairfield*, 1979; *Tsurutani et al.*, 1984]. *Fairfield* [1979] has examined the dawn-dusk field component in the earth's magnetotail based on IMP 6 measurements. When the effects of tail flaring and aberration of the tail axis are subtracted, it is found that the residual B_y component is correlated statistically with the interplanetary B_y component by

$$B_y(tail) = 0.13B_y(interplanetary) - 0.30nT. \tag{4.1}$$

Equation (4.1) suggests that the dawn-dusk component of the interplanetary magnetic field penetrates partially ($\sim$ 13%) into the magnetotail. Earlier, *King* [1977] also studied the correlation of the dawn-dusk magnetic field component in the neutral sheet and in that of the interplanetary magnetic field. Figure 4.3 shows a scatter plot between the averaged B_y component in multiple neutral sheet crossings (B_{yT}) versus the hourly averaged dawn-dusk component of the interplanetary magnetic field (B_{yIP}) taken from *King* [1977]. A linear regression fit (straight line) gives

$$B_y(tail) = (0.5 \pm 0.1)B_y(interplanetary) - (0.5 \pm 0.2)nT, \tag{4.2}$$

with a correlation coefficient of 0.6 (the slope of the fitted straight line) while the correlation coefficient in *Fairfield*'s [1979] study is only 0.13 (see (4.1)). *Lui* [1984] pointed out that the correlation found by Fairfield is based on magnetic field measurements over the entire magnetotail sampled by IMP 6 and thus includes tail regions outside the neutral sheet, whereas King's result is derived from data in the neutral sheet only. Equation (4.2) implies that about 50% of the B_y component of the interplanetary magnetic field penetrates into the neutral sheet region. Noting this difference, *Lui* [1984]

suggested that the dawn-dusk component of the interplanetary magnetic field (B_y) is enhanced in the neutral sheet of the magnetotail.

4.2.3 Core field associated with magnetic flux tubes

At the dayside magnetopause, the observed flux transfer events (FTEs) are now widely accepted as evidence in support of the dayside sporadic magnetic reconnections. As reviewed in Chapter 1, various dayside reconnection models have been proposed in the process of interpreting FTEs. In *Russell and Elphic*'s [1978] model, FTEs are envisaged as passages of magnetic flux tubes resulting from patchy reconnections. *Lee and Fu* [1985] proposed an alternative model which predicts that in the presence of a southward interplanetary magnetic field with a finite B_y component, multiple X-line reconnections can lead to the formation of magnetic flux tubes at the dayside magnetopause. The subsequent poleward convection of these magnetic flux tubes produces magnetic field deflections which may be observed as FTEs. In both Russell and Elphic and Lee and Fu's models, FTEs are related closely to localized magnetic flux tubes. In Scholer and Southwood et al.'s model, FTE signatures are suggested to be produced by bursty reconnection at a single X line extended over a large longitudinal segment of the dayside magnetopause. In the presence of finite B_y in the interplanetary magnetic field, the single X-line bursty reconnection gives rise to a loop-like structures twisted in the y direction. The loop-like structure in this model is similar to magnetic flux tubes in the Lee-Fu model except that the loops are closed in the Lee-Fu model due to double reconnections.

One of the observational facts of FTEs is that the magnetic field strength often shows a clear increase at the center of FTEs. Figure 4.4 shows an example of FTE observations with the an increased B feature. Shown in Figure 4.4 are the variations

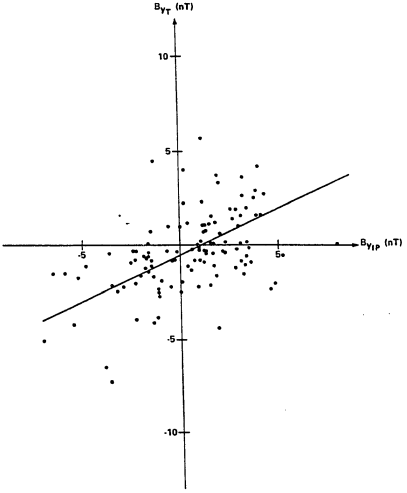

Figure 4.3 A plot of the average B_y component in multiple neutral sheet crossings (B_{yT}) versus the hourly B_y component of the interplanetary magnetic field (B_{yIP}) at the corresponding time. A linear correlation is indicated, suggesting that about 50% of the B_y component of the interplanetary magnetic field penetrates into the neutral sheet region [*King*, 1977].

of the magnetic field as a function of time. B_L, B_M, and B_N are the L, M, and N components of the magnetic field in the boundary normal system (see Figure 4.2c for a illustration), respectively, while $|B|$ is the magnitude of the magnetic field. It can be seen in Figure 4.4 that the three bipolar B_N pulses (FTEs) at UT$\sim$ 1421, 1442, and 1454 correspond to three peaks in the magnetic field magnitude $|B|$. This feature has been attributed to a strong core magnetic field inside the FTE magnetic flux tubes [e.g., *Paschmann et al.*, 1982].

In the magnetotail, the existence of B_y within the plasmoids has been confirmed [*Hones et al.*, 1982; *Sibeck et al.*, 1984; *Scholer et al.*, 1985; *Richardson and Cowley*, 1985; *Elphic et al.*, 1986; *Nishida et al.*, 1986]. The existence of B_y in plasmoids requires the conventional plane picture of plasmoids to be extended to a 3-dimensional structure, leading to the flux tubes picture. In search of the origin of B_y in the plasmoids, *Hughes and Sibeck* [1987] compared observations of B_y within plasmoids and related tail structures reported in the literature with simultaneous upstream IMF B_y data from the IMF data book. They concluded that the B_y within plasmoids may also result from the penetration of IMF B_y. In particular, magnetic field observations on ISEE-1 and -2 in and near the neutral sheet about 20 R_E down th near-Earth magnetotail [*Elphic et al.*, 1986] reveal the occurrence of structures resembling magnetic flux ropes with scale size of roughly 3–5 R_E. The structure of these magnetic flux ropes was found to be strikingly similar to that of flux transfer events at the dayside magnetopause. In addition, a large core field was seen inside these flux ropes. Figure 4.5 shows the actual observational data from ISEE satellites [*Elphic et al.*, 1986]. In Figure 4.5, B_x, B_y, and B_z are the three components of the magnetic field in Geocentric Solar Magnetospheric coordinates, $|B|$ is the magnitude of the magnetic field, and $\mathbf{V}_\perp$ is the inferred $\mathbf{E} \times \mathbf{B}$ flow velocity. One magnetic flux rope structure at UT$\sim$1922 can be identified by a negative-positive bipolar structure of B_z. Note that at the center of the bipolar B_z

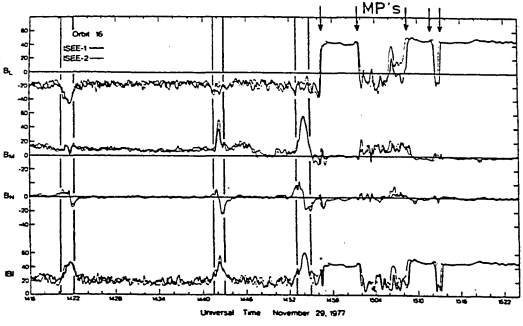

Figure 4.4 Data from ISEE 1 for a one-hour period on 29 November 1977, showing 3 FTEs, numbered 1–3, all located in the magnetosheath. There are five magnetopause crossings, the first at $\sim$ 1456.30UT, identified by the large increase in B_L. B_L, B_M, and B_N are magnetic field components in L, M, and N directions of the boundary normal coordinates. $|B|$ is the strength of magnetic field. The spacecraft location in terms of geocentric radial distance R and GSM local time and latitude during this interval was approximately 12 R_E, 0830 hours, and 22°, respectively [*Paschmann et al.*, 1982].

structure, B_y becomes large in the negative y (dusk-dawn) direction, suggesting a large core magnetic field in the magnetic flux ropes.

4.3 Brief Reviews of the Relevant Theories

The observed "bulge-out" feature in **B** vector hodograms in the dayside magnetopause has been studied by *Lee and Kan* [1979]. In Lee and Kan's work, a self-consistent model of the tangential magnetopause is formulated on the basis of the time-independent Vlasov-Maxwell equations. In their model, plasmas on both sides are magnetized; the magnetic field is assumed everywhere parallel to the magnetopause and is allowed to rotate through an arbitrary angle across the magnetopause. Figure 4.6 is one case they obtained showing the rotation of the magnetic field across the magnetopause (or magnetic field hodogram in y-z plane), where B_z and B_y are z and y components of the magnetic field in the Geocentric Solar Magnetospheric coordinates, B_0 is the normalization unit, S and M denote the magnetosheath side and magnetospheric side, respectively. The bulge-out feature of the magnetic field vector similar to that observed by ISEE satellites (see Figure 4.2a) can be clearly seen in Figure 4.6. These authors have attributed the bulge-out feature in the magnetic field hodogram produced in their model magnetopause to the lack of overlap between plasmas from the two sides of the dayside magnetopause. *Lee and Kan*'s [1979] work demonstrated that magnetic field structures with a "bulge-out" feature in **B** vector hodogram are possible steady-state configurations of the dayside magnetopause. However, their work did not answer the question of how this state is reached, which is one of the topics of this chapter.

In the framework of the single X-line bursty reconnection model (see Chapter 1 for a review), *Scholer* [1988*b*] proposed a sweeping-up mechanism for the observed core field enhancement in flux transfer events (FTEs) at the dayside magnetopause. His proposed

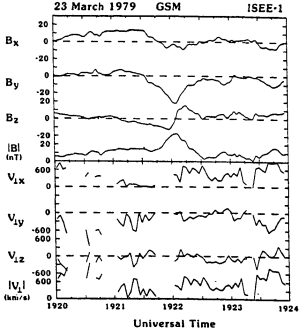

Figure 4.5 Detail of magnetic field and inferred $\mathbf{E} \times \mathbf{B}$ velocities in GSM coordinates for the UT~1922 event. Note the bipolar signature in B_Z and the large $-B_y$ excursion centered on it. A strong (500 km/s) earthward flow carries the structure past the spacecraft [*Elphic et al.*, 1986].

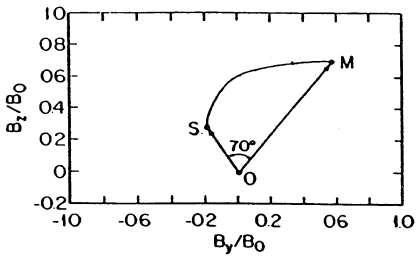

Figure 4.6 Theoretical hodogram of a magnetic field vector across the magnetopause obtained by *Lee and Kan* [1979]. s and m denote the magnetosheath side and magnetospheric side, respectively. The coordinates are the GSM coordinates. B_0 is the normalization unit of the magnetic field in the calculation.

process of core field enhancement is illustrated in Figure 4.7, where the plane marks the magnetopause boundary, $\mathbf{B}_2$ and $\mathbf{B}_1$ are magnetic fields on the magnetospheric and magnetosheath sides, respectively, and $\mathbf{B}_{mp0}$ is the magnetic field in the direction of the common component of $\mathbf{B}_2$ and $\mathbf{B}_1$, or $\mathbf{B}_{mp0}$ is perpendicular to $\Delta\mathbf{B} = \mathbf{B}_2 - \mathbf{B}_1$ [e.g., *Sonnerup*, 1976]. This magnetopause field, $\mathbf{B}_{mp0}$, is zero only when the magnetosheath and magnetospheric field is exactly antiparallel. In the single X-line bursty reconnection model of FTEs, the open-ended loops as shown in Figure 4.7 are produced after the magnetic flux comprising the original magnetopause has been reconnected and IMF becomes connected to the geomagnetic field. Due to the Maxwell stresses produced by the bending of loop field lines, the loops will move along the magnetopause away from the X line (upward in Figure 4.7). As long as the speed of the loops exceeds the ambient flow speed of plasma in the magnetopause, the magnetopause field $\mathbf{B}_{mp0}$ will get swept up in the interior of the loop. Noting that the loops are distributed over a large longitudinal segment corresponding to the length of the X line, Scholer suggested that the sweeping-up process of the magnetopause field may lead to a continuously increase of magnetic field in the center of the loops, which may constitute the strong core magnetic field in FTEs. Along this line of argument, Scholer predicted that neither the Russell-Elphic connected tube model nor the Lee-Fu multiple X line reconnection model can account for an enhancement of the core magnetic field strength since the magnetic flux tubes formed in the Russell-Elphic and the Lee-Fu models are closed instead of open loops in Scholer's model. The work presented in this chapter is motivated partly by this latter assertion of Scholer's. It will be shown in this chapter that an enhancement of the core field is also possible in closed magnetic flux tubes.

However, for the enhanced B_y in the magnetotail neutral sheet and magnetic flux ropes as discovered by *Elphic et al.* [1986], so far no theoretical explanations have been given. On the other hand, much of the emphasis in theoretical work concerning the

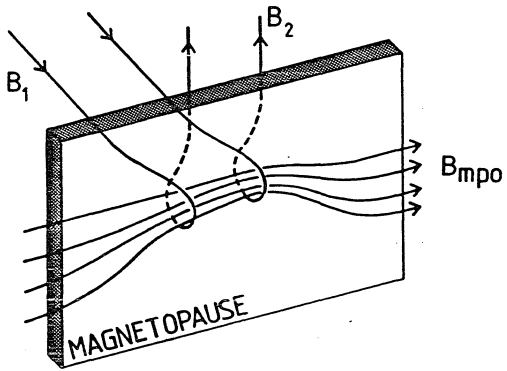

Figure 4.7 Schematic drawing of part of the magnetopause after bursty reconnection at a single X line has produced magnetic field loops over some longitudinal distance. Two loops connecting the magnetosheath field $\mathbf{B}_1$ and the magnetospheric field $\mathbf{B}_2$ are shown. During their northward motion, these loops collect the magnetopause field $\mathbf{B}_{mp0}$ [*Scholer*, 1988*b*].

B_y in the magnetotail has been on the origin of magnetotail B_y and its significance in plasma processes in the magnetotail. *Cowley* [1981] suggested that by flux conservation an internal B_y field having the same sign as the IMF B_y must be present in the tail lobes. He attributed the presence of B_y to the penetration of IMF B_y as a result of the magnetospheric relaxation in response to the torque produced by dayside reconnection. *Sibeck* [1985] argued that the penetration of the IMF B_y into the tail may be a consequence of the interconnection of magnetotail and magnetosheath field lines within the latitudinally limited "window" [*Stern*, 1973] where the magnetopause is a rotational discontinuity. The existence of a significant B_y in the plasma sheet was also noted by *Akasofu et al.* [1978] who found that this B_y often varies systematically with B_z, and therefore a 3-D analysis of the magnetic fields in the magnetotail is needed.

4.4 Mechanism of B_y Enhancement in the Current Sheet

4.4.1 Mechanism

As mentioned in section 4.2, the magnetic field hodograms of the dayside magnetopause obtained from ISEE magnetopause crossings have revealed a "bulge-out" feature [e.g., *Russell and Elphic*, 1978] and an enhancement of the B_y component was observed in the magnetotail neutral sheet [*Lui* , 1984]. It will be shown in this section that the bulge-out feature in the magnetic field hodogram of the dayside magnetopause can be explained by the same B_y enhancement process as in the magnetotail neutral sheet. In the following, a mechanism will be proposed for the B_y enhancement in the magnetopause and magnetotail current sheets.

First, we consider the B_y enhancement at the dayside magnetopause. Suppose that the current sheet has initially a sheared magnetic field configuration with a finite B_y

component as given by

$$\mathbf{B}(x) = B_{0z} tanh(x/a)\hat{\mathbf{z}} + B_{0y}\hat{\mathbf{y}}, \tag{4.3}$$

where a is the thickness of the current sheet and B_{0z} and B_{0y} are constants. Note that the coordinates are not exactly Geocentric-Solar-Magnetospheric (GSM) coordinates. In (4.3), the antiparallel component of the magnetic field is in the z-direction and the common component of the magnetic field is in the y-direction. The rotation of the magnetic field vector $\mathbf{B}$ across the current sheet represented by (4.3) is shown in Figure 4.8. In the present symmetric case, since a constant B_{0y} is assumed, the hodogram of the current sheet is a non-"bulge-out" one as can be seen in Figure 4.8. Hence, if the B_y at the center of the current sheet is increased while B_y on the two sides of the current sheet remains more or less unchanged, a bulge-out in the magnetic field hodogram will appear. At the dayside magnetopause, the magnetic field structure with a bulge-out feature in its hodogram has been shown by *Lee and Kan* [1979] to be a stable state. A process is suggested in the following that can lead to such a state. For the symmetric configurations described in (4.3), if magnetic fields on both sides of the current sheet are carried by impinging plasma flows toward the current sheet, one would expect, in the absence of magnetic reconnection, a pile-up of magnetic fields in the current sheet. One would also expect that the incoming plasma, upon reaching the current sheet, will be deflected and move out along the magnetic field lines. In the case of dayside magnetopause, a pile-up of magnetic field near the subsolar point is expected and, as pointed out by *Lees* [1964] and *Zwan and Wolf* [1976], the solar wind plasma at the dayside magnetopause is likely to be squeezed out of the dayside region by the solar wind ram pressure along magnetic field lines. Therefore, near the central plane of the current sheet ($x = 0$ where $B_z = 0$), plasma is expected to flow along magnetic field lines, which are in the y-direction, and move out of the subsolar region. However, the field-aligned

plasma flow will not carry the magnetic field away. As a consequence, the pile-up of the magnetic field and the squeeze-out of plasma at the dayside magnetopause will lead to the enhancement of B_y in the dayside current sheet. The process suggested here for B_y enhancement in the current sheet seems simple and intuitive. The key factor in this mechanism is the time scale for the magnetic field pile-up. Note that a significant and observable pile-up of the magnetic field would require that the characteristic time (τ_p) for magnetic field pile-up be less than the convection time (τ_c) during which magnetic fields are convected out of the dayside magnetopause region by perpendicular plasma flows. One objective of the simulations below is to show that the pile-up time τ_p is usually small and, therefore, this last requirement is in fact easily satisfied.

It is therefore suggested that the pile-up and squeezing process as described above may account for the B_y enhancement in the magnetopause and likewise, in the magnetotail current sheet. At the dayside magnetopause, the interplanetary magnetic fields (IMF) carried by the solar wind toward the dayside region is often observed to have a finite B_y component. Similarly, in the magnetotail lobe region, a finite B_y component is also observed (see observations cited in section 4.2). It is therefore possible that the driving force caused by the cross-tail electric field in the magnetotail lobe region would lead to the B_y enhancement in the tail neutral sheet. To demonstrate this, MHD simulations were carried out and are presented below.

4.4.2 Simulation

Figure 4.9 illustrates schematically the simulation setup. The simulation is two-dimensional. In the chosen simulation plane, the x-y plane, a sheared magnetic field configuration represented by (4.3) is specified at $t = 0$. Hence the distribution of the magnetic field component (B_y) in the simulation plane is uniform at time $t = 0$ while the current

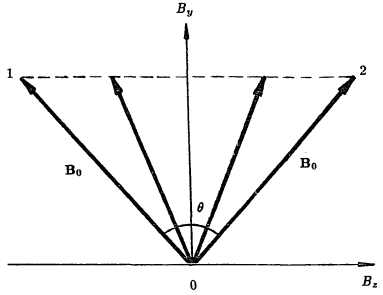

Figure 4.8 Rotation of magnetic field vector $\mathbf{B}$ from side 1 to side 2 in a symmetric sheared magnetic field configuration represented by equation (4.3). The direction of the common component of the sheared configuration is y and z is the direction of the antiparallel component. Numeral 1 and 2 denote side 1 and side 2 of the current sheet. B_0 is the strength of magnetic field outside the current sheet and θ is the angle between the two magnetic field vectors on side 1 and side 2.

sheet structure is produced by the antiparallel component of the magnetic field (B_z). Plasma flows are then imposed on the two sides of the current sheet or on the two driven boundaries of the simulation domain. Along with the plasma flows, the embedded magnetic field, which lies initially outside the current sheet, will be carried in towards the current sheet from the two driven boundaries. As time goes on, B_y will pile up in the current sheet while the incoming plasma exits the simulation region approximately in the positive and negative x direction. Note that since the antiparallel component B_z of the magnetic field $\mathbf{B}$ is perpendicular to the simulation domain, magnetic reconnection will not occur as we intend (B_y enhancement in a tangential discontinuity boundary is the subject of interest here). In the following a detailed description of the simulation method is given.

The simulation domain is a rectangular box in the x-y plane extending in x direction from $-L_x$ to L_x and in y direction from $-L_y$ to L_y. In the case of dayside magnetopause, x is in the anti-sunward direction and y the dusk-dawn direction. In the case of the magnetotail neutral sheet, x is in the southward direction and y in the dusk-dawn direction. In simulation planes thus chosen, the antiparallel component of magnetic fields is always in the z direction.

A two-dimensional compressible MHD code is used to simulate the pile-up of magnetic fields and the squeezing of plasmas at the current sheet. Hereinafter, the magnetic field, density, velocity, pressure, length, current density, resistivity, and time are expressed in units of B_0, ρ_0, Alfvén speed $V_{A0} = B_0/\sqrt{\mu_0\rho_0}$, B_0^2/μ_0, a, $B_0/\mu_0 a$, $\mu_0 a V_{A0}$, and Alfvén transit time $t_A = a/V_{A0}$, respectively, where B_0 and ρ_0 are the initial magnetic field strength and density outside the initial current sheet, which has a half

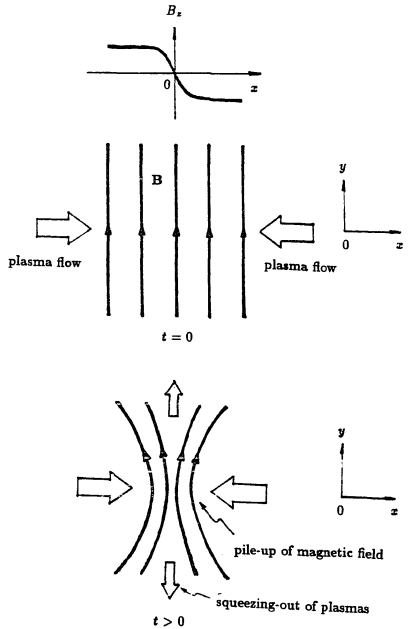

Figure 4.9 Schematic illustration of simulation setup. At time $t = 0$, the current sheet structure is produced by the antiparallel component B_z of the magnetic sheared configuration. The profile of B_z is shown on top. In the x-y plane (the simulation plane) the magnetic field (heavy lines with arrows) are initially uniform. Plasma flows (represented by the hollow arrows) are imposed on the two sides of the current sheet. At $t > 0$, pile-up of magnetic field occurs at the center of the current sheet while plasma is being squeezed out in the y direction.

thickness a, respectively, and μ_0 is the magnetic permeability in free space. The governing equations used are

$$\frac{\partial \rho}{\partial t} = -\nabla \cdot (\rho \mathbf{v}) \tag{4.4}$$

$$\frac{\partial (\rho \mathbf{v})}{\partial t} = -\nabla \cdot [\rho \mathbf{v}\mathbf{v} + (p + \frac{B^2}{2})I - \mathbf{B}\mathbf{B}] \tag{4.5}$$

$$\frac{\partial \mathbf{B}}{\partial t} = \nabla \times (\mathbf{v} \times \mathbf{B}) - \nabla \times \eta \mathbf{j} \tag{4.6}$$

$$\frac{\partial \epsilon}{\partial t} = -\nabla \cdot \mathbf{S} \tag{4.7}$$

where ρ, $\mathbf{v}$, p, $\mathbf{B}$, $\mathbf{j}$, ϵ, and η, are plasma density, velocity, pressure, magnetic field, current density, energy density, and resistivity, respectively. Current density $\mathbf{j}$, energy ϵ, and energy flux $\mathbf{S}$, are defined as follows

$$\mathbf{j} = \nabla \times \mathbf{B} \tag{4.8}$$

$$\mathbf{S} = (\epsilon + p + \frac{B^2}{2})\mathbf{v} - (\mathbf{B} \cdot \mathbf{v})\mathbf{B} + \eta \mathbf{j} \times \mathbf{B} \tag{4.9}$$

$$\epsilon = \frac{1}{2}\rho v^2 + \frac{B^2}{2} + \frac{p}{\gamma - 1} \tag{4.10}$$

where γ is the adiabatic constant chosen to be $\gamma = 5/3$. Equations (4.4)–(4.10) are expressed in normalized form. The finite differencing scheme for (4.4) to (4.7) is the same as used in Chapter 3 (see Appendix).

An initial plasma and magnetic field configuration, which varies only in the direction (the x direction) across the current sheet, is given by (4.3). For convenience, two quantities θ_L and B_0 are introduced, where θ_L is the angle between the magnetic field vectors on each side of the current sheet and B_0 is the magnetic field strength on the two sides of the current sheet (as illustrated in Figure 4.8). In terms of θ_L and B_0, we have $B_{0x} = sin(\theta_L/2)B_0$ and $B_{0y} = cos(\theta_L/2)B_0$ in (4.3). Figure 4.10*a* is a schematic sketch of the initial magnetic field configuration in the simulation domain. Figures 4.10*b* and *c* are the initial magnetic field configuration viewed along the y direction and the x

direction in the plane of the simulation domain, respectively. For an initial equilibrium, the initial pressure distribution is prescribed as

$$p(x) = \frac{B_0^2}{2}(\beta + 1) - \frac{B(x)^2}{2}, \tag{4.11}$$

where β is the ratio of gas pressure to magnetic pressure at the simulation boundaries ($x = \pm L_x$). The initial plasma velocity is set to zero everywhere in the simulation box. Different initial density profiles are used for the three simulation cases below.

For $t \geq 0$, driven boundary conditions are imposed on the two boundaries at $x = \pm L_x$. The incoming speed of the plasmas at the driven boundaries are perpendicular to the driven boundaries and are specified by

$$v_{in}(y) = \begin{cases} \frac{4}{3}(1 - y/L_y)v_{in0}, & \text{if } y > L_y/4; \\ v_{in0}, & \text{if } -L_y/4 < y < L_y/4; \\ \frac{4}{3}(1 + y/Ly)v_{in0}, & \text{if } y < -L_y/4, \end{cases} \tag{4.12}$$

where v_{in0} denotes the incoming speed at the center of the driven boundaries. In addition, on the driven boundaries, the plasma mass density, pressure, and magnetic field Poynting flux are kept at their initial values. The boundaries at $y = \pm L_y$ are "free," meaning that the derivative of each quantity in the boundary normal direction is set to zero. Since only symmetric cases are considered, the actual calculation is conducted in one quadrant of the domain and, therefore, the boundaries at x=0 and $y = 0$ are symmetric ones. The grid points used in this calculated quadrant are 52×72.

Three simulation cases are presented in the following. For Case A and Case B, a large β value is used. In Case C, a small β and a small initial B_y are used. Results from Case A and Case B may be applicable to the magnetopause, while Case C is applicable to the magnetotail current sheet. For all simulation cases in section 4.4, the scales of the simulation domain are chosen as $L_x = 5a$ and $L_y = 28a$.

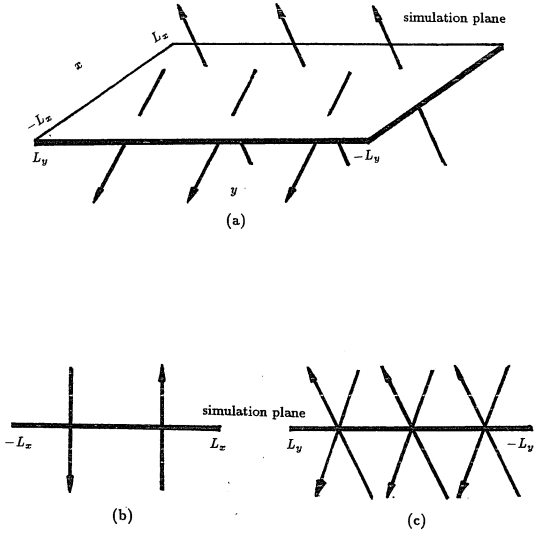

Figure 4.10 Initial sheared magnetic configuration in the simulation. (a) A 3-D perspective view, where the vectors (heavy straight lines with arrow heads) are magnetic field vectors on the two sides of the current sheet and the simulation plane is the x-y plane; (b) configuration viewed in the positive y direction; (c) configuration viewed in the positive x direction.

Case A

In Case A, the magnetic field across the current sheet has a large antiparallel component. This case corresponds to a large southward component in the interplanetary magnetic field. For the initial magnetic field configuration expressed by (4.3), $B_{0y}/B_{0z} = 0.27$ or, equivalently, $\theta_L = 130°$ is chosen. The inflow speed $v_{in0} = 0.2V_{A0}$ and $\beta = 1$ is used. The initial density profile is specified as

$$\rho(\boldsymbol{x}) = p(\boldsymbol{x})/T_0 \tag{4.13}$$

where T_0 is a constant. Hence, the distribution in (4.13) is one with a constant temperature.

Under the driven boundary conditions, enhancement of B_y in the current sheet is observed as time goes on. Figures 4.11*a* and *b* are the 3-D profile of B_y in the simulation plane (x-y plane) at times $t = 0$ and $60t_A$, respectively. At $t = 0$, B_y is uniformly distributed in the simulation domain. By $t = 60t_A$, an enhanced B_y region has appeared in the central area of the current sheet.

Figure 4.12 shows the plasma flow pattern and the corresponding magnetic field at $t = 60t_A$. The magnetic field is highly compressed and enhanced in the current sheet. While the magnetic flux is being piled up in the current sheet region, the incoming plasmas are seen to be squeezed out of the simulation box approximately along the magnetic field lines. Note that in the present 2-D simulation, the incoming magnetic flux cannot be convected outward perpendicular to the simulation plane. In the actual situation, the magnetic field lines may be convected outward in the z-direction. The effect of the convection in the z-direction will impose an upper limit on the pile-up time τ_p. This 3-D effect will be discussed later.

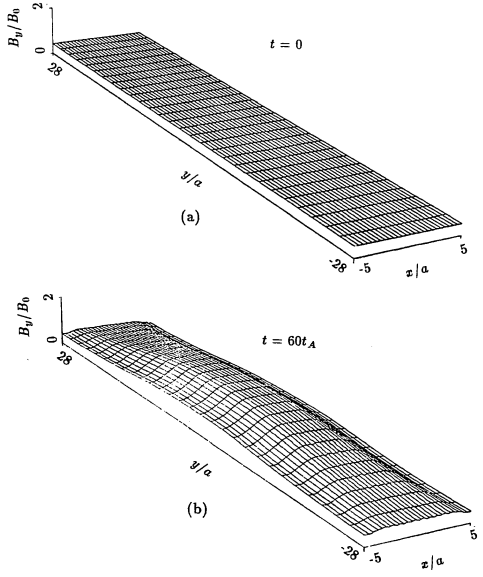

Figure 4.11 3-D B_y profiles in the y-x plane for Case A (a) at time $t = 0$ and (b) at $t = 60t_A$.

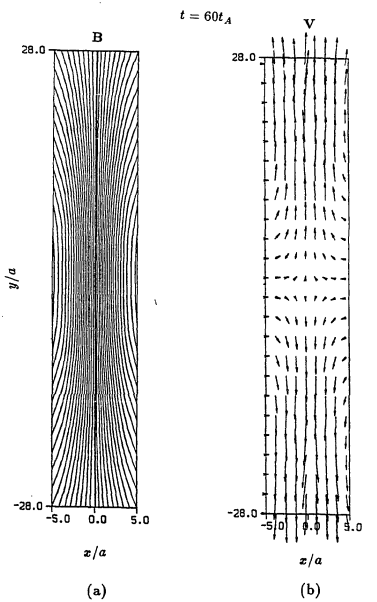

Figure 4.12 Magnetic field configuration and plasma flow patterns in the x-y plane at $t = 60t_A$ for Case A. (a) Magnetic field lines. (b) Velocity vectors (the direction of the arrows is the direction of the velocity vectors and the length of the arrows is proportional to the magnitude of the velocity vectors).

Figure 4.13 shows the hodogram of the magnetic field in the y-z plane and the corresponding B_y component across the central line ($y = 0$) of the simulation box at $t = 60t_A$. The hodogram in Figure 4.13a shows a "bulge-out" feature similar to that observed by ISEE satellites [*Russell and Elphic*, 1978] for a tangential magnetopause. From Figure 4.13, it is seen that at the center of the simulation region, B_y reaches a value almost twice the value at the incoming boundaries.

Figure 4.14a shows the density profile at $y = 0$ for $t = 0$ and $t = 60t_A$. It is interesting to note in Figure 4.14a that the plasma density at the center of the current sheet has been depleted considerably by $t = 60t_A$. The peak density at $t = 0$ is $1.8\rho_0$, which is reduced to $1.3\rho_0$ by $t = 60t_A$ (a decrease of $\sim 29\%$). This depletion process in the region near the dayside magnetopause has been predicted and studied by *Lees* [1964] and *Zwan and Wolf* [1976]. They attributed the depletion to the squeezing of solar wind plasma along the interplanetary field lines in the absence of magnetic reconnection.

Case B

Case B is used to demonstrate that the squeezing and depletion of plasma in the current sheet region is a fundamental process independent of the initial density distribution. In Case B, all the parameters are the same as in Case A except that the initial density profile is changed to

$$\rho(x) = \rho_0. \tag{4.14}$$

Similar to Case A, an enhancement of the B_y component is observed in Case B. The magnetic field hodogram and profiles of B_y are also similar to those in Case A both quantitatively and qualitatively. Figure 4.14b shows the density profiles at $y = 0$ for $t = 0$ and $t = 60t_A$. The depletion of plasmas in the current sheet again is clearly seen.

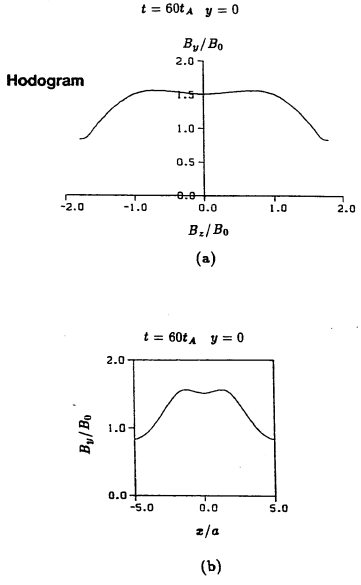

Figure 4.13 (a) Hodogram of magnetic vector across the current sheet at $y = 0$ and $t = 60t_A$ in Case A; (b) B_y profile across the current sheet at $y = 0$ and $t = 60t_A$ in Case A.

The plasma density decreases from ρ_0 to $0.75\rho_0$ at $x = 0$ by $t = 60t_A$ (a reduction of 25%).

Case C

In Case C, the B_y enhancement process is simulated in a situation similar to that in the magnetotail neutral sheet region. For Case C, the initial density profile is

$$\rho(x) = \rho_0[1 + 2sech^2(x/a)]. \tag{4.15}$$

Equation (4.15) gives a density ratio of ~1:3 at $x = \pm 5a$ and $x = 0$, since the plasma density in the magnetotail neutral sheet is usually higher than plasma density in the lobe region. A small β (=0.1) is used . In addition, since the lobe B_y component is observed to be very small, a large initial angle between the two magnetic vectors at each side of the current sheet is used: $B_{0y}/B_{0z} = 0.05$ or $\theta_L = 174^o$.

Figure 4.15 shows the the hodogram of the magnetic vector and the B_y profile across the neutral sheet (going from north to the south) at $t = 60t_A$ and $y = 0$ for Case C. The reader is reminded that in the magnetotail situation, the x-axis in the simulation is in the southward direction and the y-axis is in the dawn-dusk direction. It is found in Case C that the relative enhancement of B_y in the current sheet as compared to the boundary B_y is larger than that in both Case A and B (dayside situation). This difference can be clearly seen by comparing B_y profiles of Case A and Case C at $t = 60t_A$ (Figure 4.13*b* and Figure 4.15*b*). Let R denote the ratio of B_y in the current sheet to B_y outside the current sheet (near the simulation boundaries $x = \pm 5a$). Then at $t = 60t_A$, $R \sim 4$ for Case C and $R \sim 2$ for Case A. Relative to the initial value, B_y also shows a larger percentage of enhancement in Case C than in Case A. In Case C, the initial large angle $\theta_L = 174^o$ corresponds to a small $B_y = 0.05B_0$. By $t = 60t_A$ the peak value of

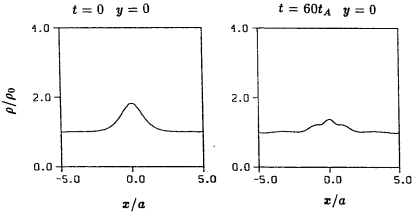

Figure 4.14 Plasma density profiles across the current sheet at $y = 0$ and $t = 0, 60t_A$ in Case A and Case B (a) Case A; (b) Case B.

B_y in the current sheet increases to 0.5, a 900% increase. On the other hand, in Case A, the initial value of B_y with $\theta_L = 130^o$ is $\sim 0.4B_0$ whereas the peak value of B_y at $t = 60t_A$ (Figure 4.13*b*) is $\sim 1.6B_0$, only a 300% increase.

The hodogram in Figure 4.15*a* is also different from hodograms of large β cases. The hodogram in Figure 4.15*a* indicates that when B_y increases, B_z remains almost unchanged.

4.4.3 B_y enhancement at the dayside magnetopause and in the magnetotail neutral sheet

The earth's dayside magnetopause is a boundary that separates the external solar wind flow from the geomagnetic fields (for a review of solar wind-magnetosphere interaction, see *Spreiter and Alksne* [1969]). The constant solar wind flow carries the interplanetary magnetic fields (IMF) towards the dayside magnetopause region. In the case of a tangential discontinuity magnetopause boundary, the IMF flux will be convected by the divergent solar wind flow sideward over the magnetosphere surface away from the dayside magnetopause region. Meanwhile, since the gas pressure of the solar wind flow is much greater than the magnetic pressure of the IMF in the region immediately in front of the magnetopause surface, the interplanetary magnetic field is compressed against the magnetopause surface, leading to a pile-up of IMF flux. In the case of an IMF with a finite B_y (dawn to dusk) component, the pile-up will lead to an increase of the B_y intensity near or in the magnetopause current sheet. However, the increase in B_y intensity due to compression or pile-up is regulated by the convection time τ_c of the IMF flux moving away from the subsolar point region out of the magnetopause region. If τ_p is taken as the characteristic time for the IMF flux pile-up, a significant increase in B_y in the magnetopause current sheet would require that τ_p be less than τ_c.

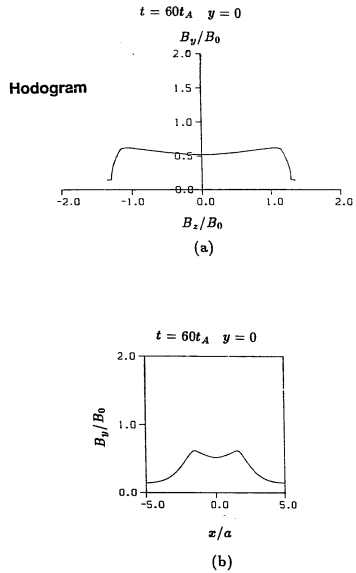

Figure 4.15 (a) Hodogram of magnetic vector across the current sheet at $y = 0$ and $t = 60t_A$ in Case C; (b) B_y profile across the current sheet at $y = 0$ and $t = 60t_A$ in Case C.

In Case A and Case B of the simulation, B_y in the current sheet is observed to increase to a value more than twice as high as the ambient B_y in 50-60 Alfvén transit times (t_A) with an inflow speed of $0.2V_{A0}$. At the dayside magnetopause, the Alfvén transit time calculated on the basis of the magnetopause current sheet thickness and local Alfvén speed can be estimated to be ~5 sec (based on a magnetic field value $B \sim 30$ nT, plasma number density $n \sim$ 5-20 cm^{-3}, and a current sheet thickness of $\sim$ 200-500 km). If the convection speed of the IMF flux around the magnetopause is taken to be 100-200 km/sec, it would take 300-600 sec to travel a distance of 10 R_E (where R_E is the earth radius), the scale size of the dayside magnetopause. Therefore, it is possible that a significant B_y enhancement can occur in the dayside magnetopause. This enhancement of B_y will explain naturally the "bulge-out" feature in the observed hodograms of magnetic vectors for a tangential discontinuity magnetopause [*Russell and Elphic*, 1978]. It should be noted that the data presentation in Russell and Elphic is based on the boundary normal coordinate system (such representation of magnetic variations in local coordinates was pioneered by *Sonnerup and Cahill* [1967] through the use of the minimum variance technique). A detailed comparison requires the transformation of the present simulation data into the boundary normal coordinates. However, in the case of a large southward component of the IMF, the boundary normal coordinate system nearly coincides with the solar-magnetosphere coordinate system near the subsolar point. Hence it is reasonable to believe that the observed B_y enhancement in the magnetopause current sheet may be the consequence of the compression of the IMF against the magnetopause surface in the absence of magnetic reconnection.

Simulation Case C is a case with a small β ($\beta = 0.1$) which is applicable to the magnetotail. Case C shows that the B_y enhancement observed in the magnetotail neutral sheet may also result from the same pile-up and squeeze process as suggested above. *King*'s [1977] results (see section 4.2) suggested a penetration of 50% of IMF

B_y into the neutral sheet whereas *Fairfield*'s [1979] analysis (see section 4.2) indicates a penetration of 13% of IMF B_y into the whole magnetotail. From their results, it is expected that the ratio of B_y in the neutral sheet to that in the lobe region should be $\sim$ 2–3. In Case C, this ratio is about 4 at $t = 60t_A$ (see Figure 4.15*b*). If $t_A \simeq 10s$ is used (estimated based on the neutral sheet half thickness $a \simeq 10^4$ km and Alfvén velocity near the tail neutral sheet $V_{A0} \simeq 1000$ km/s), Case C suggests that it takes less than 10 minutes ($60t_A$) to reach the observed ratio of enhancement in B_y. In addition, compared to the dayside magnetopause situation, the convection motion of the magnetic field lines in the magnetotail is negligible or the convection characteristic time τ_c is large. This fact also favors the pile-up and squeeze mechanism for B_y enhancement in the tail neutral sheet.

Finally, note that the inflow speed at the incoming boundary for all the above three simulation cases is $v_{in0} = 0.2V_{A0}$. The magnitude of this inflow speed is appropriate for the dayside magnetopause situation but may be a few times larger than the real convection flow speed in the magnetotail corresponding to the dawn-dusk convection electric field. Hence, the actual pile-up of B_y in the magnetotail neutral sheet may take longer than estimated above.

4.5 Enhancement of Core Field Associated With Flux Transfer Events and Plasmoids In the Magnetotail

4.5.1 Mechanism

To explain the origin of strong core fields often observed in flux transfer events (FTEs) at the dayside magnetopause and in plasmoids in the magnetotail, a possible mechanism is proposed in the following:

In section 4.2, it was pointed out that an enhanced B_y component is often observed in the magnetopause and magnetotail current sheets and the simulation presented in section 4.4 shows that such enhancement of the B_y component may be a direct result of the driven process in the absence of magnetic reconnection, or may be the result of the penetration of the interplanetary magnetic field B_y component into the dayside magnetopause and the penetration of the lobe B_y component into the magnetotail neutral sheet. Suppose that the reconnection is initiated in such a current sheet with an enhanced B_y component. The initial B_y flux in the current sheet will be redistributed due to the breakup of the current sheet by magnetic reconnection. The simulation presented below shows that the redistribution of the B_y flux proceeds in such a way that B_y flux at the reconnection point is removed and lumped into the magnetic island or plasmoid (a helical flux tube in the 3-D configuration). This would lead to an enhanced B_y in the magnetic island or flux tube and, at the same time, a reduced B_y around the reconnection point. Therefore, B_y in the magnetic island (or flux tube) will be greater than in the surrounding region due to such redistribution. A further enhancement of the core field (B_y) can be obtained by the squeezing of plasma out of the helical magnetic flux tube along the tube axis or the core field. The squeezing is caused by the inward pinch produced by the azimuthal component of magnetic flux tubes. The escape of plasma along the magnetic flux tubes will reduce the thermal pressure inside the flux tubes, and, consequently, will facilitate the gathering of core fields towards the center of the tubes, eventually further increasing the intensity of the core field.

4.5.2 Simulation

Again a 2-D compressible MHD simulation is used (the governing equations and finite

differencing scheme are identical to that in section 4.4). In the present 2-D simulation, only the first part of the proposed process (the redistribution of the B_y flux due to magnetic reconnection) can be simulated. The further increase of the core field because of the pinch effect of the magnetic flux tube may need a 3-D simulation.

In the simulation presented in this section, the initial anti-parallel magnetic field component is in the simulation plane so that magnetic reconnection can occur. The simulation domain is again a rectangular box but, in contrast to that in section 4.4, it is set in the x-z plane (extending from $-L_x$ to L_x and from $-L_z$ to L_z). In the case of the dayside magnetopause, the x-axis is in the anti-sunward direction and the z-axis in the northward direction. In the case of magnetotail, the x-axis is in the northward direction and the z-axis is in the earthward direction.

To illustrate the proposed mechanism, an initially sheared magnetic field configuration with an enhanced B_y in its central current sheet is set up. Specifically, the following initial magnetic field configuration is used in the simulation:

$$\mathbf{B}(x) = B_{0z} tanh(x/a)\hat{\mathbf{z}} + B_{0y}(x)\hat{\mathbf{y}} \tag{4.16}$$

where a is the half-thickness of the current sheet, B_{0z} is a constant, and $B_{0y}(x) = rB_0[1 - (B_{0z}tanh(x/a)/B_0)^2]^{1/2}$ where r is a parameter and B_0 is the normalization unit. Besides B_0, the normalization conventions here are the same as in section 4.4. Equation (4.16) represents a current sheet configuration in which the vector $\mathbf{B}$ rotates across the current sheet. For $r = 1$, the intensity of the magnetic field is a constant B_0 independent of x; for $r < 1$, the intensity of the magnetic field is smaller at the center of the current sheet. In either case, B_y is enhanced at the center of the current sheet.

Initially, the pressure distribution is given by (4.11) and the density distribution by (4.14) for Cases D and F and by (4.15) for Case E. Plasma velocity is set to zero

everywhere. The resistivity used is

$$\eta(x,z,t) = \begin{cases} \eta_0 + \eta_1(x,t) + \alpha(|j_y| - j_c)^2, & \text{if } |j_y| > j_c; \\ \eta_0 + \eta_1(x,t), & \text{otherwise,} \end{cases} \tag{4.17}$$

with

$$\eta_1(x,t) = 0.3e^{-x^2/a^2}e^{-(z-z_p)^2/a^2}e^{-(t/\tau)^2} \tag{4.18}$$

In (4.17), η_0 is a constant background resistivity, j_y is the y-component of current density $\mathbf{j}$, j_c is the value of the critical current density for the enhancement of nonlinear resistivity, and α is a constant. In (4.18), z_p is the position in the center of the current sheet ($x = 0$) where an initial perturbation is given and τ is the decay time for the initial perturbation. Magnetic reconnection is initiated at $x = 0$ and $z = z_p$ by the time-dependent localized resistivity enhancement η_1 expressed in (4.17).

Simulation boundaries at $x = L_x$ and $z = L_z$ are free ones where the derivatives of each quantity with respect to the boundary normal are set to zero. Again only symmetric cases are simulated and hence boundaries at $x = 0$ and $z = 0$ are symmetric ones. In the quadrant simulated (from $x = 0$ to $x = L_x$ and $z = 0$ to $z = L_z$), 52×72 grid points are used.

Three cases are run to study the B_y distribution associated with: (1) magnetic island (with large β); (2) magnetic island (with small β); and (3) bursty reconnection. The common parameters used for the following three simulation cases are $\eta_0 = 0.01$, $\tau = 20t_A$, $j_c = 1.5$, $\alpha = 10$, and $L_x = 5a$

Case D: Magnetic island with large β

In Case D, $\beta = 1$, $\theta_L = 130^o$ (or $B_{0z}/B_{0y}(x = \pm L_x) = 2.15$), $r = 1$, and $L_z = 28a$. Figure 4.16 shows the initial magnetic field configuration and B_y profile in the x-z plane for Case D.

At $t = 0$, an enhancement in resistivity (see (4.17)) is turned on at $z_p = L_z/2$ and $x = 0$ to trigger the reconnection at that point. By symmetry, a magnetic island centered at $z = 0$ will be formed. By $t = 49t_A$, the formed magnetic island has grown to a large size as a result of the continuous reconnections. Figure 4.17 shows the magnetic field lines in the x-z plane and the corresponding B_y profile in the same plane at $t = 49t_A$. It is seen that the initially uniformly distributed B_y in the current sheet is now either lumped into a magnetic island region or has been carried away by the reconnected field lines out of the simulation box. The process results in a region within the magnetic island where B_y is larger than it is in the surrounding region. Figure 4.18 shows the B_y profiles along different straight lines across the simulation box for $t = 49t_A$. Figure 4.18 shows that the maximum B_y value ($\sim 1.05B_0$) in the magnetic island is almost the same as the initial B_y ($= B_0$) in the current sheet, and the B_y value near the reconnection point (at $z \sim 18a$) is reduced to $0.55B_0$ (from the initial value of B_0). Thus, the 2-D reconnection process functions mainly to redistribute the initial B_y flux and does not lead to significant further enhancement of B_y. Therefore, the enhancement of B_y in the 2-D magnetic island case can be considered as a three-step process: (1) the enhancement of B_y in the current sheet due to driven processes, (2) the redistribution of the enhanced B_y flux by magnetic reconnection, and (3) further enhancement of B_y by the pinch of the flux tube (3-D effect).

Case E: Magnetic island with small β

Case E simulates the situation with small $\beta = 0.1$. This case may be applicable to the B_y enhancement in the magnetotail plasmoids. Note that the B_y component observed in the magnetotail lobe region is usually small. Therefore, in Case E the initial B_y component at the simulation boundaries $x = \pm L_x$ is set to a value smaller than that

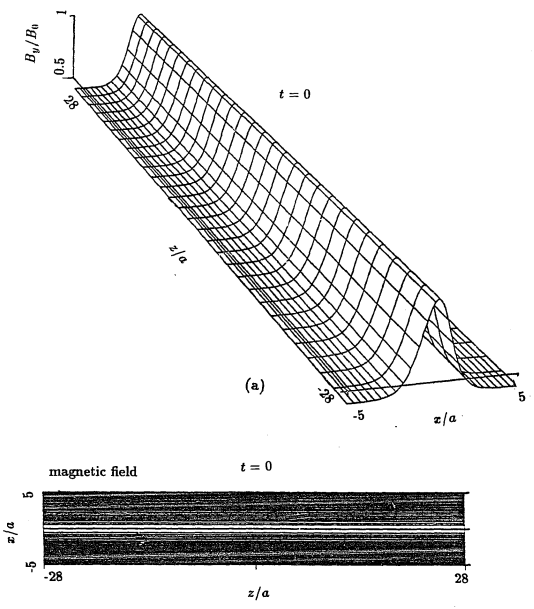

Figure 4.16 (a) Initial B_y profile in the x-z plane (simulation plane) for Case D; (b) initial magnetic field configuration in the x-z plane for Case D.

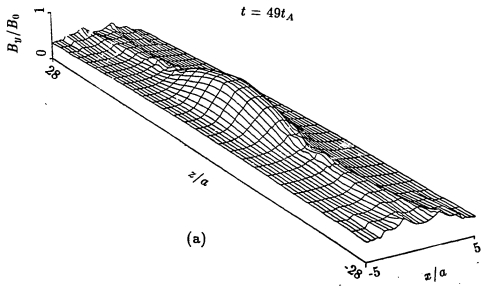

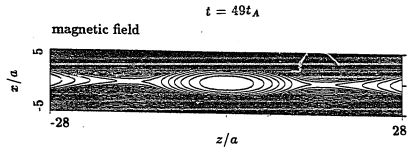

(b)

Figure 4.17 (a) B_y profile in the x-z plane at $t = 49t_A$ in Case D; (b) magnetic field configuration in the x-z plane at $t = 49t_A$ in Case D.

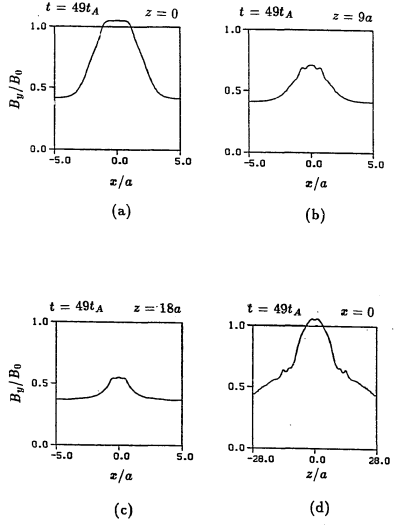

Figure 4.18 Profiles of B_y across the simulation box at $t = 49t_A$ in Case D (a) along line $z = 0$; (b) along line $z = 9a$; (c) along line $z = 18a$; (d) along line $x = 0$.

in Case D. $\theta_L = 168°$, or equivalently $B_{0z}/B_{0y}(x = \pm L_x) = 9.5$ is used (the definition of θ_L is the same as in section 4.4). Furthermore, since in the magnetotail the thermal pressure is higher in the neutral sheet than in the lobe region, $r = 0.3$ is chosen in (4.16) for this case to ensure a pressure peak in the current sheet. All other parameters are the same as in Case D.

Figure 4.19 shows the magnetic field configurations and B_y profile in the x-z plane at $t = 50t_A$. As in Case D, an enhanced B_y region is found within the magnetic island (or plasmoid). Therefore, under the magnetotail conditions, the same driven and redistribution processes can also lead to the observed enhanced B_y in the plasmoid.

Case F: Bursty reconnection

As proposed by *Scholer* [1988*a*] and *Southwood et al.* [1988], bursty single X-line reconnection caused by a sudden surge in the reconnection rate around a point in the current sheet may lead to the formation of a bulge-shaped magnetic structure. Scholer and Southwood et al. have used this model to explain some features of flux transfer events at the dayside magnetopause. In addition, *Scholer* [1988*b*] proposed that the generation of the strong core field in flux transfer events can be attributed to a sweeping up of the guiding field by the poleward-moving magnetic field loops in their model (see review in section 4.3).

The simulation result presented below will show that the enhanced B_y associated with the bursty reconnection could also result from the same redistribution mechanism as proposed earlier in this section.

In Case F, choose $\beta = 1$, $\theta_L = 130°$, $r = 1$ with all other parameters the same as in Case D. To initiate the bursty reconnection, a resistivity enhancement of the form given in (4.18) is applied at $z = 0$ and $x = 0$ at $t = 0$.

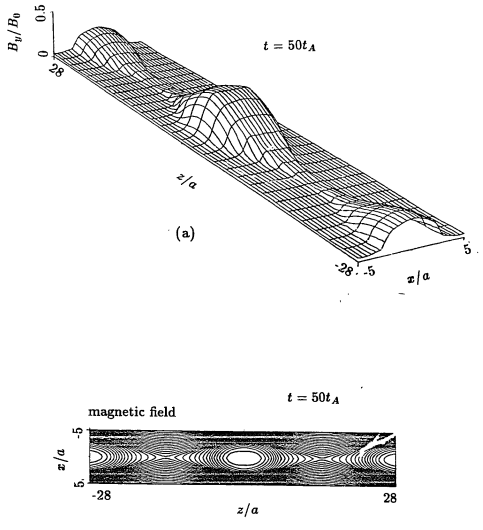

Figure 4.19 (a) B_y profile in the x-z plane at $t = 50t_A$ in Case E; (b) magnetic field configuration in the x-z plane at $t = 50t_A$ in Case E.

Figure 4.20 shows the magnetic field lines and the B_y distribution in the x-z plane at $t = 52t_A$ for Case F (only the $z > 0$ part of the simulation domain is shown). Figure 4.20 shows that, as in the magnetic island cases, the B_y flux is removed from the reconnection point (X point) located at $z = 0$ and $x = 0$ and lumped into the bulge-shaped magnetic field region, while the B_y distribution in the slightly perturbed current sheet region (approximately $z > 3L_z/4$) is only slightly affected. The region with an enhanced B_y is outlined by the bulge-shaped magnetic field region together with the unperturbed current sheet region. The whole enhanced B_y region is moving outward in the z-axis direction at a speed of $\sim 0.6V_{A0}$ along with the bulge-shaped magnetic field region. The maximum value of B_y in the enhanced region is $\sim B_0$ which is the initial peak value of B_y in the current sheet. However, at the reconnection site (X-line) B_y reduces to $0.5B_0$ from the initial $B_y = B_0$ at the same position. Outside the bulge-shaped magnetic field region and the remaining current sheet region, B_y maintains values from 0.4–$0.5B_0$, while the initial B_y outside the current sheet is $\sim 0.42B_0$ with $\theta_L = 130^o$ and $r = 1$. Therefore, the same redistribution mechanism can also lead to enhanced B_y in the magnetic bulge produced in a 2-D bursty reconnection.

4.5.3 Core field enhancement in magnetic flux tubes

As reviewed in section 4.2, observations suggest that the dayside magnetic flux tubes associated with flux transfer events (FTEs) often reveal a strong core field. *Scholer* [1988*b*] (see section 4.3) has proposed a mechanism to explain the origin of such strong core fields in the framework of a recently proposed FTE model: bursty reconnection [*Southwood et. al*, 1988; *Scholer*, 1988*a*]. Scholer argued that the poleward convection of the open magnetic field loops produced in the bursty reconnection will sweep magnetic field lines in the magnetopause, leading eventually to the observed strong core

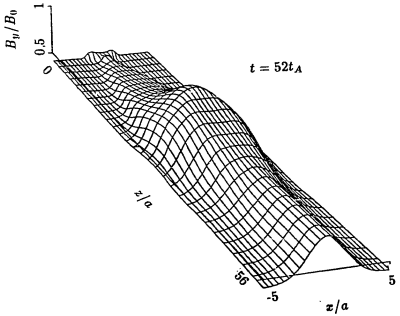

(a)

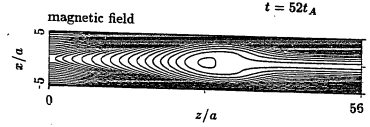

(b)

Figure 4.20 (a) B_y profile in the x-z plane at $t = 52t_A$ in Case F; (b) magnetic field configuration in the x-z plane at $t = 52t_A$ in Case F.

field. However, the strength of the core field in Scholer's mechanism depends on the longitudinal extent of the loop structure and the distance traveled by the loops. For example, as estimated by Scholer, to generate a core field of 60 nT, a magnetopause magnetic field of 20 nT has to be swept up over a distance of 6 R_E. Therefore, Scholer's mechanism will not be able to account for the enhanced core field observed in the low-latitude FTEs. On the other hand, the mechanism proposed here does not have latitude dependence and it can account for the enhanced core field found in low-latitude as well as high-latitude FTEs. In addition, Scholer's mechanism can only apply to open magnetic flux loops while the mechanism suggested here is expected to operate in either the open magnetic flux loop situation or the magnetic flux tube situation.

For the existence and, sometimes, the enhancement of the B_y observed in the magnetotail plasmoids, Case C and Case E of our simulation indicate that: (1) the B_y component can penetrate into the neutral sheet from the lobe region under driven conditions and this penetration can further lead to enhanced B_y in the neutral sheets, and (2) the plasmoid formed in such a neutral sheet has an enhanced B_y. Therefore, if the B_y in the lobe is due to the penetration of IMF B_y, our simulation would naturally suggest that the sign of B_y in the plasmoids is the same as IMF B_y, as is observed, and, most likely, B_y in the plasmoids will be larger than the ambient B_y (in the lobe or near the neutral line).

4.6 Discussion and Conclusion.

The MHD simulation conducted in this chapter is only a two-dimensional one. A three dimensional configuration may modify some of the results obtained in this chapter. In B_y enhancement in the current sheet, as has been discussed in section 4.4,

the convective motion of magnetic fields may compete with the magnetic flux pile-up process. Consideration of the convection is especially necessary for the dayside situation.

For the core field enhancement in magnetic flux tubes at the dayside magnetopause and in the magnetotail, it is expected that the inward pinch produced by the azimuthal component of magnetic flux tubes may contribute to further B_y enhancement. In the 2-D case, the effectiveness of the pinch process alone in the enhancement of B_y has been simulated by us (not presented here). It was found in this simulation that, in a current sheet with a finite but not enhanced B_y, the formation of a magnetic island can lead to only a 10% to 20% enhancement of B_y in the island region. Similar small B_y enhancement in the magnetic island region was observed in the particle simulation by *Allen and Swift* [1989]. Thus, the proposed enhancement of B_y through a pinch effect of magnetic flux tubes remains to be tested in a 3-D simulation. The small enhancement of B_y observed in our 2-D simulation may be attributed to the pressure build-up in the magnetic island, which will then prevent effective penetration of B_y into the core of the magnetic island, while in a 3-D situation, the escape of plasma along the flux tube may reduce considerably the pressure build-up.

In conclusion, the major results obtained in this chapter are:

(1) In the absence of magnetic reconnection, a pile-up of magnetic fields will occur in the current sheet under the driven condition, while the plasmas are being squeezed out along field lines. In the presence of a finite initial B_y, the pile-up and squeeze process will lead to a B_y enhancement in the current sheet.

The result can apply to the dayside magnetopause to explain the "bulged-out" feature observed in the hodogram of the magnetic field, and to the magnetotail to explain the presence of a larger dawn-dusk magnetic field component in the neutral sheet than in the lobes.

(2) In a current sheet with an initially enhanced B_y, magnetic reconnection can redistribute the initial B_y flux, leading to enhanced B_y regions associated with magnetic islands or bulge-shaped magnetic structures (in the case of the bursty reconnection).

The result can be used to explain the observed strong core fields associated with dayside flux transfer events and the presence, and sometimes the enhancement, of the dawn-dusk component of the magnetic field in magnetotail plasmoids.

Chapter 5. Summary and Conclusions

The importance of the dayside reconnection have been recognized for many years since *Dungey*'s [1961] earliest open magnetosphere model. The Dungey model was later further elaborated by *Levy et al.* [1964], who predicted the existence of a rotational discontinuity at the dayside magnetopause and the associated high-speed plasma jets. Both Dungey and Levy et al.'s models are characterized by the single X-line quasi-steady reconnection at the subsolar point of the magnetopause. The fact that the predicted high-speed plasma jets [*Levy et al.*, 1964] associated with dayside reconnection were not frequently observed led to some doubts about Dungey and Levy et al.'s hypothesis of a steady-state reconnection process at the dayside magnetopause. The observation of flux transfer events (FTEs) in 1978 by ISEE satellites indicated that the dayside reconnection is unlikely to be a steady-state process. Hence, in contrast to the early steady-state and large-scale models, new dayside reconnection models proposed to explain the observations of FTEs emphasize the sporadic and localized aspects of the reconnection process, notably, the Russell-Elphic patchy reconnection model, the Lee-Fu multiple X-line reconnection model, and the single X-line bursty reconnection model. Nevertheless, due to the lack of global observational data, the dayside reconnection configuration remains to a certain degree a mystery. The objective of the work reported in this thesis is to lessen the degree of mystery by a study of the dayside reconnection processes through computer simulations.

First, global patterns of the dayside reconnections were studied in Chapter 2 using a global two-dimensional incompressible magnetohydrodynamic code. Various patterns of magnetic reconnection were observed in the simulation depending on three parameters:

the magnetic Reynolds number R_m, the current-dependent anomalous resistivity, and the solar-wind Alfvén Mach number M_{Asw}.

When the magnetic Reynolds number is small, the Dungey-type single X-line quasi-steady reconnection is observed; when the magnetic Reynolds number is large (> 200), dayside reconnection occurs along multiple X lines and as a result, magnetic islands are formed. For a large magnetic Reynolds number, a long and thin dayside magnetopause current layer can be formed. In the presence of a current-dependent anomalous resistivity, the onset of a tearing instability can lead to the formation and poleward convection of magnetic islands as predicted in the Lee-Fu model. It is demonstrated that the formation and poleward convection of the magnetic islands in the Lee-Fu type of multiple X line reconnection can indeed generate the FTE-like magnetic field and plasma signatures. Hence, the Lee-Fu type reconnection may be a potential candidate of FTEs. In the presence of a large solar-wind Alfvén Mach number, the reconnection sites tend to shift to higher latitude region. Such a dependence of reconnection sites on solar-wind Alfvén Mach number is qualitatively consistent with the laboratory experiment of *Podgorny et al.* [1978]. The bursty single X line reconnection process [*Scholer*, 1988a; *Southwood et al.*, 1988], another FTE model, is also simulated. Therefore it is seen from the simulations that dayside reconnection patterns are diversified. However, due to the large magnetic Reynolds number at the dayside magnetopause and the observed long and thin magnetopause current layer, multiple X-line reconnection may prevail.

The global simulation in Chapter 2 is only a two-dimensional incompressible one. Some aspects of the dayside reconnection related to the compressibility of the plasma may have not been revealed. The dayside magnetopause is a current layer separating two distinct magnetized plasma regions, the magnetosheath and the magnetosphere. Typically, the plasma density in the magnetosheath is an order of magnitude larger than

the plasma density in the magnetosphere while the magnetic field strength on the magnetospheric side is usually higher. In addition, the plasma β on the magnetosheath side varies considerably from time to time. Both the asymmetry in plasma density and the finite plasma β may affect the dayside reconnection. However, these two effects on the dayside reconnection cannot be studied in the incompressible MHD simulation presented in Chapter 2. For this reason, a local two-dimensional compressible MHD simulation of the dayside reconnection was carried out in Chapter 3.

Chapter 3 presents results from the simulation of a spontaneous magnetic reconnection process in a plane current sheet configuration. The simulation was based on a two-dimensional compressible MHD code. Under the asymmetric conditions typical of the dayside magnetopause, the reconnection layer was found to be bounded by an intermediate shock on the magnetosheath side and a weak slow shock on the magnetospheric side in the presence of a medium or low plasma β in the magnetosheath. This type of structure of the dayside reconnection layer is believed to be caused mainly by the large asymmetry in plasma density on the two sides of the dayside magnetopause. The reconnection layer structure of this type is quite different from the reconnection layer structure found in simulation cases with a symmetric configuration. In a symmetric situation, the reconnection layer was bounded by a pair of slow shocks as predicted in Petschek's model, which may be more applicable to the magnetotail reconnection process. In addition to the plasma density asymmetry, the effect of the plasma β on the structure of the dayside reconnection layer was found to be also significant. When β in the magnetosheath is large, the discontinuity structure in the dayside reconnection layer became less evident.

The simulations presented in Chapters 2 and 3 are purely two-dimensional: the magnetic field component perpendicular to the simulation plane, the noon-midnight meridian plane, is zero. In the interplanetary magnetic field, the existence of a B_y

component is common. Hence, the magnetic fields on the two sides of the magnetopause current layer are usually non-coplanar. The existence of the B_y component may modify the dayside reconnection layer structure found in the simulations in Chapter 2. In the case of non-coplanar magnetic fields on the two sides of the magnetopause, rotational discontinuities are required to rotate the magnetosheath field and the geomagnetic field onto the same plane. In this case, it is speculated that the edge of the dayside reconnection layer on the magnetosheath side may consist of a rotational discontinuity and a slow shock lumped together instead of an intermediate shock. Another property of the dayside reconnection in the presence of a finite B_y is the enhanced B_y in the magnetic island or magnetic flux tubes in a 3-D situation. Satellite observations have provided evidence that the core or guide fields in the magnetic flux tubes associated with the flux transfer events at the dayside magnetopause are often enhanced. This latter consequence of the existence of a finite B_y in the IMF in relation to the dayside reconnection was the subject of Chapter 4.

In Chapter 4, a mechanism was proposed to explain the observed core magnetic field enhancement in magnetic flux tubes associated with FTEs. The proposed mechanism consists of three steps. First, under driven conditions and in the absence of magnetic reconnection, the pile-up of the magnetic field and depletion of plasma can lead to enhanced B_y in the dayside current layer. Note that an enhanced B_y in the dayside current layer is also an observational fact. Second, the onset of the magnetic reconnection in such a current sheet will redistribute the B_y flux in the current sheet, leading to an enhanced B_y (or core field) region within the magnetic flux tubes. Finally, further enhancement of the core field can be achieved by the inward pinch of the magnetic flux tubes due to the Maxwell stresses of the azimuthal magnetic field component.

The two-dimensional compressible MHD simulation conducted and presented in Chapter 4 demonstrated and supported the proposed mechanism. The results can also be applied to the magnetotail to explain the similar B_y enhancement observed in the tail neutral sheet and plasmoids.

In summary, the present study provides a global criterion for the occurrence of the single X-line quasi-steady reconnection or the multiple X-line time-dependent reconnection at the dayside magnetopause. The boundary structure associated with reconnections at the dayside magnetopause is also examined. In addition, a mechanism is proposed to explain the observed B_y enhancement in the dayside current sheet and magnetic flux tubes.

Appendix . Difference Scheme For Compressible MHD Equations

It can be shown that the set of governing compressible MHD equations used in Chapter 3 (eqs.(3.1)-(3.4)) can be easily rewritten into the following conservation form

$$\frac{\partial U}{\partial t} + \frac{\partial F}{\partial x} + \frac{\partial G}{\partial z} = 0, \tag{A.1}$$

where $U = (\rho, \rho\mathbf{v}, \mathbf{B}, \epsilon)$ and F and G are the corresponding fluxes in the x and z directions, respectively. For the compressible MHD equations of the form as in (A.1), the following two-step Lax-Wendroff scheme is used [*Lapidius*, 1967]. The *first step* of the two-step scheme is:

$$\begin{aligned} U^{n+\frac{1}{2}}_{j+\frac{1}{2},k+\frac{1}{2}} =& \frac{1}{4}(U^n_{jk} + U^n_{j,k+1} + U^n_{j+1,k} + U^n_{j+1,k+1}) \\ & - \frac{\Delta t}{2\Delta x}(F^n_{j+1,k+\frac{1}{2}} - F^n_{j,k+\frac{1}{2}}) - \frac{\Delta t}{2\Delta z}(G^n_{j+\frac{1}{2},k+1} - G^n_{j+\frac{1}{2},k}). \end{aligned} \tag{A.2}$$

The *second step* of the scheme is:

$$U^{n+1}_{jk} = U^n_{jk} - \frac{\Delta t}{\Delta x}(\bar{F}^{n+\frac{1}{2}}_{j+\frac{1}{2},k} - \bar{F}^{n+\frac{1}{2}}_{j-\frac{1}{2},k}) - \frac{\Delta t}{\Delta z}(\bar{G}^{n+\frac{1}{2}}_{j,k+\frac{1}{2}} - \bar{G}^{n+\frac{1}{2}}_{j,k-\frac{1}{2}}), \tag{A.3}$$

with

$$\bar{F}^{n+\frac{1}{2}}_{j+\frac{1}{2},k} = (F^{n+\frac{1}{2}}_{j+\frac{1}{2},k+\frac{1}{2}} + F^{n+\frac{1}{2}}_{j+\frac{1}{2},k-\frac{1}{2}})/2; \tag{A.4}$$

$$\bar{G}^{n+\frac{1}{2}}_{j,k+\frac{1}{2}} = (G^{n+\frac{1}{2}}_{j+\frac{1}{2},k+\frac{1}{2}} + G^{n+\frac{1}{2}}_{j-\frac{1}{2},k+\frac{1}{2}})/2. \tag{A.5}$$

This is a nine-point scheme in the sense that only nine points of the mesh at time $n \cdot \Delta t$ are needed to obtain numerical values at time $(n+1) \cdot \Delta t$. *Lapidius* [1967] has proved that the truncation error of the above two-step scheme is $O(\Delta x^3, \Delta z^3)$.

To maintain the numerical stability, *Lapidius* [1967] introduced the following type of stabilizing transformation which consisted of replacing quantities U^{n+1} by new ones,

U'^{n+1}, obtained by smoothing first in the x direction and then in the z direction according to the following prescription.

$$U'^{n+1}_{jk} = U^{n+1}_{jk} + \lambda C \cdot \Delta'[|\Delta' u^{n+1}_{j+1,k}| \cdot \Delta'(U^{n+1}_{j+1,k})] \tag{A.6}$$

$$U''^{n+1}_{jk} = U'^{n+1}_{jk} + \lambda C \cdot \Delta''[|\Delta'' v'^{n+1}_{j,k+1}| \cdot \Delta''(U'^{n+1}_{j,k+1})], \tag{A.7}$$

where $\Delta'_{jk} = U_{jk} - U_{j-1,k}$; $\Delta''_{jk} = U_{jk} - U_{j,k-1}$; and C is a constant while u and v are the x and z components of the fluid velocity, respectively.

Equations (A.6) and (A.7) are fractional steps for the numerical solution of the diffusion equation

$$U_t = \lambda C(\Delta^3)[(|u_x|U_x)_x + (|v_z|U_z)_z]. \tag{A.8}$$

From (A.8) it is clear that smoothing is of third order and consequently does not affect the truncation error of the difference scheme.

References

Akasofu, S.-I., A. T. Y. Lui, C.-I. Meng, and M. Haurwitz, Need for a three-dimensional analysis of magnetic fields in the magnetotail during substorms, *Geophys. Res. Lett.*, *5*, 283, 1978.

Allen, C. W., and D. W. Swift, A particle simulation of the tearing mode instability at the dayside magnetopause, *J. Geophys. Res.*, *94*, 6925, 1989.

Barnes, A., Theoretical constraints on the microscale fluctuations in the interplanetary medium, *J. Geophys. Res.*, *76*, 7522, 1971.

Berchem, J., and C. T. Russell, The thickness of the magnetopause current layer: ISEE 1 and 2 observations, *J. Geophys. Res.*, *87*, 2108, 1982.

Berchem, J., and C. T. Russell, Flux transfer events on the magnetopause: Spatial distribution and controlling factors, *J. Geophys. Res.*, *87*, 8139, 1984.

Biernat, H. K., M. F. Heyn, and V. S. Semenov, Unsteady Petschek reconnection, *J. Geophys. Res.*, *92*, 3392, 1987.

Biernat, H. K., M. F. Heyn, R. P. Rijinbeek, V. S. Semenov and C. J. Farrugia, The structure of reconnection layers: Application to the Earth's magnetopause, *J. Geophys. Res.*, in press, 1988.

Birn, J., and E. W. Hones, Jr., Three-dimensional computer modeling of dynamic reconnection in the geomagnetotail, *J. Geophys. Res.*, *86*, 6802, 1981.

Biskamp, D., Effect of secondary tearing instability on the coalescence of magnetic islands, *Phys. Lett.*, *87A*, 357, 1982.

Biskamp, D., Magnetic reconnection via current sheets, *Phys. Fluids*, *29*, 1520, 1986.

Carmichael, H., A process for solar flares, AAS-NASA Symposium on Solar Flares, edited by W. N. Hess, NASA SP-50, p. 451, 1964.

Coroniti, F. V., and A. Eviatar, Magnetic field reconnection in a collisionless plasma, *Ap. J.*, Suppl. Series, *33*, 189, 1977.

Cowley, S. W. H., Asymmetry effects associated with the x-component of the IMF in a magnetically open magnetosphere, *Planet. Space. Sci.*, *29*, 809, 1981.

Cowley, S. W. H., The causes of convection in the earth's magnetosphere: A review of developments during the IMS, *Rev. Geophys. Res.*, 89, 6689, 1982.

Crooker, N. U., Explorer 33 entry layer observations, *J. Geophys. Res.*, *82*, 515, 1977.

Daly, P. W., D. J. Williams, C. T. Russell, and I. Keppler, Particle signature of magnetic transfer events at the magnetopause, *J. Geophys. Res., 86,* 1628, 1981.

Daly, P. W., M. A. Saunders, R. P. Rijnbeek, N. Sckopke, and C. T. Russell, The distribution of reconnection geometry in flux transfer events using energetic ion plasma and magnetic data, *J. Geophys. Res., 89,* 3843, 1884.

Ding, D. Q., L. C. Lee, and Z. F. Fu, Multiple X line reconnection, 3, A particle simulation of flux transfer events, *J. Geophys. Res.*, *91*, 13,384, 1986.

Dungey, J. W., Interplanetary field and auroral zones, *Phys. Rev. Lett.*, *6*, 47, 1961.

Eastman, T. E., E. W. Hones Jr., S. J. Bame and J. R. Asbridge, The magnetospheric boundary layer: Site of plasma, momentum and energy transfer from the magnetosheath into the magnetosphere, *Geophys. Res. Lett.*, 685, 1976.

Edmiston, J. P., and C. F. Kennel, A parametric study of slow shock Rankine-Hugoniot solutions and critical Mach numbers, *J. Geophys. Res.*, *91*, 1361, 1986.

Elphic, R. C., C. A. Cattell, K. Takahashi, S. J. Bame, and C. T. Russell, ISEE-1 and 2 observation of magnetic flux ropes in the magnetotail: FTE's in the plasma sheet?, *Geophys. Res. Lett.*, *13*, 648, 1986.

Fairfield, D. H., On the average configuration of the geomagnetic tail, *J. Geophys. Res.*, *84*, 1950, 1979.

Feldman, W. C., S. J. Schwartz, S. J. Bame, D. N. Baker, J. Birn, J. T. Gosling, E. W. Hones, Jr., D. J. McComas, J. A. Slavin, E. J. Smith and R. D. Zwickl, Evidence for slow mode shocks in the distant geomagnetic tail, *Geophys. Res. Lett.*, *11*, 599, 1984.

Feldman, W. C., R. L. Tokar, J. Birn, E. W. Hones, Jr., S. J. Bame and C. T. Russell, Structure of a slow mode shock observed in the plasma sheet boundary layer, *J. Geophys. Res.*, *92*, 83, 1987.

Forbes, T. G., and E. R. Priest, On reconnection and plasmoids in the geomagnetic tail, *J. Geophys. Res.*, *88*, 863, 1983.

Forbes, T. G., and E. R. Priest, A comparison of analytical and numerical models for steadily driven magnetic reconnection, *Rev. Geophys.*, *25*, 1583, 1987.

Frank, L. A., Plasma in the Earth's polar magnetosphere, *J. Geophys. Res.*, *76*, 5202, 1971.

Fu, Z. F., and L. C. Lee, Simulation of multiple X line reconnection at the dayside magnetopause, *Geophys. Res. Lett.*, *12*, 291, 1985.

Fu, Z. F., and L. C. Lee, Multiple X line reconnection, 2, The dynamics, *J. Geophys. Res.*, *91*, 13,373, 1986.

Furth, H. P., J. Killeen, and M. N. Rosenbluth, Finite resistivity instabilities of a sheet pinch, *Phys. Fluids*, *6*, 459, 1963.

Giovanelli, R. G., A theory of chromospheric flares, *Nature*, *158*, 81, 1946.

Giovanelli, R. G., Chromospheric Flares, *Mon. Not. Roy. Ast. Soc.*, *108*, 163, 1948.

Glassmeier, K. H., M. Lester, W. A. C. Mier-Jedrzejowicz, C. A. Green, G. Rostoker, D. Orr, J. Wedeken, H. Junginger, and E. Amata, Pc 5 pulsations and their possible source mechanisms: A case study, *J. Geophys. Res.*, *55*, 108, 1984.

Gosling, J. T., J. R. Asbridge, S. J. Bame, W. C. Feldman, G. Paschmann, N. Sckopke and C. T. Russell, Evidence for quasi-stationary reconnection at the dayside magnetopause, *J. Geophys. Res.*, *87*, 2147, 1982.

Haerendel, G., Microscopic plasma processes related to reconnection, *J. Atmos. Terr. Phys.*, *40*, 343, 1977.

Haerendel, G., G. Paschmann, N. Sckopke, H. Rosenbauer, and P. C. Hedgecock, The frontside boudary layer of the magnetosphere and the problem of reconnection, *J. Geophys. Res.*, *83*, 3195-3216, 1978.

Hau, L.-N., and B. U. Ö. Sonnerup, On the structure of resistive MHD intermediate shocks, *J. Geophys. Res.*, *94*, 6539, 1989.

Hayashi, T., and T. Sato, Magnetic reconnection: Acceleration, heating, and shock formation, *J. Geophys. Res.*, *83*, 217, 1978.

Heikkila, W. J., and J. D. Winningham, Penetration of the magnetosheath plasma to low latitudes through the dayside magnetospheric cusps, *J. Geophys. Res.*, *76*, 3657, 1971.

Heikkila, W. J., Is there an electrostatic field tangential to the dayside magnetopause and neutral line?, *Geophys. Res. Lett.*, *2*, 154-157, 1975.

Heyn, M. F., H. K. Biernat, R. P. Rijnbeek and V. S. Semenov, The structure of reconnection layer, *J. Plasma Phys.*, in press, 1988.

Hones, E. W., Jr., J. Birn, S. J. Bame, G. Paschmann, and C. T. Russell, On the three-dimensional magnetic structure of the plasmoid created in the magnetotail at substorm onset, *Geophys. Res. Lett.*, *9*, 203, 1982.

Hoshino, M., and A. Nishida, Numerical simulation of the dayside reconnection, *J. Geophys. Res.*, *88*, 6926, 1983.

Hoyle, F., Magnetic storms and aurorae, in *Some Recent Researches in Solar Physics*, p. 102-104, Cambridge University Press, 1949.

Huba, J. D., N. T. Gladd, and K. Papadopoulos, Lower-hybrid-drift wave turbulence in the distant magnetotail, *J. Geophys. Res.*, *83*, 5217, 1978.

Hughes, W. J., and D. G. Sibeck, On the 3-dimensional structure of plasmoids, *Geophys. Res. Lett.*, *14*, 636, 1987.

Jeffrey, A. and T. Taniuti, *Non-linear wave propagation*, Academic Press, London, 1964.

Kan, J., A theory of patchy and intermittent reconnections for magnetospheric flux transfer events, *J. Geophys. Res.*, *93*, 5613, 1988.

Kantrowitz, A. and H. E. Petschek, MHD characteristics and shock waves, in *Plasma Physics in Theory and Application*, edited by W. B. Kunkel, p. 148, McGraw-Hill, New York, 1966.

King, J. H., *Interplanetary medium data book–Appendix, NSSDC/WDC-A-R&S 77-04a*, September, 1977

Kulikovskiy, A. G., and G. A. Lyubimov, *Magnetohydrodynamics*, Addison-Wesley Publishing Company, Inc., 198 pp., 1965.

La Belle-Hamer, A. L., Z. F. Fu, and L. C. Lee, A mechanism for patchy reconnection at the dayside magnetopause, *Geophys. Res. Lett.*, *15*, 152, 1988.

Lanzerotti, L. J., L. C. Lee, C. G. Maclennan. A. Wolfe, and L. V. Medford, Possible evidence of flux transfer events in the polar ionosphere, *Geophys. Res. Lett.*, *13*, 1089, 1986.

Lapidius, A., A detached shock calculation by second-order finite differences, *J. Comp. Phys.*, *2*, 154, 1967.

Leboeuf, J. N., T. Tajima, C. F. Kennel and J. M. Dawson, Global simulation of the time-dependent magnetosphere, *Geophys. Res. Lett.*, *5*, 609, 1978.

Leboeuf, J. N., T. Tajima, and J. M. Dawson, Dynamic magnetic X points, *Phys. Fluids*, *25*, 784, 1982.

Lee, L. C., Ion two-stream and modified two-stream instabilities in the magnetic neutral sheet, *Geophys. Res. Lett.*, *9*, 1159, 1982.

Lee, L. C., Magnetic flux transfer at the earth's magnetopause, in *Solar Wind-Magnetopause Coupling*, edited by Y. Kamide and J. Slavin, Terra Scientific Company, Tokyo, p. 297, 1986.

Lee, L. C., and J. Kan, A unified kinetic model of the tangential magnetopause structure, *J. Geophys. Res.*, *84*, 6417, 1979.

Lee, L. C., and Z. F. Fu, A theory of magnetic flux transfer at the earth's dayside magnetopause, *Geophys. Res. Lett.*, *12*, 105, 1985.

Lee, L. C., and Z. F. Fu, Multiple X line reconnection 1. A criterion for the transition from a single X line to a multiple X line reconnection, *J. Geophys. Res.*, *91*, 6807, 1986*a*.

Lee, L. C., and Z. F. Fu, Collisional tearing instability in the current sheet with a low magnetic Lundquist number, *J. Geophys. Res.*, *91*, 3311, 1986*b*.

Lee, L. C., Y. Shi, and L. J. Lanzerotti, A mechanism for the generation of cusp region hydromagnetic waves, *J. Geophys. Res.*, *93*, 7578, 1988.

Lees, L., Interaction between the solar plasma wind and the geomagnetic cavity, *AIAA J.*, *2*, 1576, 1967.

Levy, R. H., H. E. Petschek, and G. L. Siscoe, Aerodynamic aspects of the magnetospheric flow, *AIAA J.*, *2*, 2065, 1964.

Lui, A. T. Y., Characteristics of the cross-tail current in the earth's magnetotail, in *Magnetospheric Currents*, edited by T. A. Potemra, p. 158, AGU, Washington DC, 1984.

Lyon, J. G., S. H. Brecht, J. D. Huba, J. A. Fedder, and P. J. Palmadesso, Computer simulation of a geomagnetic substorm, *Phys. Rev. Lett.*, *46*, 1038, 1981.

Maezawa, K., Dependence of the magnetopause position on the southward interplanetary magnetic field, *Planet. Space Sci.*, *22*, 1443, 1974.

Matthaeus, W. H., and S. L. Lamkin, Rapid magnetic reconnection caused by finite amplitude fluctuations, *Phys. Fluids*, *28*, 303, 1985.

Ness, N. F., The earth's magnetic tail, *J. Geophys. Res.*, *70*, 2989, 1965.

Nishida, A., M. Scholer, T Terasawa, S. J. Bame, G. Gloeckler, E. J. Smith, and R. D. Zwickl, Quasi-stagnant plasmoid in the middle tail: a new preexpansion phase phenomenon, *J. Geophys. Res.*, *91*, 4245, 1986.

Ogino, T., R. J. Walker, M. Ashour-Abdalla, and J. M. Dawson, An MHD simulation of the effects of the interplanetary magnetic field B_y component on the interaction of the solar wind with the earth's magnetosphere during southward interplanetary magnetic field, *J. Geophys. Res.*, *91*, 10029, 1986.

Ogino, T., R. J. Walker, and M Ashour-Abadalla, A magnetohydrodynamic simulation of the formation of magnetic flux tubes at the earth's dayside magnetopause, *Geophys. Res. Lett.*, *16*, 155, 1989.

Olson, J. V., ULF signatures of the polar cusp, *J. Geophys. Res.*, *91*, 10,055, 1986.

Papamastorakis, I., G. Paschmann, W. Baumjohann, B. U. Ö. Sonnerup, and H. Lühr, Orientation, motion, and other properties of flux transfer event structures on September 4, 1984, *J. Geophys. Res.*, *94*, 8852, 1989.

Parker, E. N., Sweet's mechanism for merging magnetic fields in conducting fluids, *J. Geophys. Res.*, *62*, 509, 1957.

Parker, E. N., The solar flare phenomenon and the theory of reconnection and annihilation of magnetic fields, *Astrophys. J. Suppl., Series 8*, 177, 1963.

Paschmann, G., B. U. Ö. Sonnerup, I. Papamastorakis, N. Sckopke, G. Haerendel, S. J. Bame, J. R. Asbridge, J. T. Gosling, C. T. Russell and R. C. Elphic, Plasma acceleration at the Earth's magnetopause: Evidence for reconnection, *Nature*, *282*, 243, 1979.

Paschmann, G., G. Haerendel, I. Papamastorakis, N. Sckopke, S. J. Bame, J. T. Gosling, and C. T. Russell, Plasma and magnetic field characteristics of magnetic flux transfer events, *J. Geophys. Res.*, *87*, 2159, 1982.

Paschmann, G., I. Papamastorakis, W. Baumjohan, N. Sckopke, C. W. Carlson, B. U. Ö. Sonnerup and H. Lühr, The magnetopause for large magnetic shear: AMPTE/IRM observations, *J. Geophys. Res.*, *91*, 11099, 1986.

Petschek, H. E., Magnetic field annihilation, in AAS-NASA Symposium on the Physics of Solar Flares, *NASA Spec. Publ., SP-50*, 425-439, 1964.

Podgorny, I. M., E. M. Dubinin, U. N. Potanin, The magnetic field on the magnetospheric boundary from laboratory simulation data, *Geophys. Res. Lett.*, *4*, 207, 1978.

Priest, E. R., and M. A. Raduu, Preflare current sheets in the solar atmosphere, *Solar Phys.*, *43*, 177, 1975.

Priest, E. R., and T. G. Forbes, New models for fast steady state magnetic reconnection, *J. Geophys. Res.*, *91*, 5579, 1986.

Richardson, I. G., and S. W. H. Cowley, Plasmoid-associated energetic ion bursts in the deep geomagnetic tail: properties of the boundary layer, *J. Geophys. Res.*, *90*, 12,133, 1985.

Rijnbeek, R. P., S. W. H. Cowley, D. J. Southwood, and C. T. Russell, A survey of dayside flux transfer events observed by ISEE 1 and 2 magnetometers, *J. Geophys. Res.*, *89*, 786, 1984.

Rijnbeek, R. P., H. K. Biernat, M. F. Heyn, V. S. Semenov, C. J. Farrugia, D. J. Southwood, G. Paschmann, N. Sckopke, and C. T. Russell, The structure of the reconnection layer observed by ISEE 1 on 8 September 1978, *Annales Geophys.*, submitted, 1988.

Russell, C. T., and R. C. Elphic, Initial ISEE magnetometer results: magnetopause observations, *Space Sci. Rev.*, *22*, 681, 1978.

Russell, C. T., and R. C. Elphic, ISEE observations of flux transfer events at the dayside magnetopause, *Geophs. Res. Lett.*, *6*, 33, 1979.

Russell, C. T., J. Berchem, and J. Luhmann, On the source region of flux transfer events, *Adv. Space Res.*, *5*, 363, 1985.

Sakai, J. I., Forced reconnexion by fast magnetosonic waves in a current sheet with stagnation-point flows, *J. Plasma Phys.*, *30*, 109, 1983.

Samson, J. C., J. A. Jacobs, and G. Rostoker, Latitude-dependent characteristics of long-period geomagnetic micropulsations, *J. Geophys. Res.*, *76*, 3675, 1971.

Sato, T., Strong plasma acceleration by slow shocks resulting from magnetic reconnection, *J. Geophys. Res.*, *84*, 7177, 1979.

Sato, T., and T. Hayashi, Externally driven magnetic reconnection and a powerful magnetic energy converter, *Phys. Fluids*, *22(6)*, 1189, 1979.

Sato, T., T. Shimada, M. Tanaka, T. Hayashi, and K. Watanabe, Formation of field twisting flux tubes on the magnetopause and solar wind particle entry into the magnetosphere, *Geophys. Res. Lett.*, *13*, 801, 1986.

Saunders, M. A., C. T. Russell, and N. Sckopke, Flux transfer events: Scale size and interior structure, *Geophys. Res. Lett.*, *11*, 131, 1984.

Scholer, M., Magnetic flux transfer at the magnetopause based on single X line bursty reconnection, *Geophys. Res. Lett.*, *15*, 291, 1988*a*.

Scholer, M., Strong core fields in magnetopause flux transfer events, *Geophys. Res. Lett.*, *8*, 748, 1988*b*.

Scholer, M. Undriven magnetic reconnection in an isolated current sheet, *J. Geophys. Res.*, *94*, 8805, 1989.

Scholer, M., and D. Roth, A simulation study on reconnection and small scale plasmoid formation, *J. Geophys. Res.*, *92*, 3223, 1987.

Scholer, M, D. Hovestadt, F. M. Ipavich, and G. Gloeckler, Energetic protons, alpha particles, and electrons in magnetic flux transfer events, *J. Geophys. Res.*, *87*, 2169, 1982.

Scholer, M., D. N. Baker, S. J. Bame, W. Baumjohann, G. Gloeckler, F. M. Ipavich, E. J. Smith, and B. T. Tsurutani, Correlated observations of substorm effects in the near-earth region and deep magnetotail, *J. Geophys. Res.*, *90*, 4021, 1985.

Shi, Y., C. C. Wu, and L. C. Lee, A study of multiple X line reconnection at the dayside magnetopause, *Geophys. Res. Lett.*, *15*, 295, 1989.

Sibeck, D. G., G. L. Siscoe, J. A. Slavin, E. J. Smith, S. J. Bame, and F. L. Scarf, Magnetotail flux ropes, *Geophys. Res. Lett.*, *11*, 1090, 1984.

Sibeck, D. G., G. L. Siscoe, J. A. Slavin, E. J. Smith, B. T. Tsurutani, and S. J. Bame, Magnetic field properties of the distant magnetotail magnetopause and boundary layer, *J. Geophys. Res.*, *90*, 9561, 1985.

Sonnerup, B. U. Ö, Magnetic-field re-connexion in a highly conducting incompressible fluid, *J. Plasma Phys.*, *4*, 161, 1970.

Sonnerup, B. U. Ö, Magnetopause and boundary layer, in *Physics of Solar Planetary Environments*, ed. by D. J. Williams, p. 541, *AGU*, Washington, D.C., 1976.

Sonnerup, B. U. Ö, Magnetic field reconnection, in *Solar System Plasma Physics, Vol III*, p45, ed. by C. F. Kennel, L. T. Lanzerotti, and E. N. Parker, North Holland Publishing Company, 1979.

Sonnerup, B. U. Ö, Magnetic field reconnection at the magnetopause: an overview, in *Magnetic reconnection in Space and Laboratory Plasmas*, p. 93, edited by E. W. Hones, Jr., American Geophysical Union, Washington D. C., 1984.

Sonnerup, B. U. Ö, On the stress balance in flux transfer events, *J. Geophys. Res.*, *92*, 8613, 1987.

Sonnerup, B. U. Ö, and L. J. Cahill, Jr., Magnetopause structure and altitude from Explorer 12 observations, *J. Geophys. Res.*, *72*, 171, 1967.

Sonnerup, B. U. Ö, and J. Sakai, Stability of a current sheet with resistive MHD stagnation-point flows (abstract), *Eos Trans. AGU*, *65*, 353, 1981.

Sonnerup, B. U. Ö, G. Paschmann, I. Papamastorakis, N. Sckopke, G. Haerendel, S. J. Bame, J. R. Asbridge, J. T. Gosling, and C. T. Russell, Evidence for magnetic field reconnection at the earth's magnetopause, *J. Geophys. Res.*, *86*, 10,049, 1981.

Southwood, D. J., M. A. Saunders, M. W. Dunlop, W. A. C. Mier-Jedrzejowicz and R. P. Rijnbeek, A survey of flux transfer events recorded on the UKS spacecraft magnetometer, *Planet. Space Sci.*, *34*, 1349, 1986.

Southwood, D. J., The ionospheric signature of flux transfer events, J. Geophys. Res., 92, 3207, 1987.

Southwood, D. J., C. J. Farrugia, and M. A. Saunders, What are flux transfer events? *Planet. Space Sci.*, *36*, 503, 1988.

Speiser, T. W., Conductivity without collision or noise, *Planet. Space Sci.*, *18*, 613, 1970.

Spreiter, J. R., and A. Y. Alksne, Plasma flow around the magnetosphere, *Rev. Geophys. Space Phys.*, 7, 11, 1969.

Stern, D. P., A study of the electric field in an open magnetospheric model, *J. Geophys. Res.*, *78*, 7292, 1973.

Sweet, P. A., The neutral point theory of solar flares, in *Electromagnetic Phenomena in Cosmical Physics*, edited by B. Lehnert, Cambridge University Press, p. 123, 1958.

Swift, D. W., Substorms and magnetospheric energy transfer processes, in *Dynamics of the Magnetosphere*, edited by S.-I. Akasofu, p.327, D. Reidel Publishing Co., Dordrecht, 1980.

Troitskaya, V. A., Results of ULF-wave investigations in the USSR, in *Achievements of the International Magnetospheric Study (IMS), Proceedings of an International Symposium, Graz, Austria,* ESA Publications, Noordwijk, Netherlands, 1984.

Tsurutani, B. T., D. E. Jones, R. P. Lepping, E. J. Smith, and D. G. Sibeck, The relationship between the IMF B_y and the distant tail (150-238 R_E) lobe and plasmasheet B_y fields, *Geophys. Res. Lett.*, *11*, 1082, 1984.

Ugai, M., Dependence of fast magnetic reconnection on electrical resistivity in an isolated current-sheet system, *Phys. Fluids*, *26*, 1569, 1983.

Ugai, M., Self-consistent development of fast magnetic reconnection with anomalous plasma resistivity, *Plasma Phys. Contr. Fusion*, *26*, 1549, 1984.

Ugai, M., and T. Tsuda, Magnetic field line reconnexion by localized enhancement of resistivity. Part 1. Evolution in a compressible MHD fluid, *J. Plasma Phys.*, *17*, 337, 1977.

Vasyliunas, V. M., Theoretical models of magnetic field line merging, 1., *Rev. Geophys.*, *13*, 303, 1975.

Walén, C., On the theory of sunspots, *Ark. Mat. Astron. Fys.*, *30A(15)*, 1–87, 1944.

Wu, C. C, R. J. Walker, and J. D. Dawson, A three dimensional MHD model of the earth's magnetosphere, *Geophys. Res. Lett.*, *8*, 523, 1981.

Wu, C. C., On MHD intermediate shocks, *Geophys. Res. Lett.*, *14*, 668, 1987.

Wu, C. C., The MHD intermediate shock interaction with an intermediate wave: are intermediate shocks physical? *J. Geophys. Res.*, *93*, 987, 1988*a*.

Wu, C. C., Effects of dissipation on rotational discontinuities, *J. Geophys. Res.*, *93*, 2369, 1988*b*.

Yang, C.-K., and B. U. Ö. Sonnerup, Compressible magnetopause reconnection, *J. Geophys. Res.*, *82*, 699, 1977.

Yeh, T., and W. I. Axford, On the re-connexion of magnetic field lines in conducting fluids, *J. Plasma Phys.*, *4*, 207, 1970.

Zwan, B. J., and R. A. Wolf, Depletion of solar wind plasma near a planetary boundary, *J. Geophys. Res.*, *81*, 1636, 1976.